# Chem Soc Rev



## **REVIEW ARTICLE**

View Article Online



Cite this: Chem. Soc. Rev., 2021, **50**. 5086

> Zhenduo Cui, a Yanqin Liang, 🕩 a Zhaoyang Li, 🕩 a Shengli Zhu, 🕩 a Xianbao Wang (D) and Shuilin Wu (D)\*a

Qiyao Zheng,<sup>a</sup> Xiangmei Liu,\*b Yufeng Zheng, och Kelvin W. K. Yeung,<sup>d</sup>

The recent progress on metal-organic

frameworks for phototherapy

Some infectious or malignant diseases such as cancers are seriously threatening the health of human beings all over the world. The commonly used antibiotic therapy cannot effectively treat these diseases within a short time, and also bring about adverse effects such as drug resistance and immune system damage during long-term systemic treatment. Phototherapy is an emerging antibiotic-free strategy to treat these diseases. Upon light irradiation, phototherapeutic agents can generate cytotoxic reactive oxygen species (ROS) or induce a temperature increase, which leads to the death of targeted cells. These two kinds of killing strategies are referred to as photodynamic therapy (PDT) and photothermal therapy (PTT), respectively. So far, many photo-responsive agents have been developed. Among them, the metalorganic framework (MOF) is becoming one of the most promising photo-responsive materials because its structure and chemical compositions can be easily modulated to achieve specific functions. MOFs can have intrinsic photodynamic or photothermal ability under the rational design of MOF construction, or serve as the carrier of therapeutic agents, owing to its tunable porosity. MOFs also provide feasibility for various combined therapies and targeting methods, which improves the efficiency of phototherapy. In this review, we firstly investigated the principles of phototherapy, and comprehensively summarized recent advances of MOF in PDT, PTT and synergistic therapy, from construction to modification. We expect that our demonstration will shed light on the future development of this field, and bring it one step closer to clinical trials.

Received 24th January 2021 DOI: 10.1039/d1cs00056j

rsc.li/chem-soc-rev

### 1. Introduction

The history of light treatment dates back to 3000 years ago, when the ancient civilizations utilized light to treat skin cancer, rickets and vitiligo.1 In 1903, Niels Finsen was awarded the Nobel Prize for using red light and ultraviolet (UV) light to treat smallpox pustules and cutaneous tuberculosis, which was known as the beginning of "phototherapy". 1,2 In 1975, Thomas Dougherty firstly demonstrated complete tumor eradication of mice, which aroused extensive investigation in this field.<sup>1,3</sup> Nowadays, phototherapy refers to cell-killing treatment by certain

therapeutic agents under appropriate light irradiation. There are two distinct killing strategies: reactive oxygen species (ROS) generation and temperature increase, and the former route is named photodynamic therapy (PDT) while the latter is called photothermal therapy (PTT). Compared to traditional treatment strategies such as chemotherapy and radiotherapy, phototherapy is less invasive, highly selective and causes minimum damage to normal tissues. 4,5 In recent decades, more and more researchers have been trying to apply phototherapy in the treatment of cancer and nonmalignant diseases, and have achieved good therapeutic efficacy. 4,6 Therefore, phototherapy is showing great promise as an emerging type of therapeutic method.

In the case of PDT, a photosensitizer (PS) is irradiated by a certain wavelength of light, leading to the generation of highly toxic ROS, including the superoxide anion radical ( ${}^{\bullet}O_2^-$ ), hydroxyl radical (\*OH), hydrogen peroxide (H2O2) and singlet oxygen ( ${}^{1}O_{2}$ ). These ROS, especially  ${}^{1}O_{2}$  and  ${}^{\bullet}OH$ , are cytotoxic oxidizing agents that can diffuse through the membrane and then directly react with many biomolecules in cells such as proteins and DNA, thus inducing cell death and tissue lesions.<sup>4,7</sup> The superoxide anion radical is more like an intermediate for the generation of H<sub>2</sub>O<sub>2</sub> and OH via Type I process in PDT, or by reacting with metal ions (e.g. Fe<sup>2+</sup>), namely the Fenton reaction.<sup>7</sup>

<sup>&</sup>lt;sup>a</sup> School of Materials Science & Engineering, The Key Laboratory of Advanced Ceramics and Machining Technology by the Ministry of Education of China, Tianjin University, Tianjin 300072, China. E-mail: shuilinwu@tju.edu.cn

<sup>&</sup>lt;sup>b</sup> Ministry-of-Education Key Laboratory for the Green Preparation and Application of Functional Materials. Hubei Key Laboratory of Polymer Materials. School of Materials Science & Engineering, Hubei University, Wuhan 430062, China. E-mail: liuxiangmei1978@163.com

<sup>&</sup>lt;sup>c</sup> State Key Laboratory for Turbulence and Complex System and Department of Materials Science and Engineering, College of Engineering, Peking University, Beijing 100871, China

<sup>&</sup>lt;sup>d</sup> Department of Orthopaedics & Traumatology, Li Ka Shing Faculty of Medicine, The University of Hong Kong, Pokfulam, Hong Kong, China

**Review Article** Chem Soc Rev

However, as the lifetime of ROS is short, the direct influence of ROS has a limited radius of action. For example, the lifetime of <sup>1</sup>O<sub>2</sub> is around 48 ns and its diffusion in cells is approximately 20 nm.8 Therefore, targeted cells should be in proximity, to where ROS is generated. Besides direct cytotoxic effects, PDT also causes vascular injury and robust immune response, which depends on the interval between drug administration and light irradiation.<sup>6,9</sup> A longer interval provides the PS with sufficient time to diffuse through tissues, while a shorter interval renders the accumulation of PS in vessels, thus inducing vascular stasis and thrombus formation. Porphyrin and its derivatives are the most commonly used PS in clinical settings, owing to their low dark toxicity and high ROS quantum yield. 10 Hematoporphyrin derivative (HPD) is the first approved PS for clinical usage by the US Food and Drug Administration (FDA), followed by Foscan®, Levulan®, and Radachlorin®, etc. because of their excellent photochemical properties.<sup>2,5</sup> Besides that, organic dyes,<sup>11</sup> quantum dots,<sup>12</sup> black phosphorus, <sup>13</sup> red phosphorus, <sup>14</sup> copper sulfide, <sup>15</sup> zinc oxide, <sup>16</sup> graphic carbon nitride  $(g-C_3N_4)^{17}$  can also act as PSs. To date, PSs have been developed from bare HPD and its derivatives to those carrier-loaded PSs with long-wavelength absorption and selective accumulation. However, these properties still need further improvement.10 Other drawbacks of the existing PSs are hydrophobicity-induced aggregation, limited diffusion of ROS, oxygen dependence and undesirable penetration depth, etc.

Different from PDT, the mechanism of PTT is like causing a localized "fever" in the therapeutic sites. During this course, the temperature increase is triggered by light irradiation on photothermal agents (PTAs) through the nonradiative relaxation of excited electrons. The efficacy of PTA was evaluated by photothermal conversion efficiency, which refers to the ratio between the absorption ( $\sigma_{abs}$ ) and extinction ( $\sigma_{ext}$ ) of light, according to the following equation:18

$$\mu = \sigma_{\rm abs}/\sigma_{\rm ext} \tag{1}$$

Based on the final temperature, PTT can be categorized into diathermia (<41 °C), hyperthermia (41-46 °C) and thermal ablation (>46 °C). 19-23 Diathermia is a relatively mild treatment that can promote tumor oxygenation by increasing blood flow, thereby sensitizing cells to radiotherapy and chemotherapy.<sup>22</sup> Diathermia is also applied in physiotherapy for rheumatic treatment and muscle relaxation. 19,20 In hyperthermia, heat stress causes protein denaturation and aggregation, cell membrane loosening and DNA cross-linking, which strongly affect cellular functions and finally lead to cell inactivation. 20,21,24 However, in this temperature range, the expression of heat shock protein is higher, which is a molecular chaperone that repairs thermal damage to cells, leading to the formation of thermoresistance. 25,26 Moreover, hyperthermia is also able to induce the sensitization of cells towards heat, 22 antibiotics, 27 and other therapies.<sup>23</sup> Thermal ablation can directly cause coagulative necrosis of cells in a few minutes, which is irreversible damage. 19 Despite the high efficiency of thermal ablation, it can also affect healthy cells, induce inflammation and cancer metastasis.<sup>28</sup> When the temperature is above 60 °C, rapid necrosis of cells will occur due to enzyme inactivation and protein denaturation.<sup>29</sup> Hence, the therapeutic temperature should be appropriately designed to achieve desirable efficacy. PTAs have several distinct types: carbon material, 30-32 noble metal material, <sup>33–35</sup> organic dyes, <sup>36,37</sup> conjugated polymers, <sup>38,39</sup> manganese dioxide, 40 magnetic nanoparticles, 20 etc. Similar to PSs, limited penetration depth and lack of selectivity are the main drawbacks of PTAs. To utilize sensitization, prevent thermoresistance and reduce damage to healthy tissues, PTT requires a more elaborate design and a new therapeutic platform for combined therapy.

Metal-organic frameworks (MOFs) are emerging materials that are widely utilized in gas storage, gas separation, catalysis and medical treatment. 41 The main components of the MOF are metal nodes (or metal clusters) and organic linkers (mostly carboxyl- or nitrogen-containing agents), which are joined by coordination bonds, forming one-, two- or three-dimensional networks. 41-43 Numerous combinations of metals and linkers give rise to diverse MOFs with different structures and properties. Moreover, MOF is highly porous, with pore size ranging from the micro- to the meso-scale, providing space for guest molecules.<sup>44</sup> The well-defined structure of the MOF has a clear relationship with their properties, which offers guidance for future modifications. 41 In terms of biomedical applications, MOFs have shown great promise in chemotherapy, phototherapy, diagnosis and imaging. Due to the tunable pore size, MOFs have been reported as efficient drug carriers. The weak coordination bonds in MOFs render the stimuli-responsive release of drugs.45 MOFs have a large number of reactive sites, 46 which are suitable for further modifications such as targeting molecule attachment, thus greatly improving the selectivity of therapeutic nanoparticles (NPs). Under rational design, some MOFs are nontoxic and biodegradable and can be eliminated from the body with low side effects.

The study of MOFs in phototherapy started in the last decade (2010-2020) and showed a rapidly growing tendency in recent years (Fig. 1). The major functions of MOFs in phototherapy are schematically summarized in Fig. 2. MOFs can directly act as PSs

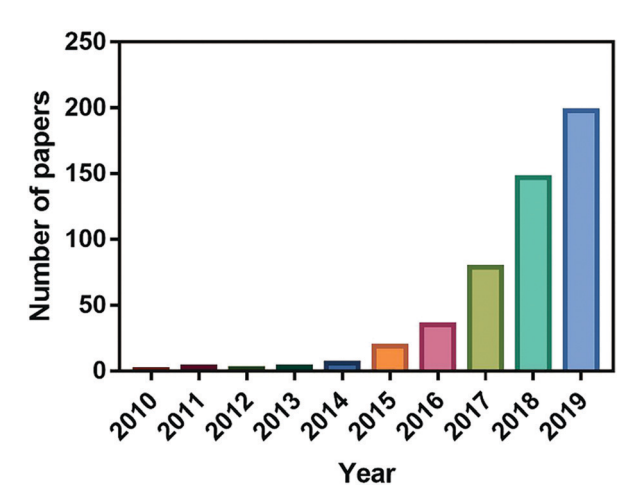


Fig. 1 The number of publications in the last decade that focused on the topic of phototherapy by using a metal-organic framework based on a Web of Science search conducted on March 31st 2020.

Chem Soc Rev

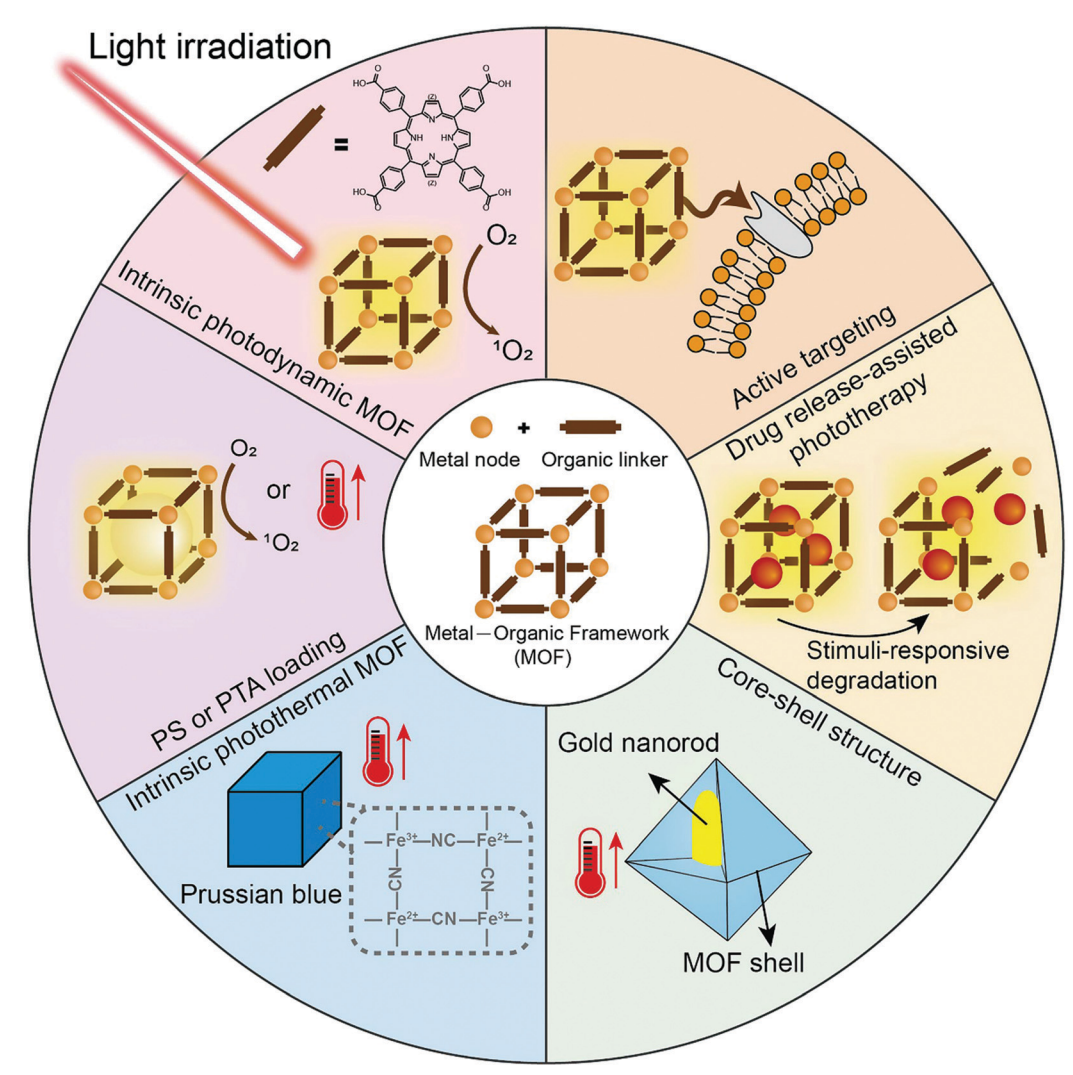


Fig. 2 Summary of the major functions of MOFs in phototherapy.

or PTAs by using photo-responsive building units, 47-49 thus constructing intrinsic photodynamic or photothermal MOFs. They can also realize photo-responsive ability by loading phototherapeutic agents, 50,51 or forming core-shell structures and other composites. 52,53 The structural design and modification of MOFs can tune the light absorption<sup>54,55</sup> and electron transition pathway<sup>56</sup> for improving the efficiency of ROS generation or temperature increase, and also help therapeutic particles to better adapt to the physiological environment through hypoxia alleviation<sup>57</sup> or targeting molecule attachment.<sup>58</sup> MOFs are also excellent platforms for combined therapy such as chemotherapy, 59-61 starvation therapy<sup>62,63</sup> and gas therapy, <sup>64,65</sup> which greatly improve the therapeutic efficacy as compared to phototherapy alone. Due to the stimuli-responsive degradation of MOF, the loaded agents can be released and function in certain environments, preventing the loss during transportation. 51,66

In this review, we firstly illustrate the principles of phototherapy, then comprehensively summarize the recent advances of MOFs in phototherapy (including PDT, PTT and PDT-PTT synergistic therapy) from the intrinsic photo-responsive MOFs to the modified MOFs, and then categorize the typical methods for therapy optimization. We mainly focus on how MOFs function and make a difference in each therapeutic system. Finally, we address the existing drawbacks and challenges in this rapidly growing research field.

## 2. Principles of phototherapy

Phototherapy is initiated by light irradiation on therapeutic agents. During this process, some incident photons impinge on chromophores and then undergo scattering, transmission, or absorption.3 As only absorbed photons can take effect in phototherapy, we use the Jablonski diagram to describe this process, as shown in Fig. 3a. 19,67-70 Absorption occurs when an electron in the ground state (S<sub>0</sub>) interacts with a photon with energy equal to the difference between two electronic states. The energy of the photon is then transferred to the electron, bringing the electron from the ground state to the short-lived  $(\sim 10^{-6} \text{ s})$  higher-energy singlet excited state (S<sub>1</sub>), and then the

**Review Article** Chem Soc Rev

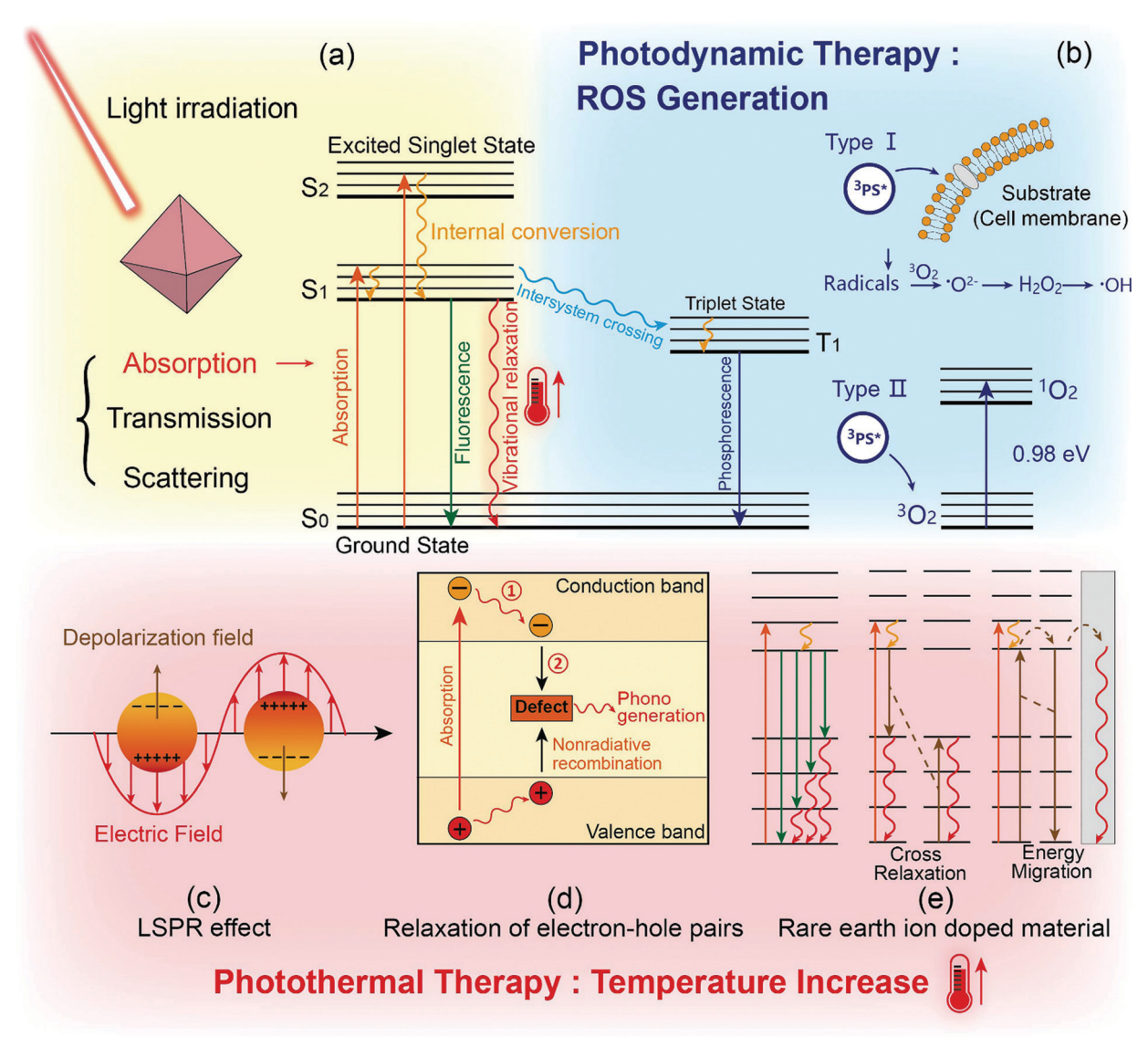


Fig. 3 Photophysics and photochemistry processes of phototherapy: (a) Jablonski diagram; (b) Type I and Type II mechanism of PDT; schematic illustration of (c) the LSPR effect, (d) relaxation of electron-hole pairs, and (e) rare earth ion doped material in PTT.

electron relaxes to the lowest vibrational level of the excited state through internal conversion.<sup>5,67</sup> Internal conversion is a nonradiative process that occurs between energy states of the same spin multiplicity, which is a rapid process.<sup>71</sup> Finally, the excited electron goes back to the ground state by three pathways: fluorescence, phosphorescence, and vibrational relaxation.<sup>2,67</sup>

Fluorescence refers to a radiative electron transition from the lowest vibrational excited state to the ground state, which has the same spin multiplicity, inducing the release of a photon.<sup>3,71</sup> In medical fields, fluorescence is mostly applied to imaging guidance including diagnostics, drug delivery, monitoring, and surgery imaging. 9,72 For example, fluorescence imaging can be used for defining the margin between a tumor and healthy tissues, or serve as the marker of the body's response to treatment. 9,73 After drug administration, fluorescence can monitor the location of drugs and determine the degree of drug uptake by

diseased tissues.<sup>73</sup> Hence, guidance by fluorescence imaging can provide important information about the disease and treatment. It is also helpful in understanding the mechanism and adjusting the parameters of therapy.<sup>73</sup>

Different from fluorescence, phosphorescence emission occurs by electron transitions between energy states of different spin multiplicity. The electron firstly enters the long-lived  $(\sim 10^{-2} \text{ s})$  triplet state  $(T_1)$  through a process called intersystem crossing, leading to the change in the electron spin orientation.<sup>3,5</sup> Intersystem crossing is a forbidden transition caused by the interaction between the orbital angular momentum of the electron and the magnetic dipole related to the electron spin.<sup>3,74</sup> Afterwards, the electron usually transfers energy by phosphorescence emission and then relaxes to the ground state. However, as the lifetime of T<sub>1</sub> is long, many kinds of quenchers can react with the T<sub>1</sub> electron before phosphorescence emission.<sup>73</sup>

In high partial oxygen solvents, the electron in T<sub>1</sub> can transfer energy by reacting with a nearby substrate or triplet state molecules such as molecular oxygen (<sup>3</sup>O<sub>2</sub>), thus producing ROS.<sup>1,3</sup>

To be specific, ROS are generated through two distinct routes, namely, the Type I and Type II mechanism (Fig. 3b). In the Type I mechanism, PS in the triplet state (referred to as <sup>3</sup>PS\*) transfers a proton or an electron to the nearby substrate (e.g., cell membrane, protein and lipid, etc.) or other PS molecules, which leads to the formation of a radical anion or radical cation (eqn (2) and (3)).1,10,75,76

$${}^{3}PS^{*} + {}^{3}PS^{*} \rightarrow {}^{\bullet}PS^{+} + {}^{\bullet}PS^{-}$$
 (2)

$$^{3}PS^{*} + Substrate \rightarrow ^{\bullet}Substrate^{+} + ^{\bullet}PS^{-}$$
 (3)

These radicals can further react with <sup>3</sup>O<sub>2</sub>, thus producing •O<sub>2</sub> (eqn (4)).

$$^{\bullet}PS^{-} + {^{3}O_{2}} \rightarrow PS + {^{\bullet}O_{2}}^{-}$$
 (4)

Although \*O2 is not the main reactive cytotoxic agent and cannot cause much oxidative damage, it is an important intermediate in biological systems. •O<sub>2</sub> can produce H<sub>2</sub>O<sub>2</sub> through dismutation in the presence of superoxide dismutase or by oneelectron reduction (eqn (5)).

$${}^{\bullet}O_{2}^{-} + 2H^{+} + e^{-} \rightarrow H_{2}O_{2}$$
 (5)

Finally, H<sub>2</sub>O<sub>2</sub> can generate the highly cytotoxic hydroxyl radical (\*OH) through one-electron reduction (eqn (6)).<sup>6,7</sup>

$$H_2O_2 + e^- \rightarrow {}^{\bullet}OH + OH^-$$
 (6)

In the Type II mechanism, the energy of the triplet state PS is directly transferred to <sup>3</sup>O<sub>2</sub> due to the same electron spin multiplicity, which brings the <sup>3</sup>O<sub>2</sub> from the ground state to the excited singlet state, thus producing  ${}^{1}O_{2}$ . The energy gap between <sup>3</sup>O<sub>2</sub> and <sup>1</sup>O<sub>2</sub> is 0.98 eV, which is the energy threshold for <sup>3</sup>PS\* in PDT.3 The two types of mechanism can work simultaneously, and the ratio depends on the oxygen concentration, substrate and PS type. Generally, most PSs are based on the Type II mechanism, which results in the dependence of PDT on oxygen. The reaction product <sup>1</sup>O<sub>2</sub> is the main cytotoxic component in PDT due to its high electrophilicity. The Type I mechanism is more effective in oxygen-deficient environments. 6,76,78,79

Vibrational relaxation is the main mechanism of light-toheat conversion. During this process, electrons in the excited state relax to the ground state in a nonradiative way, causing the collision between the chromophore and the surrounding environment. Hence, part of the energy is released as heat.<sup>3,80</sup> Generally, most PTAs such as carbon-based PTAs, organic dyes and photothermal polymers generate heat via this mechanism, under light irradiation at the appropriate wavelength. 19,36,81 However, as for metals, semiconductors, and rare earth materials, the light-to-heat conversion mechanism is more complex.

For high carrier density materials such as metals, the movement of free conduction electrons can be guided by incident light, causing the polarization of electrons. The oppositely accumulated charges, in turn, form a depolarization field, which leads to the collective oscillation of electrons, namely,

surface plasmon polariton. 18,68 The surface plasmon then decays by light emission or nonradiative transition.82 In the latter case, energy is dissipated in the form of heat. This phenomenon is called localized plasmon surface resonance (LSPR), which is shown in Fig. 3c. As LSPR is related to the energy redistribution in the conduction band, it is also referred to as "intraband transition". 68 The primary control of LSPR is free electron density, which determines whether a material can have the LSPR effect in the optical region.<sup>83</sup> The LSPR frequency is slightly influenced by particle size and shape. By changing the particle morphology or introducing coupling materials, the LSPR peak can be tuned from the visible to the near-infrared (NIR) range. 68,80 The most popular LSPR materials are noble metals, such as gold and silver, because of their suitable response of light at optical frequencies. However, LSPR is not confined to metals. Semiconductors, metal oxides and quantum dots with high carrier density can also have a photothermal effect through LSPR. 83 It is worth noting that enhancing the electron density through modifications can change the major electron transition from bandgap to LSPR, thus inducing the photothermal effect. 54,84

Another mechanism is based on the bandgap transition of electrons, which mainly appears in low electron density semiconductors. Due to the interaction of molecular orbitals, semiconductors have two broad energy bands, namely the conduction band and valence band. The former is filled with electrons while the latter has no electrons. There are no energy levels between these two bands. The energy gap between the lowest energy of the conduction band and the highest energy of the valence band is called the bandgap. If the semiconductor is irradiated by photons with energy higher than or equal to the bandgap, the electron will be excited to a higher energy level in the conduction band, leaving a hole in the valence band. The electrons and holes are referred to as "hot carriers", due to their higher temperature than the lattice. When the energy of the photon is higher than the bandgap, the electron and hole will be "above-bandgap", as shown in Fig. 3d. Then, in process 1, the electron and hole will relax to the band edges through vibrational relaxation, which causes the thermalization process, thus converting energy into heat. 69,85 Hence, narrowing the bandgap can improve the photothermal effect through a longer relaxation pathway. Afterwards, the electron-hole pair will recombine near the band edge or at deep-level defect (DLD) sites (process 2).<sup>70</sup> During the recombination process, the excessive energy is transferred to phonon generation for the equilibrium of hot carriers and lattice, resulting in heat generation due to the crystal lattice vibration. DLD sites serve as the centers of nonradiative recombination. More DLDs lead to higher photon generation, thus increasing the photothermal effect.<sup>70</sup>

The last type of photothermal mechanism is based on the ladder-like energy level of rare earth ions (Fig. 3e). Similarly, the nonradiative relaxation of excited electrons to the ground state can generate heat. In rare earth doped nanocrystals, when the rare earth ion content is increased, the distance to the same ions is reduced, forming electron pathways between the same ions, which is called cross-relaxation (CR).86 CR results in the excitation and de-excitation of two neighboring ions, and then the two excited electrons relax to the ground state to produce heat, thus improving the photothermal effect of PTAs.<sup>56</sup> The energy of excited electrons can also migrate between the same ions. Once the energy is transferred to a nonradiative center, the energy will be released in the form of heat. 19 This process is called energy migration.

The light's wavelength is a critical factor that is related to the depth of light penetration, photon adsorption and the subsequent electron behaviors. The frequently used wavelength of light in phototherapy is red light (620-750 nm), NIR-I (750-1000 nm), and NIR-II (1000-1350 nm). For PSs, the wavelength is usually in the range of 650-800 nm, which is called the "tissue transparent window". Tissue penetration depth in this wavelength region is 3-10 mm.<sup>2</sup> Shorter wavelengths (<600 nm) have limited therapeutic depth and will cause skin photosensitivity, while longer wavelengths (>800 nm) cannot provide enough energy for <sup>3</sup>O<sub>2</sub> excitation. Since longer wavelengths of light have deeper penetration, the ideal wavelength of PDT is located in the deep-red region.<sup>6</sup> To further improve the tissue penetration of PDT, the PS can be modified with upconversion nanoparticles that can absorb NIR light and emit ultraviolet (UV)-vis light for PS activation. 87-89 In this way, NIR can be used as the light source. For PTAs, the desired wavelength is longer, which is located in the first biological window (700-980 nm) and the second biological window

(1000-1400 nm).19 The longer wavelength of light provides deeptissue treatment because of minimal tissue absorption and scattering.90 The absorption of PSs or PTAs is a critical factor when choosing the light source. When the irradiation wavelength is the same as the wavelength of the absorption peak, the photon absorption is enhanced. It is worth mentioning that for coordination structures, besides the interband transition mentioned above, their absorption is also influenced by various charge transfer processes such as metal-to-ligand charge transfer, ligand-to-metal charge transfer, etc. 91 The absorptions of typical PSs, PTAs and some intrinsic photodynamic or photothermal MOFs are listed in Table 1, and are summarized according to the published literature. The absorption of a material is not constant and can be tuned by different sizes and shapes or by modifications. The disease location and tissue properties should also be considered when selecting the appropriate wavelength of light.6

Whether an excited electron goes through fluorescence emission, nonradiative relaxation or enters into the triplet state depends on many factors, which requires deep insight into the mechanism of photo-induced electron transitions. The ratio between radiative and nonradiative processes depends on the distance and relative orientation of chromophores.<sup>3</sup> When the fluorescence quantum yield is low, the ratio of the other two processes is high, which means higher efficacy of phototherapy.

Table 1 Typical PSs and PTAs responding to light of specific wavelength

Porphyrin	PSs or PTAs	Absorption under specific wavelengths of light	Ref.
Chlorin         630-650 nm (Q band)           Bacteriochlorin         700-800 nm           Methylene blue         550-700 nm           Rose bengal         480-550 nm           IR780         Absorption peak at 780 nm           IR825         Absorption peak at 825 nm         93           Indocyanine green (ICG)         Absorption peak at 777 nm         94           1,3,6,8-Tetrakis(p-benzoic acid)pyrene (H,TBAPy)         Absorption peak at 777 nm         95           Tetrakis(4-carboxyphenyl)-porphyrin (TCPP)         Soret band at 419 nm         95           5,15-Di(p-benzoato)porphyrin (H₂DBP)         Soret band at 402 nm         96           5,15-Di(p-methylbenzoato)chlorin (H₂DBC)         Soret band at 402 nm         97           5,15-Di(p-methylbenzoato) (H₄TBC)         Soret band at 420 nm         97           5,15-Di(p-methylbenzoato) (H₄TBC)         Soret band at 420 nm         97           4u nanorod         Longitudinal peak in the NIR region         98           Au nanorod         Soret band at 420 nm         98           Prussian blue         Surface plasmon resonance absorption at 220-700 nm         98           Graphene         Strong absorption in the NIR region         10           Graphene oxide         Absorption peak at 227 nm         10	Porphyrin	Strong absorption band at 400 nm (Soret band)	5
Bacteriochlorin         700-800 nm         1           Methylene blue         550-700 mm         1           Rose bengal         480-550 nm         1           IR780         Absorption peak at 825 nm         93           IR825 [R825]         Absorption peak at 825 nm         93           Indocyanine green (ICG)         Absorption peak at 777 nm         94           1,3,6,8-Tetrakis(p-benzoic acid)pyrene (H₄TBAPy)         Absorption peak at 777 nm         95           Tetrakis(4-carboxyphenyl)-porphyrin (TCPP)         Soret band at 419 nm         96           5,15-Di(p-benzoato)porphyrin (H₂DBP)         Soret band at 402 nm         96           5,15-Di(p-methylbenzoato)chlorin (H₂DBC)         Soret band at 408 nm         47           5,10,15,20-Tetra(p-benzoato) (H₄TBC)         Soret band at 420 nm         97           5,10,15,20-Tetra(p-benzoato) (H₄TBC)         Soret band at 420 nm         97           4 u nanorod         Longitudinal peak in the NIR region         98           Pb nanocube         Longitudinal peak in the NIR region         98           Prussian blue         Surface plasmon resonance absorption at 220-700 nm         90           Graphene oxide         Polymorion         Non-100 nm         100           Graphene oxide         Absorption peak at 227 nm		A set of absorption bands at 600-800 nm (Q band)	
Methylene blue         550-700 nm         10           Rose bengal         480-550 nm         2           IR780         Absorption peak at 780 nm         92           IR825         Absorption peak at 825 nm         93           Indocyanine green (ICG)         Absorption peak at 777 nm         94           1,3,6,8-Tetrakis(p-benzoic acid)pyrene (H₄TBAPy)         Absorption peak at 777 nm         95           Tetrakis(4-carboxyphenyl)-porphyrin (TCPP)         Soret band at 419 nm         96           5,15-Di(p-benzoato)porphyrin (H₂DBP)         Soret band at 402 nm         9           5,15-Di(p-methylbenzoato)chlorin (H₂DBC)         Soret band at 408 nm         9           5,10,15,20-Tetra(p-benzoato) (H₄TBC)         Soret band at 420 nm         9           5,10,15,20-Tetra(p-benzoato) (H₄TBC)         Soret band at 420 nm         9           Au nanorod         LSPR peak at 520 nm         98           LSPR peak at 520 nm         98           Pussian blue         Surface plasmon resonace absorption at 220-700 nm         9           Graphene         Strong absorption in the NIR region         31           Graphene oxide         Absorption peak at 227 nm         10           Polydopamine         Absorption peak at 227 nm         10           PO-1200 nm <td< td=""><td>Chlorin</td><td>630-650 nm (Q band)</td><td></td></td<>	Chlorin	630-650 nm (Q band)	
Rose bengal         480-550 nm           IR780         Absorption peak at 780 nm         92           IR825         Absorption peak at 825 nm         93           Indocyanine green (ICG)         Absorption peak at 777 nm         94           1,3,6,8-Tetrakis/p-benzoic acid/pyrene (H₄TBAPy)         Absorption peaks at ~420 nm and ~330 nm         95           Tetrakis(4-carboxyphenyl)-porphyrin (TCPP)         Soret band at 419 nm         96           5,15-Di(p-benzoato)porphyrin (H₂DBP)         Soret band at 402 nm         9           5,15-Di(p-methylbenzoato)chlorin (H₂DBC)         Soret band at 408 nm         47           5,10,15,20-Tetra(p-benzoato) (H₄TBC)         Soret band at 402 nm         9           5,10,15,20-Tetra(p-benzoato) (H₄TBC)         Soret band at 402 nm         9           80 bands at 504, 534, 591, 643 nm         9           80 cret band at 400 nm         9           90 bands at 518, 546, 600, 652 nm         9           Au nanorod         Longitudinal peak in the NIR region         9           Punsain blue         Soret band at 420 nm         9           Prussian blue         Soret band at 420 nm         10           Graphene         Strong absorption in the NIR region         10           Graphene oxide         Absorption peak at 227 nm         10	Bacteriochlorin	700-800 nm	
$ \begin{array}{c} IR780 \\ IR825 $	Methylene blue	550-700 nm	10
$ \begin{array}{llllllllllllllllllllllllllllllllllll$	Rose bengal	480-550 nm	
$ \begin{array}{llllllllllllllllllllllllllllllllllll$	IR780	Absorption peak at 780 nm	92
$\begin{array}{c} 1,3,6,8\text{-Tetrakis}(p\text{-benzoic acid}) \text{pyrene } (\text{H}_4\text{TBAPy}) & \text{Absorption peaks at $\sim$420 nm and $\sim$330 nm} & 95 \\ \text{Tetrakis}(4\text{-carboxyphenyl})\text{-porphyrin } (\text{TCPP}) & \text{Soret band at }419 nm} & 96 \\ \text{Q bands at }513,548,589,645 nm} \\ \text{Soret band at }402 nm} & 55 \\ \text{Q bands at }505,540,566,619 nm} & 55 \\ \text{Q bands at }505,540,566,619 nm} & 57 \\ \text{Soret band at }408 nm} & 97 \\ \text{Q bands at }504,534,591,643 nm} & 97 \\ \text{Q bands at }504,591,643 nm} & 99 \\ \text{Polyadroin }104,104,104,104,104,104} & 99 \\ \text{Polyadroin }104,104,104,104,104,104,104} & 99 \\ \text{Polyadroin }104,104,104,104,104,104,104,104,104,104,$	IR825	Absorption peak at 825 nm	93
$ \begin{array}{llllllllllllllllllllllllllllllllllll$	Indocyanine green (ICG)	Absorption peak at 777 nm	94
$ \begin{array}{llllllllllllllllllllllllllllllllllll$	1,3,6,8-Tetrakis(p-benzoic acid)pyrene ( $H_{4}TBAPy$ )	Absorption peaks at $\sim$ 420 nm and $\sim$ 330 nm	95
$\begin{array}{llllllllllllllllllllllllllllllllllll$		Soret band at 419 nm	96
$\begin{array}{c} \text{Q bands at 505, 540, 566, 619 nm} \\ \text{Soret band at 408 nm} \\ \text{Q bands at 504, 534, 591, 643 nm} \\ \text{Soret band at 420 nm} \\ \text{Q bands at 518, 546, 600, 652 nm} \\ \text{Au nanorod} \\ \text{LSPR peak at 520 nm} \\ \text{Longitudinal peak in the NIR region} \\ \text{Por nanocube} \\ \text{Prussian blue} \\ \text{Graphene} \\ \text{Strong absorption in the NIR region} \\ \text{Strong absorption peak at 712 nm} \\ \text{100} \\ \text{Graphene} \\ \text{Strong absorption in the NIR region} \\ \text{101} \\ \text{Polypyrrole} \\ \text{Polydopamine} \\ \text{PON-224 (composed of TCPP ligand and Zr node)} \\ \text{DBP-UiO MOF (composed of H}_2\text{DBP ligand and Hf node)} \\ \text{DBP-UiO MOF (composed of H}_2\text{DBC ligand and Hf node)} \\ \text{DBC-Hf MOF (composed of Fc(COOH)}_2 ligand and Zr node)} \\ \text{Strong absorption at 220-700 nm} \\ \text{Strong absorption peak at 227 nm} \\ \text{101} \\ \text{201} \\ \text{301} \\ \text{302} \\ \text{303} $		Q bands at 513, 548, 589, 645 nm	
$\begin{array}{c} \text{Q bands at 505, 540, 566, 619 nm} \\ \text{Soret band at 408 nm} \\ \text{Q bands at 504, 534, 591, 643 nm} \\ \text{Soret band at 420 nm} \\ \text{Q bands at 518, 546, 600, 652 nm} \\ \text{Au nanorod} \\ \text{LSPR peak at 520 nm} \\ \text{Longitudinal peak in the NIR region} \\ \text{Por nanocube} \\ \text{Prussian blue} \\ \text{Graphene} \\ \text{Strong absorption in the NIR region} \\ \text{Strong absorption peak at 712 nm} \\ \text{100} \\ \text{Graphene} \\ \text{Strong absorption in the NIR region} \\ \text{101} \\ \text{Polypyrrole} \\ \text{Polydopamine} \\ \text{PON-224 (composed of TCPP ligand and Zr node)} \\ \text{DBP-UiO MOF (composed of H}_2\text{DBP ligand and Hf node)} \\ \text{DBP-UiO MOF (composed of H}_2\text{DBC ligand and Hf node)} \\ \text{DBC-Hf MOF (composed of Fc(COOH)}_2 ligand and Zr node)} \\ \text{Strong absorption at 220-700 nm} \\ \text{Strong absorption peak at 227 nm} \\ \text{101} \\ \text{201} \\ \text{301} \\ \text{302} \\ \text{303} $	5,15-Di(p-benzoato)porphyrin (H <sub>2</sub> DBP)		55
$\begin{array}{llllllllllllllllllllllllllllllllllll$	, d )1 1 5 (2 )	O bands at 505, 540, 566, 619 nm	
$\begin{array}{c} Q \text{ bands at } 504, 534, 591, 643 \text{ nm} \\ 5,10,15,20\text{-Tetra}(p\text{-benzoato}) \left( \text{H}_4\text{TBC} \right) & \text{Soret band at } 420 \text{ nm} \\ Q \text{ bands at } 518, 546, 600, 652 \text{ nm} \\ \text{LSPR peak at } 520 \text{ nm} \\ \text{Longitudinal peak in the NIR region} \\ \text{Pb nanocube} & \text{Surface plasmon resonance absorption at } 220-700 \text{ nm} & 99 \\ \text{Prussian blue} & \text{500-900 nm} \text{ with an absorption peak at } 712 \text{ nm} & 100 \\ \text{Graphene} & \text{Strong absorption in the NIR region} & 31 \\ \text{Graphene oxide} & \text{Absorption peak at } 227 \text{ nm} & 101 \\ \text{Polypyrrole} & \text{700-1200 nm} & 102 \\ \text{Polydopamine} & \text{Absorption peak centered at } 500-800 \text{ nm} & 53 \\ \text{PCN-224 (composed of TCPP ligand and Zr node)} & Q \text{ bands at } 515, 550, 591, 646 \text{ nm} & 96 \\ \text{DBP-UiO MOF (composed of H}_2\text{DBP ligand and Hf node)} & Q \text{ bands at } 510, 544, 579, 634 \text{ nm} & 55 \\ \text{DBC-UiO MOF (composed of Fc(COOH)}_2 \text{ ligand and Hf node})} & Q \text{ bands at } 520, 548, 600, 653 \text{ nm} & 97 \\ \text{Zr-Ferrocene MOF (composed of Fc(COOH)}_2 \text{ ligand and Zr node})} & 350-4350 \text{ nm} & 103 \\ 5,10,15,20\text{-Tetrakis}(4\text{-pyridyl})-21\text{H},23\text{-porphine}} & \text{TPyP} \\ \text{Soret band at } 440 \text{ nm} & 104 \\ \text{Pd-TPyP MOF (composed of TPyP ligand and Pd node)} & \text{Soret band at } 440 \text{ nm} & 104 \\ \text{Soret band at } 440 \text{ nm} & 1$	5.15-Di(p-methylbenzoato)chlorin (H <sub>2</sub> DBC)		47
$\begin{array}{llllllllllllllllllllllllllllllllllll$	(2 )	O bands at 504, 534, 591, 643 nm	
Au nanorod  LSPR peak at 520 nm Longitudinal peak in the NIR region  Pb nanocube Prussian blue Graphene Graphene Graphene oxide Polypyrrole Polydopamine Polydopamine PCN-224 (composed of TCPP ligand and Zr node) DBP-UiO MOF (composed of H <sub>2</sub> DBP ligand and Hf node) DBP-UiO MOF (composed of Fc(COOH) <sub>2</sub> ligand and Zr node) DBC-UiO MOF (composed of Fc(COOH) <sub>2</sub> ligand and Zr node) Soret band at 418 nm Soret band at 440 nm  Q bands at 518, 546, 600, 652 nm LSPR peak at 520 nm LSPR peak at 520 nm LOSPR peak at 520 nm Sufface plasmon resonance absorption at 220-700 nm 99 Surface plasmon resonance absorption at 220-700 nm 99 Strong absorption in the NIR region 31 Absorption peak at 227 nm 100 200 200 200 200 200 200 200 200 200	5,10,15,20-Tetra(p-benzoato) (H <sub>4</sub> TBC)		97
Au nanorod  LSPR peak at 520 nm  Longitudinal peak in the NIR region  Pb nanocube  Surface plasmon resonance absorption at 220–700 nm  Prussian blue  Graphene  Graphene  Graphene oxide  Polypyrrole  Polydopamine  Polydopamine  Polydoposed of TCPP ligand and Zr node)  DBP-UiO MOF (composed of H <sub>2</sub> DBC ligand and Hf node)  DBP-UiO MOF (composed of H <sub>2</sub> DBC ligand and Hf node)  DBC-UiO MOF (composed of Fc(COOH) <sub>2</sub> ligand and Zr node)  TBC-Hf MOF (composed of Fc(COOH) <sub>2</sub> ligand and Zr node)  TCP-Ferrocene MOF (composed of Fc(COOH) <sub>2</sub> ligand and Zr node)  Soret band at 418 nm  Soret band at 440 nm  Surface plasmon resonance absorption at 220–700 nm  POP  Popon mwith an absorption peak at 712 nm  100  Absorption peak at 227 nm  101  Absorption peak centered at 500–800 nm  53  PCN-224 (composed of TCPP ligand and Hf node)  Q bands at 515, 550, 591, 646 nm  96  DBP-UiO MOF (composed of H <sub>2</sub> DBC ligand and Hf node)  Q bands at 508, 544, 579, 634 nm  97  TC-Ferrocene MOF (composed of Fc(COOH) <sub>2</sub> ligand and Zr node)  5,10,15,20-Tetrakis(4-pyridyl)-21H,23H-porphine (TPyP)  Soret band at 418 nm  104  Pd-TPyP MOF (composed of TPyP ligand and Pd node)  Soret band at 440 nm	, , , , , , , , , , , , , , , , , , ,	O bands at 518, 546, 600, 652 nm	
Longitudinal peak in the NIR region  Pb nanocube  Pussian blue  Surface plasmon resonance absorption at 220–700 nm  99  Prussian blue  Strong absorption in the NIR region  Strong absorption in the NIR region  31  Graphene oxide  Absorption peak at 227 nm  101  Polypyrrole  Polydopamine  Absorption peak centered at 500–800 nm  53  PCN-224 (composed of TCPP ligand and Zr node)  DBP-UiO MOF (composed of H <sub>2</sub> DBP ligand and Hf node)  DBC-UiO MOF (composed of H <sub>2</sub> DBC ligand and Hf node)  DBC-UiO MOF (composed of H <sub>4</sub> TBC ligand and Hf node)  TBC-Hf MOF (composed of Fc(COOH) <sub>2</sub> ligand and Zr node)  Zr-Ferrocene MOF (composed of Fc(COOH) <sub>2</sub> ligand and Zr node)  Soret band at 418 nm  104  Pd-TPyP MOF (composed of TPyP ligand and Pd node)  Soret band at 440 nm	Au nanorod		98
Pb nanocube Pussian blue Surface plasmon resonance absorption at 220–700 nm Prussian blue Strong absorption in the NIR region 31 Graphene oxide Absorption peak at 227 nm 101 Polypyrrole 700–1200 nm 102 Polydopamine PCN-224 (composed of TCPP ligand and Zr node) DBP-UiO MOF (composed of H <sub>2</sub> DBP ligand and Hf node) DBC-UiO MOF (composed of H <sub>2</sub> DBC ligand and Hf node) DBC-UiO MOF (composed of H <sub>2</sub> DBC ligand and Hf node) DBC-UiO MOF (composed of Fc(COOH) <sub>2</sub> ligand and Zr node)  Zr-Ferrocene MOF (composed of Fc(COOH) <sub>2</sub> ligand and Zr node) Soret band at 418 nm 104 Pd-TPyP MOF (composed of TPyP ligand and Pd node) Soret band at 440 nm			
Prussian blue 500–900 nm with an absorption peak at 712 nm 100 Graphene Strong absorption in the NIR region 31 Graphene oxide Absorption peak at 227 nm 101 Polypyrrole 700–1200 nm 102 Polydopamine Absorption peak centered at 500–800 nm 53 PCN-224 (composed of TCPP ligand and Zr node) Q bands at 515, 550, 591, 646 nm 96 DBP-UiO MOF (composed of H <sub>2</sub> DBP ligand and Hf node) Q bands at 510, 544, 579, 634 nm 55 DBC-UiO MOF (composed of H <sub>2</sub> DBC ligand and Hf node) Q bands at 508, 545, 592, 646 nm 57 TBC-Hf MOF (composed of H <sub>4</sub> TBC ligand and Hf node) Q bands at 520, 548, 600, 653 nm 97 Zr-Ferrocene MOF (composed of Fc(COOH) <sub>2</sub> ligand and Zr node) 350–1350 nm 103 5,10,15,20-Tetrakis(4-pyridyl)-21H,23H-porphine (TPyP) Soret band at 418 nm 104 Pd-TPyP MOF (composed of TPyP ligand and Pd node) Soret band at 440 nm 104	Pb nanocube		99
Graphene oxide Strong absorption in the NIR region 31 Graphene oxide Absorption peak at 227 nm 101 Polypyrrole 700–1200 nm 102 Polydopamine Absorption peak centered at 500–800 nm 53 PCN-224 (composed of TCPP ligand and Zr node) Q bands at 515, 550, 591, 646 nm 96 DBP-UiO MOF (composed of H <sub>2</sub> DBP ligand and Hf node) Q bands at 510, 544, 579, 634 nm 55 DBC-UiO MOF (composed of H <sub>2</sub> DBC ligand and Hf node) Q bands at 508, 545, 592, 646 nm 57 DBC-Hf MOF (composed of H <sub>4</sub> TBC ligand and Hf node) Q bands at 520, 548, 600, 653 nm 97 Zr-Ferrocene MOF (composed of Fc(COOH) <sub>2</sub> ligand and Zr node) 350–1350 nm 103 5,10,15,20-Tetrakis(4-pyridyl)-21H,23H-porphine (TPyP) Soret band at 418 nm 104 Pd-TPyP MOF (composed of TPyP ligand and Pd node) Soret band at 440 nm 104	Prussian blue		100
Graphene oxide  Absorption peak at 227 nm  101  Polypyrrole  700–1200 nm  102  Polydopamine  Absorption peak centered at 500–800 nm  53  PCN-224 (composed of TCPP ligand and Zr node)  DBP-UiO MOF (composed of H <sub>2</sub> DBP ligand and Hf node)  DBC-UiO MOF (composed of H <sub>2</sub> DBC ligand and Hf node)  DBC-UiO MOF (composed of H <sub>2</sub> DBC ligand and Hf node)  DBC-UiO MOF (composed of H <sub>2</sub> DBC ligand and Hf node)  DBC-UiO MOF (composed of H <sub>2</sub> DBC ligand and Hf node)  DBC-UiO MOF (composed of F <sub>2</sub> DBC ligand and Hf node)  DBC-UiO MOF (composed of F <sub>2</sub> DBC ligand and Hf node)  DBC-UiO MOF (composed of F <sub>2</sub> DBC ligand and Hf node)  DBC-UiO MOF (composed of F <sub>2</sub> DBC ligand and Hf node)  DBC-UiO MOF (composed of F <sub>2</sub> DBC ligand and Hf node)  DBC-UiO MOF (composed of H <sub>2</sub> DBC ligand and Hf node)  DBC-UiO MOF (composed of H <sub>2</sub> DBC ligand and Hf node)  DBC-UiO MOF (composed of H <sub>2</sub> DBC ligand and Hf node)  DBC-UiO MOF (composed of H <sub>2</sub> DBC ligand and Hf node)  DBC-UiO MOF (composed of H <sub>2</sub> DBC ligand and Hf node)  DBC-UiO MOF (composed of H <sub>2</sub> DBC ligand and Hf node)  DBC-UiO MOF (composed of H <sub>2</sub> DBC ligand and Hf node)  DBC-UiO MOF (composed of H <sub>2</sub> DBC ligand and Hf node)  DBC-UiO MOF (composed of H <sub>2</sub> DBC ligand and Hf node)  DBC-UiO MOF (composed of H <sub>2</sub> DBC ligand and Hf node)  DBC-UiO MOF (composed of H <sub>2</sub> DBC ligand and Hf node)  DBC-UiO MOF (composed of H <sub>2</sub> DBC ligand and Hf node)  DBC-UiO MOF (composed of H <sub>2</sub> DBC ligand and Hf node)  DBC-UiO MOF (composed of H <sub>2</sub> DBC ligand and Hf node)  DBC-UiO MOF (composed of H <sub>2</sub> DBC ligand and Hf node)  DBC-UiO MOF (composed of H <sub>2</sub> DBC ligand and Hf node)  DBC-UiO MOF (composed of H <sub>2</sub> DBC ligand and Hf node)  DBC-UiO MOF (composed of H <sub>2</sub> DBC ligand and Hf node)  DBC-UiO MOF (composed of H <sub>2</sub> DBC ligand and Hf node)  DBC-UiO MOF (composed of H <sub>2</sub> DBC ligand and Hf node)  DBC-UiO MOF (composed of H <sub>2</sub> DBC ligand and Hf node)  DBC-UIO MOF (composed of H <sub>2</sub> DBC ligand and Hf node)  DBC-UIO MOF (composed of H <sub>2</sub> DBC ligand and Hf node)  DBC-UIO MOF (composed of H <sub>2</sub> DBC ligand and Hf node)  DBC-UIO MOF (composed of H	Graphene		31
Polypyrrole 700–1200 nm 102 Polydopamine Absorption peak centered at 500–800 nm 53 PCN-224 (composed of TCPP ligand and Zr node) Q bands at 515, 550, 591, 646 nm 96 DBP-UiO MOF (composed of H <sub>2</sub> DBP ligand and Hf node) Q bands at 510, 544, 579, 634 nm 55 DBC-UiO MOF (composed of H <sub>2</sub> DBC ligand and Hf node) Q bands at 508, 545, 592, 646 nm 47 TBC-Hf MOF (composed of H <sub>4</sub> TBC ligand and Hf node) Q bands at 520, 548, 600, 653 nm 97 Zr-Ferrocene MOF (composed of Fc(COOH) <sub>2</sub> ligand and Zr node) 350–1350 nm 103 5,10,15,20-Tetrakis(4-pyridyl)-21H,23H-porphine (TPyP) Soret band at 418 nm 104 Pd-TPyP MOF (composed of TPyP ligand and Pd node) Soret band at 440 nm 104			
Polydopamine Absorption peak centered at 500–800 nm 53 PCN-224 (composed of TCPP ligand and Zr node) Q bands at 515, 550, 591, 646 nm 96 DBP-UiO MOF (composed of H <sub>2</sub> DBP ligand and Hf node) Q bands at 510, 544, 579, 634 nm 55 DBC-UiO MOF (composed of H <sub>2</sub> DBC ligand and Hf node) Q bands at 508, 545, 592, 646 nm 47 DBC-Hf MOF (composed of H <sub>4</sub> TBC ligand and Hf node) Q bands at 520, 548, 600, 653 nm 97 Zr-Ferrocene MOF (composed of Fc(COOH) <sub>2</sub> ligand and Zr node) 350–1350 nm 103 5,10,15,20-Tetrakis(4-pyridyl)-21H,23H-porphine (TPyP) Soret band at 418 nm 104 Pd-TPyP MOF (composed of TPyP ligand and Pd node) Soret band at 440 nm 104			102
PCN-224 (composed of TCPP ligand and Zr node)  Q bands at 515, 550, 591, 646 nm  96  DBP-UiO MOF (composed of H <sub>2</sub> DBP ligand and Hf node)  Q bands at 510, 544, 579, 634 nm  55  DBC-UiO MOF (composed of H <sub>2</sub> DBC ligand and Hf node)  Q bands at 508, 545, 592, 646 nm  47  TBC-Hf MOF (composed of H <sub>4</sub> TBC ligand and Hf node)  Q bands at 520, 548, 600, 653 nm  97  Zr-Ferrocene MOF (composed of Fc(COOH) <sub>2</sub> ligand and Zr node)  5,10,15,20-Tetrakis(4-pyridyl)-21H,23H-porphine (TPyP)  Soret band at 418 nm  104  Pd-TPyP MOF (composed of TPyP ligand and Pd node)  Soret band at 440 nm		Absorption peak centered at 500–800 nm	
DBP-UiO MOF (composed of H <sub>2</sub> DBP ligand and Hf node) Q bands at 510, 544, 579, 634 nm 55 DBC-UiO MOF (composed of H <sub>2</sub> DBC ligand and Hf node) Q bands at 508, 545, 592, 646 nm 47 TBC-Hf MOF (composed of H <sub>4</sub> TBC ligand and Hf node) Q bands at 520, 548, 600, 653 nm 97 Zr-Ferrocene MOF (composed of Fc(COOH) <sub>2</sub> ligand and Zr node) 5,10,15,20-Tetrakis(4-pyridyl)-21H,23H-porphine (TPyP) Soret band at 418 nm 104 Pd-TPyP MOF (composed of TPyP ligand and Pd node) Soret band at 440 nm			
DBC-UiO MOF (composed of $H_2$ DBC ligand and Hf node) Q bands at 508, 545, 592, 646 nm 97 TBC-Hf MOF (composed of $H_4$ TBC ligand and Hf node) Q bands at 520, 548, 600, 653 nm 97 Zr-Ferrocene MOF (composed of Fc(COOH) <sub>2</sub> ligand and Zr node) 350–1350 nm 103 $5,10,15,20$ -Tetrakis(4-pyridyl)-21H,23H-porphine (TPyP) Soret band at 418 nm 104 Pd-TPyP MOF (composed of TPyP ligand and Pd node) Soret band at 440 nm 104			
TBC-Hf MOF (composed of $H_4$ TBC ligand and Hf node) Q bands at 520, 548, 600, 653 nm 97 Zr-Ferrocene MOF (composed of Fc(COOH) $_2$ ligand and Zr node) 350–1350 nm 103 5,10,15,20-Tetrakis(4-pyridyl)-21H,23H-porphine (TPyP) Soret band at 418 nm 104 Pd-TPyP MOF (composed of TPyP ligand and Pd node) Soret band at 440 nm 104			
Zr-Ferrocene MOF (composed of Fc(COOH)2 ligand and Zr node)350-1350 nm1035,10,15,20-Tetrakis(4-pyridyl)-21H,23H-porphine (TPyP)Soret band at 418 nm104Pd-TPyP MOF (composed of TPyP ligand and Pd node)Soret band at 440 nm104		, , ,	97
5,10,15,20-Tetrakis(4-pyridyl)-21H,23H-porphine (TPyP) Soret band at 418 nm Pd-TPyP MOF (composed of TPyP ligand and Pd node) Soret band at 440 nm 104			
Pd-TPyP MOF (composed of TPyP ligand and Pd node)  Soret band at 440 nm  104			
		Absorption band at 800–1000 nm	

Intersystem crossing can be promoted by combining PSs with heavy atoms due to enhanced intramolecular spin-orbit coupling or intermolecular collision, namely the heavy atom effect.<sup>3</sup> Another requirement of PDT is that the energy of the triplet state should be higher than 0.98 eV, which corresponds to the energy between <sup>1</sup>O<sub>2</sub> and  ${}^{3}O_{2}$ . On the other hand, to improve the photothermal effect, intersystem crossing and fluorescence should be reduced. Chelation with metals such as Mn and Cu can quench the fluorescence and ROS generation of PSs, 105,106 thus promoting electrons to go through nonradiative decay pathways.80 Moreover, aggregates of PSs formed by  $\pi$ -stacking can decrease the triplet state lifetime and ROS quantum yield of PSs, which improves the ratio of nonradiative relaxation.<sup>5,80</sup> As PDT is dependent on oxygen, reducing the oxygen content by clamping also hinders the PDT effect of PSs. 1

## Photodynamic therapy

### 3.1 Intrinsic photodynamic MOF

3.1.1 Porphyrin-based MOFs. Using porphyrin and its derivatives as MOF ligands is a straightforward way to fabricate intrinsic photodynamic MOFs. The frequently-used porphyrin ligands are presented in Fig. 4, which are mostly carboxyl-containing derivatives of porphyrin, chlorin and bacteriochlorin, etc. 47,55,62,97,107,108 The number of  $\pi$  electrons in porphyrin, chlorin and bacteriochlorin is 22, 20 and 18, respectively. The absorption of porphyrins red-shifts with the decrease in  $\pi$  electrons. Hence, the photo-response of MOFs can be tuned by using different porphyrin linkers. Compared to traditional porphyrin PSs, porphyrin-based MOFs are more efficient and potent. Firstly, porphyrins are regularly arranged in the MOF structure with high loading content, which prevents PSs aggregation. The channels and pores in MOFs render facile diffusion of <sup>3</sup>O<sub>2</sub> and <sup>1</sup>O<sub>2</sub>. Using metal nodes such as Hf can improve intersystem crossing through the heavy atom effect, thus increasing <sup>1</sup>O<sub>2</sub> yields. However, despite these advantages, the morphology of metal-organic nanocomposites is hard to control. The insolubility

HOOC H<sub>2</sub>DBF

Fig. 4 Typical porphyrins and their derivatives, which have been used as MOF ligands.

and aggregation of PS in common solvents also add difficulty to the MOF synthesis and porosity control. 49,109 To date, many porphyrin-based MOFs have been synthesized and applied in PDT as PSs, which are given in Table 2.

The first report of porphyrin-based MOFs for PDT was made by Lin's group.<sup>55</sup> They synthesized DBP-UiO constructed by 5,15-di(p-benzoato)porphyrin (H2DBP) ligands and Hf nodes, with a H<sub>2</sub>DBP loading of 77 wt%. DBP-UiO has nanoplate morphology, which was  $\sim 100$  nm in diameter and  $\sim 10$  nm in thickness. The high-Z ion, Hf4+, promoted the intersystem crossing of the PDT system. Hence, the absorption peaks of DBP-UiO all red-shifted and the <sup>1</sup>O<sub>2</sub> generation of DBP-UiO was at least 2 times higher as compared to H<sub>2</sub>DBP. In vivo tests manifested the excellent antitumor effect of DBP-UiO, i.e., the tumor decreased in size by 50 times, or was completely eradicated after PDT treatment. However, the lowest-energy Q band absorption of Hf-DBP was close to the edge of the "tissue transparent window", and its extinction coefficient was 2200 M<sup>-1</sup> cm<sup>-1</sup>, which means the light source had limited penetration in the tissue and the light absorption of DBP-UiO was not enough as well. Therefore, Lin's group then partially reduced H<sub>2</sub>DBP to generate H<sub>2</sub>DBC (H<sub>2</sub>DBC refers to 5,15-di(p-methylbenzoato)chlorin), which was used to fabricate DBC-UiO MOF (Fig. 5a).47 DBC-UiO also had nanoplate morphology, which was 100-200 nm in diameter and 3.3-7.5 nm in thickness (Fig. 5b). The lowest-energy Q band of DBC-UiO red-shifted to 646 nm (Fig. 5c), and the extinction coefficient reached 24 600 M<sup>-1</sup> cm<sup>-1</sup>, which was 11 times higher than DBP-UiO, Moreover, DBC-UiO exhibited 3-fold higher PDT efficacy and even more potent tumor eradication than DBP-UiO in the CT26 and HT28 model. Afterwards, Lin's group fabricated TBC-Hf MOF (TBC refers to 5,10,15,20-tetra(p-benzoato)), and loaded IDO inhibitor (INCB24360) in it for PDT and immunecombined therapy. 97 The lowest-energy Q band of TBC-Hf was 653 nm, which was 7 nm red-shifted as compared to the DBC-UiO. The extinction coefficient also increased to 38 500 M<sup>-1</sup> cm<sup>-1</sup>. Their results showed that TBC-Hf had the highest ROS generation among its analogues.

After these reports from Lin's group, a growing number of reports about MOF-based PSs came out. Among them, the porous coordination network (PCN) is an important branch, which is composed of Zr clusters (mostly octahedral Zr<sub>6</sub> clusters) and the tetrakis(4-carboxyphenyl)-porphyrin (TCPP) ligand. Due to its excellent ROS generation ability, biodegradability and stability in aqueous solution, etc., 115 this kind of MOF is becoming the most popular photodynamic MOF as indicated in Table 2. Park et al. successfully fabricated PCN-224 of various sizes from 30 to 190 nm by adding different concentrations of benzoic acid (Fig. 5d).58 When the particle size of PCN-224 was 90 nm, the cellular uptake in HeLa cells was the highest (Fig. 5e). Under the irradiation of 420 nm and 630 nm lasers, PCN-224 of 90 nm in size also had the highest PDT efficacy of around 80% in cells due to the better contact of intracellular O2 with PSs (Fig. 5f). Then, the Zr<sub>6</sub> cluster was further functionalized with folic acid by coordination between the carboxyl of the folic acid and Zr<sub>6</sub> clusters for active targeting (Fig. 5g). In folate receptorabundant cells such as ovarian tumors, the attachment of folic

**Review Article** 

Table 2 Summary of recent porphyrin-based MOFs in PDT. Particle size was measured by SEM (scanning electron microscopy), TEM (transmission electron microscopy) or DLS (dynamic light scattering)

	Organic ligands	Materials for decoration	Particle size	Irradiation wavelength	Additional functions	Ref.
Zr <sup>4+</sup>	TCPP	Folic acid	30–190 nm	420 nm and 630 nm	Targeting	58
$\mathrm{Zr}^{4^+}$	TCPP	NaFY <sub>4</sub> :Yb/Er, thiol-PEG	$52.1 \pm 9.8$ nm for PCN-224	980 nm	Upconversion	96
Zr <sup>4+</sup>	ТСРР	Glucose oxidase, catalase, cancer cell membrane	227.5 nm	660 nm	Starvation therapy, targeting	62
$\mathrm{Zr}^{4^+}$	TCPP	PDA, Pt NPs, folic acid	250 nm	660 nm	O <sub>2</sub> supply, targeting	110
$Zr^{4+}$	ТСРР	Tirapazamine, cancer cell membrane		660 nm	Bioreductive therapy, targeting, immune escape	111
$\mathrm{Zr}^{4^+}$	TCPP	Pt NPs, HOOC-PEG- COOH	90 nm	638 nm	$O_2$ supply	48
$\mathrm{Zr}^{4^+}$	TCPP	L-Arg, cancer cell membrane	105 nm for PCN-224	660 nm	Gas therapy	112
$Zr^{4+}$	TCPP	Ag ions, HA	85 nm for PCN-224	Visible light	Bacteria killing	113
Zr <sup>4+</sup>	TCPP	Apatinib, MnO <sub>2</sub> , cancer cell membrane	140.5 nm	660 nm	Angiogenesis inhibition, GSH depletion, immune escape, targeting	60
$\mathrm{Zr}^{^{4+}}$	TCPP	CeO <sub>2</sub>	190 nm	638 nm	Biofilm inhibition	114
$\mathrm{Zr}^{4^+}$	TCPP	DOX, HA	$\sim$ 250 $\pm$ 20 nm	640 nm	Targeting, enzyme responsive drug release	115
$\mathrm{Zr}^{4+}$	TCPP	_	4.0 nm	650 nm	Renal clearance	116
$\mathrm{Zr}^{4+}$	TCPP	PCL	100 nm	510 nm	Bacteria killing	117
$\mathrm{Zr}^{4^+}$	TCPP	DOX, galactose, PEG	$121.2 \pm 3.7 \text{ nm}$	660 nm	Targeting, drug loading	118
Zr <sup>4+</sup>	TCPP	α-Cyano-4- hydroxycinnamate, HA	152.4 nm	660 nm	Hypoxia alleviation, targeting, lactate-fueled respiration	119
$\mathrm{Zr}^{4^+}$	TCPP	DOX, ZnO, AS1411	161.7 nm	650 nm	Drug loading, targeting	120
$Zr^{4+}$	TCPP	MnFe <sub>2</sub> O <sub>4</sub> , PEG	~110 nm without PEG coating	660 nm	O <sub>2</sub> supply, GSH depletion, MRI	57
$Zr^{4+}$	TCPP	PAH, MnO <sub>2</sub> , DOX	72 nm for PCN-222	655 nm	Drug loading, MRI, GSH depletion	121
$Zr^{4+}$	TCPP	Pt NPs, Au NPs, folic acid	147.5 nm	671 nm	Starvation therapy, targeting	63
$\mathrm{Zr}^{4^+}$	TCPP	Alkaloid piperlongumine, cancer cell membrane		660 nm	Thioredoxin reductase inhibition, targeting	61
Zr <sup>4+</sup>	TCPP	MnO <sub>2</sub> nanosheet, cell membrane	105 nm without cell membrane coating	409 nm	O <sub>2</sub> supply, MRI, targeting	122
Zr <sup>4+</sup>	TCPP	Acriflavine, cytosine- phosphate-guanine, HA	105.4 nm	670 nm	Immunotherapy	123
$\mathrm{Zr}^{4+}$	PtTCPP	Cancer cell membrane	150.5 nm	532 nm	Homologous targeting, O2 sensing	124
Zr <sup>4+</sup>	MnTCPP	_	$300 \times 130 \text{ nm}$ (length × width)	660 nm	MRI, O <sub>2</sub> supply	125
Zr <sup>4+</sup>	FeTCPP	NaYb <sub>0.92</sub> F <sub>4</sub> :Er <sub>0.08</sub> @NaYF <sub>4</sub> , Au NPs		980 nm	Upconversion, $O_2$ supply, starvation therapy	89
$\mathrm{Hf}^{4^+}$	$H_2DBP$	_	76.3 nm	640 nm	_	55
$\mathrm{Hf}^{4^+}$	H <sub>2</sub> DBC	_	128.5 nm	640 nm	_	47
$\mathrm{Hf}^{4^+}$	H <sub>4</sub> TBC	IDO inhibitor	83.2 nm for Hf-TBC	650 nm	Immunotherapy	97
Hf <sup>4+</sup>	$H_2$ DBBC	_	220 nm in size, 4.6 nm in thickness	750 nm	Photoacoustic imaging	108
$\mathrm{Zr}^{4+}$	TBP	PEG	∼50 nm	660 nm	Immunotherapy	107
Zr <sup>4+</sup>	5,10,15,20-Tetra( <i>p</i> -benzoato)bacteriochlorin	_	117.9 $\pm$ 1.4 nm	740 nm	_	126
$\mathrm{Hf}^{4^+}$	TCPP	PEG	∼130 nm	661 nm	Radiotherapy	127
$Cu^{2+}$	ZnTCPP	_	105 nm	600 nm	H <sub>2</sub> S response	106
$Al^{3+}$	CuTCPP	_	_	650 nm	GSH depletion	128
Hf <sup>4+</sup>	TCPP	Tirapazamine, DOPA- PIMA-mPEG	$163\pm5~\text{nm}$	635 nm	Drug loading, computed topography imaging	129
$Gd^{3+}$	TCPP	_	240.7 nm	660 nm	MRI	130
Fe <sup>3+</sup>	TCPP	Bovine serum albumin, sulfadiazines, MnO <sub>2</sub>	122 nm	660 nm	O <sub>2</sub> supply, MRI	131
Mn <sup>3+</sup>	TCPP		170 nm in length, 50 nm in width and 100 nm in thickness	660 nm	MRI, GSH depletion, optical imaging	105
$\mathrm{Hf}^{4^+}$	TCPP	Human serum albumin coated MnO <sub>2</sub>		Visible light	Biofilm eradication	132
Cu <sup>2+</sup>	ZnTCPP		_	635 nm	H <sub>2</sub> S response	133
Zn <sup>2+</sup>	TCPP	DOX, PEG	2 nm in thickness	660 nm	Drug loading	134
Gd <sup>3+</sup>	ZnTCPP	ZnO, MnO, MgO, Fe <sub>2</sub> O <sub>3</sub> , CuO	_	660 nm		135
Fe <sup>3+</sup>	TCPP	Dihydroartemisinin, CaCO <sub>3</sub>	382 $\pm$ 23 nm in length and 182 $\pm$ 37 nm in width	655 nm	Drug loading, MRI, oncosis therapy	136
$Mn^{2+}$	TCPP	_	150 nm	650 nm	O <sub>2</sub> supply	137
Sm <sup>3+</sup>	TCPP	Pt NPs, triphenylphosphine	~100 nm in diameter and less than 10 nm in thickness		O <sub>2</sub> supply, mitochondrion targeting	138

Published on 26 February 2021. Downloaded by Beijing University of Technology on 5/23/2021 8:44:33 AM.

Table 2 (continued)

Metal nodes	Organic ligands	Materials for decoration	Particle size	Irradiation wavelength	Additional functions	Ref.
$W^{6+}$	TBP	CpG	114.0 ± 6.7 nm	650 nm	Immunotherapy	139
Fe <sup>3+</sup>	TCPP	Fe <sub>2</sub> O <sub>3</sub> , red blood cell membrane, AS1411	110–140 nm, depending on the reaction time	660 nm	Targeting, Fenton reaction	140
Fe <sup>3+</sup>	TCPP	Bovine serum albumin, sulfonamide	160 nm	660 nm	PTT, MRI	141
$\mathrm{Zr}^{4^+}$	TCPP	Gold nanorod,	$53.8 \pm 2.1$ nm in length and $25.2 \pm 1.7$ nm in width	,	PTT, drug loading, fluorescence	142
$\mathrm{Zr}^{4^+}$	TCPP	camptothecin CuS NPs, folic acid, ICG, PAH		660 nm PDT 650 nm	imaging PTT, fluorescence imaging, pho- tothermal imaging	143
Cu <sup>2+</sup>	TCPP	_	330 nm in size and $5.1 \pm 0.3$ nm in thickness	,	PTT, MRI, infrared thermal imaging	144
$\mathrm{Zr}^{4+}$	FeTCPP	siRNA	210 nm in length	635 nm	Low-temperature PTT, photo- thermal imaging, photoacoustic imaging, computed tomography imaging	145
$\mathrm{Zr}^{4^+}$	CuTCPP	_	100 nm	660 nm	PTT	146

acid can increase the delivery efficiency of PCN-224 due to the higher cellular uptake (Fig. 5h). After folic acid modification, the PDT efficacy reached as high as 90% (Fig. 5i). Since then, PCN-224 has been widely applied as a carrier to combine PDT and other functions, which will be further discussed in Section 3.3.

Although TCPP is extensively applied as a MOF ligand, porphyrin derivatives such as H<sub>2</sub>DBP, H<sub>2</sub>DBC and H<sub>4</sub>TBC reported by Lin's group also showed high ROS generation and therapeutic efficacy. 47,55,97 Expanding the category of porphyrin-based ligands can be a promising direction for developing MOF-based PDT. Zeng et al. coordinated the tetrabenzoporphyrin (TBP) ligand with Zr<sub>6</sub> clusters, which was named TBP-nMOF (Fig. 5j). 107 Since benzoporphyrin had a larger  $\pi$  conjugation than porphyrin, the TBP-nMOF exhibited a 50 nm-red-shifted lowest-energy Q band and a 100 nmred-shifted lowest-energy emission as compared to other porphyrin MOFs (Fig. 5k). The coordination with Zr<sub>6</sub> clusters also shortened the fluorescence lifetime of TBP from 3.16 ns to 2.12 ns, due to enhanced intersystem crossing (Fig. 5l). Therefore, the <sup>1</sup>O<sub>2</sub> yield of TBP-nMOF was about 8 times higher (Fig. 5m). Zhang and coworkers fabricated DBBC-UiO, which was composed of Hf4+ nodes and 5,15-di(p-benzoato)bacteriochlorin (H<sub>2</sub>DBBC) ligands. 108 The DBBC ligand can generate  ${}^{1}O_{2}$  in an  $O_{2}$ -sufficient environment and also produce  ${}^{\bullet}O_2^-$  in hypoxia through the Type I mechanism. In the presence of superoxide dismutase, \*O2 was partially converted into the highly cytotoxic \*OH through the H2O2 disproportionation reaction. DBBC-UiO showed high cancer cell inhibition in both normoxia and hypoxia environments, proving that this MOF was O2-independent, which is desirable in tumor suppression.

The tetrapyrrole structure in porphyrin has a strong tendency to coordinate metals at the central site, forming metalloporphyrin, which is denoted as MTCPP (M is the central-coordinated metal) in this review.  $^{147}$  Metalloporphyrin ligands endow the MOF with more metal sites for synergistic functions. For example, Li *et al.* reported a MOF that can monitor  $\rm O_2$  fluctuation, which is composed of PtTCPP and  $\rm Zr_6$  clusters, and coated with a cancer cell membrane (referred to as mPPt) (Fig. 6a).  $^{124}$  The cancer cell membrane gave the mPPt immune escape ability, which protected

mPPt from immune clearance due to the antigenic profile on the membrane. In an O<sub>2</sub>-sufficient environment, the triplet phosphorescence of mPPt was quenched because the triplet PSs mainly reacted with <sup>3</sup>O<sub>2</sub> to produce <sup>1</sup>O<sub>2</sub>. In an O<sub>2</sub>-deficient environment, the PDT effect was limited, giving rise to a higher phosphorescence emission (Fig. 6b). The authors manifested that mPPT in a 1% O<sub>2</sub> atmosphere had a 6.22-fold higher phosphorescence intensity than in 100% O2, and can give a quick response to O2 fluctuation (Fig. 6c and d). This property can be used to detect O2 in vivo and realize phosphorescence imaging guidance. Another research group fabricated PCN-222 with Mn-porphyrin as ligands. 125 Mn chelation rendered PCN-222 with magnetic resonance imaging (MRI) ability due to the high spin quantum number and long electronic relaxation time. The longitudinal relaxivity was  $\sim 35.3 \text{ mM}^{-1} \text{ s}^{-1}$ (1.0 T). Moreover, the Mn-porphyrin can also decompose the surrounding H<sub>2</sub>O<sub>2</sub>, thus providing O<sub>2</sub> for <sup>1</sup>O<sub>2</sub> generation.

The most-reported Hf- and Zr-based porphyrin-MOF is stable, and can be directly applied as a PS. Other metal nodes such as Cu, Mn and Fe can quench the ROS generation of PS ligands, resulting in much less ROS generation than free PS ligands. These metals can respond to different stimuli in the microenvironment, which means that the MOF structure will decompose after the reaction, releasing active metal ions, PS ligands and drugs. The photodynamic activity of ligands is then restored. Hence, this kind of MOF can be used for stimulustriggered PDT. Besides, Mn<sup>105</sup> and Gd<sup>130</sup> nodes can also endow MOF with imaging ability. Ma et al. reported Cu-MOF with ZnTCPP as ligands. 128 Cu2+ can respond to H2S, which is of high content in human colon adenocarcinoma cells, and Cu<sup>2+</sup> can also completely quench the fluorescence of TCPP ligands. When Cu<sup>2+</sup> encountered H<sub>2</sub>S, the Cu nodes separated from the MOF structure, restoring the photosensitivity of TCPP. Wan and coworkers fabricated a Mn(III)-TCPP MOF (Fig. 6e). 105 The fluorescence and ROS generation of TCPP were temporarily blocked by Mn nodes. Glutathione (GSH) is an antioxidative ROS scavenger in tumor cells, which can weaken the potency of PDT. Mn(III)-TCPP can react with intracellular GSH, thus

**Review Article** Chem Soc Rev

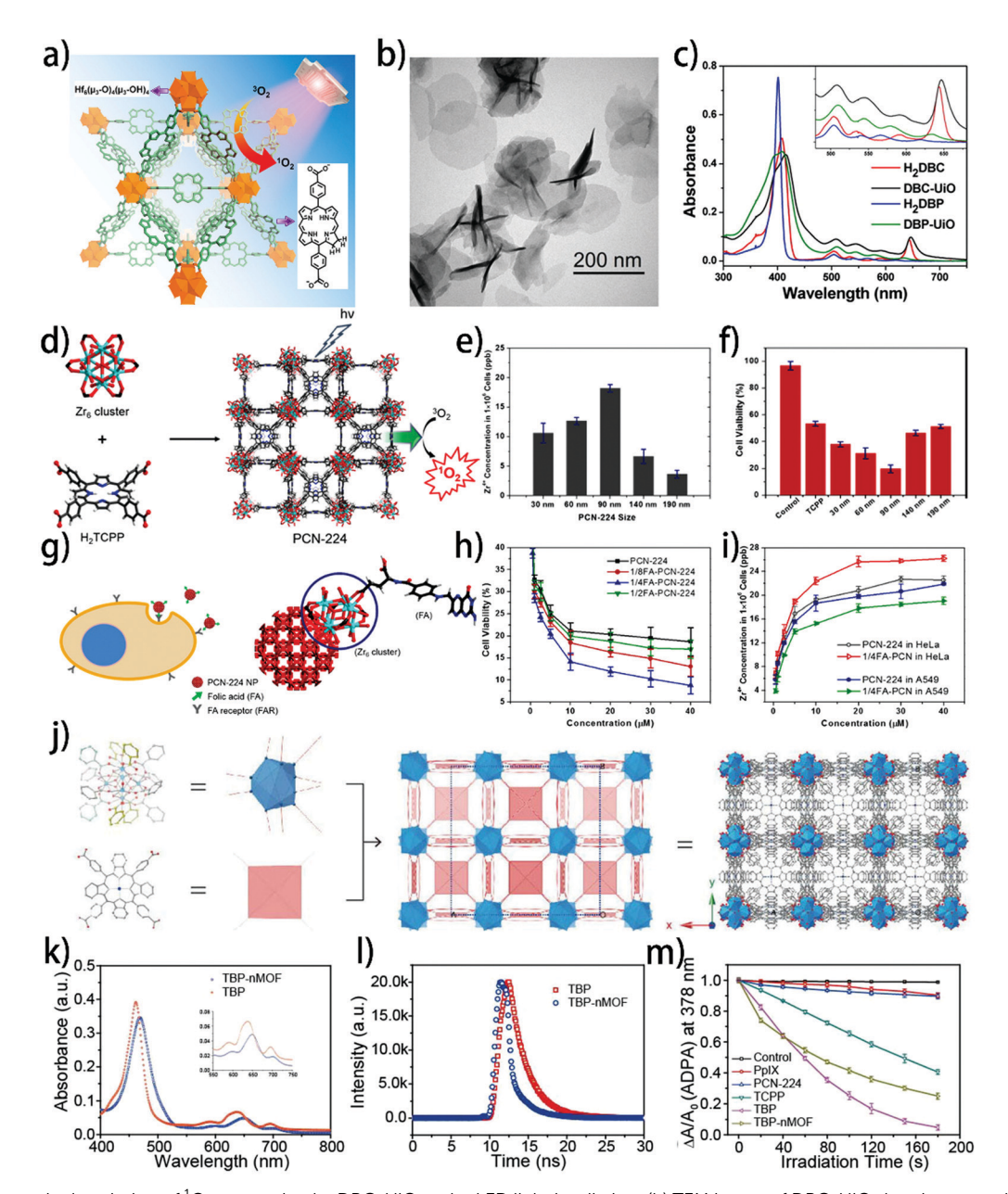


Fig. 5 (a) Schematic description of  ${}^{1}O_{2}$  generation by DBC-UiO under LED light irradiation. (b) TEM image of DBC-UiO showing nanoplate morphology. (c) UV-vis absorption spectra of H<sub>2</sub>DBC, DBC-UiO, H<sub>2</sub>DBP and DBP-UiO in DMF or 0.67 mM PBS. Reprinted with permission from ref. 47. Copyright 2015 American Chemical Society. (d) 3D nanoporous structure of PCN-224 composed of a Zr<sub>6</sub> cluster and H<sub>2</sub>TCPP ligand. (e) Size-dependent cellular uptake of PCN-224 after 24 h of incubation with HeLa cells. (f) PDT efficacy of different sized PCN-224 and free TCPP molecules. (g) Schematic illustration of FA functionalized PCN-224 and the proposed internalization. (h) ICP analysis of the cellular uptake of unfunctionalized and FA functionalized 90 nm-PCN-224 at various concentrations in HeLa and A549 cells. Incubation time = 24 h. (i) In vitro PDT efficacy of FA functionalized (FA equivalent of 0, 1/8, 1/4, 1/2) 90 nm-PCN-224 at various concentrations in HeLa cells. Irradiation at 420 nm for 30 min for PDT. Reprinted with permission from ref. 58. Copyright 2016 American Chemical Society. (j) Schematic representation of TBP-MOF, in which the 10-connected Zr<sub>6</sub> cluster and TBP ligand are simplified as a blue node and red plane, respectively. (k) UV-vis spectra of TBP and TBP-nMOF. Inset shows expanded views of the Q-band regions. (l) Time-resolved fluorescence decay traces of TBP and TBP-nMOF. (m) <sup>1</sup>O<sub>2</sub> generation by PpIX, TCPP, PCN-224, TBP, and TBP-nMOF with a 660 nm LED irradiation (30 mW cm<sup>-2</sup>). Reprinted with permission from ref. 107. Copyright 2018 American Chemical Society.

releasing Mn(II), free TCPP and glutathione disulfide (GSSG) by GSH oxidation. Hence, the fluorescence and ROS generation of TCPP was restored, and the PDT efficacy was protected as well due to GSH depletion. Mn nodes can also be used for MRI. Wan et al. reported an Fe-TCPP MOF that was loaded with the anticancer drug dihydroartemisinin (DHA). 136 In their work, Fe-TCPP was further covered with a CaCO3 mineralized layer that could prevent drug leakage and TCPP toxicity during transportation. The ROS generation of TCPP was temporarily quenched by Fe nodes. In an acidic environment such as the tumor area, CaCO<sub>3</sub> decomposes and releases Ca<sup>2+</sup>. In a high GSH environment, the exposed Fe<sup>3+</sup> on Fe-TCPP is reduced to

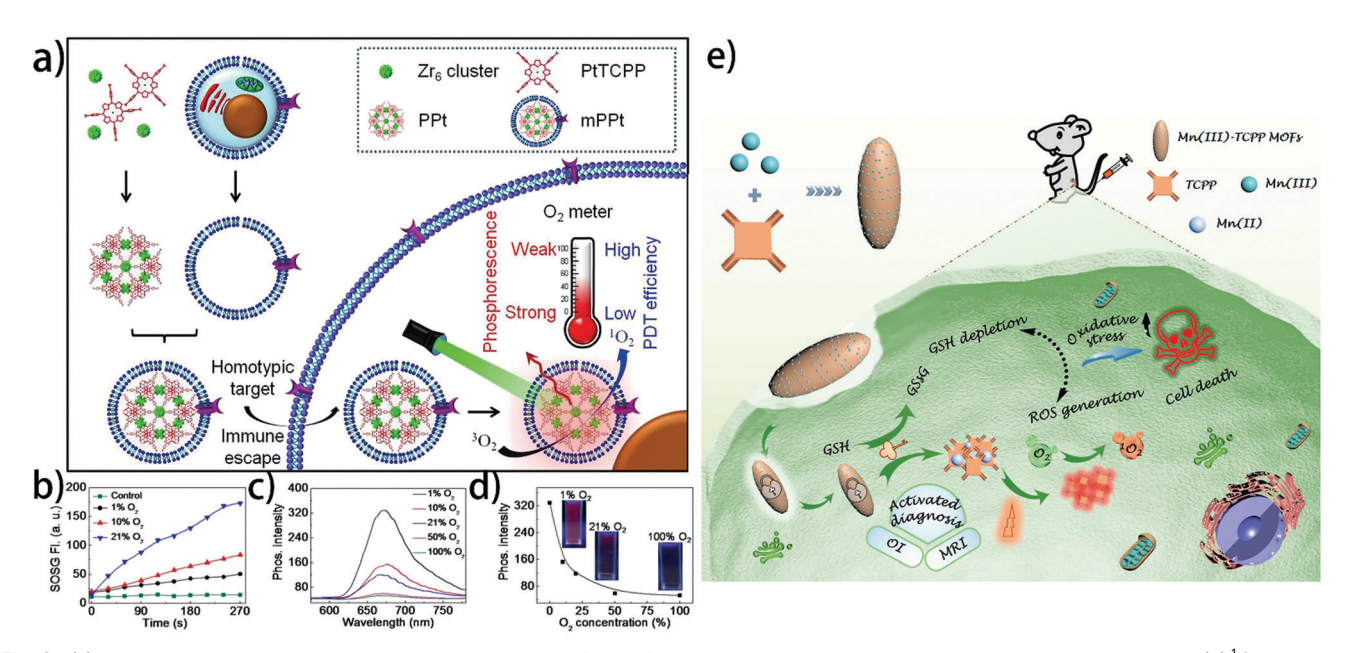


Fig. 6 (a) Preparation processes and the proposed mechanism of mPPt for cancer-targeted and phosphorescence image-guided PDT. (b) <sup>1</sup>O<sub>2</sub> generation of mPPt at various O<sub>2</sub> pressures. (c) Phosphorescence spectra of mPPt (5 µg mL<sup>-1</sup>) under various O<sub>2</sub> levels. (d) The O<sub>2</sub> concentration-related phosphorescence changes in mPPt (5 µg ml<sup>-1</sup>). Inserted: The macroscopic images of mPPt (50 µg mL<sup>-1</sup>) under the irradiation of hand-held UV lamp. Reprinted with permission from ref. 124. Copyright 2018 Elsevier. (e) Schematic illustration of an endocytosis Mn(III)-sealed MOF nanosystem for MRI- and optical imaging-guided PDT by controlled ROS generation and GSH depletion after being unlocked by overexpressed GSH in tumor cells. Reprinted with permission from ref. 105. Copyright 2019 American Chemical Society.

Fe<sup>2+</sup>, releasing free TCPP. Fe<sup>2+</sup> could activate DHA, which then generates free radicals for cancer cell killing. Moreover, as DHA could affect the  $Ca^{2+}$  pump ATPase, the  $Ca^{2+}$  from the  $CaCO_3$ coating could enter cancer cells, leading to the increase of intracellular Ca2+ concentration, which could induce oncosislike cell death. Free TCPP also restored its ROS generation. This strategy combines pH- and GSH-controlled drug activation, PDT activation and oncosis-like therapy at the same time.

3.1.2 Other photodynamic building blocks. In terms of photodynamic metal nodes, Cai and coworkers fabricated the CuTz-1 MOF composed of Cu(I) nodes and 3,5-diphenyl-1,2,4triazole ligands, which was loaded with O2. 148 F127 was coated on CuTz-1 to increase its biocompatibility. The Cu(I) and Cu(II) mixed-valence structure of MOF could induce the intervalence charge-transfer effect and d-d transition, which resulted in its absorption in the visible and NIR region. Under 808 nm NIR light irradiation, this MOF went through Type I PDT, producing \*OH and \*O<sub>2</sub> through a Fenton-like reaction. Besides, the Cu(1) could react with GSH, thus reducing the ROS loss. The loaded O<sub>2</sub> can also help to alleviate the hypoxia in the tumor environment.

Partially substituting the normal ligands of MOF with PS agents is also a feasible way to endow MOFs with photodynamic properties. This strategy leads to mixed-ligand MOFs, and even more than one PSs can be incorporated into the non-intrinsic MOF structure through the ligand-exchange process. Wang et al. substituted the 2-hydroxyterephthalic acid (H<sub>2</sub>BDC) ligand of UiO-66 with I2-BDP (carboxyl-functionalized diiodosubstituted BODIPYs) by solvent-assisted ligand exchange. 149 The final product was called UiO-PDT. According to inductively

coupled plasma-mass spectrometer (ICP-MS) tests, around 12.5% of BDC had been replaced, and the final content of I2-BDP was 31.4 wt%. After the ligand exchange, UiO-PDT showed an absorption peak at 524 nm, which was slightly shifted as compared to I2-BDP (528 nm). UiO-PDT presented moderate but lower <sup>1</sup>O<sub>2</sub> generation than that of I2-BDP because of the heterogeneous structure of the former. In another study, Zhao and coworkers used TCPP to substitute for the ligand of NU-1000, which was referred to as NT.150 NU-1000 was composed of Zr clusters and 1,3,6,8-tetrakis(p-benzoic acid)pyrene (H<sub>4</sub>TBAPy) ligand, which featured large pore sizes. About 20% of the original ligand was substituted with TCPP. After the replacement, the maximum absorption was red-shifted to 571 nm as compared to H₄TBAPy (410 nm), due to the narrowed energy gap between the highest occupied molecular orbital (HOMO) and the lowest unoccupied molecular orbital (LUMO). Hence, the ROS generation of NT was triggered under 650 nm light irradiation in their work. Park et al. in situ inserted BCDTE (1,2-bis(5-(4carbonxyphenyl)-2-methylthien-3-yl)cyclopent-1-ene) and TCPP into UiO-66 by a thermodynamic-controlled synthesis process to fabricate a photochromic switch of <sup>1</sup>O<sub>2</sub> generation (Fig. 7a). <sup>151</sup> The photoisomerization of BCDTE could switch TCPP from the <sup>1</sup>O<sub>2</sub> quenching state to the activated state. Under UV light irradiation, BCDTE had two isomers, namely, the open form and the closed form, which had different absorptions (Fig. 7b and c). When BCDTE was in the open form, TCPP in the triplet state (T<sub>1</sub>) could react with <sup>3</sup>O<sub>2</sub> to produce <sup>1</sup>O<sub>2</sub>, while the BCDTE in the closed form had another energy transfer pathway with TCPP that could hinder the reaction between TCPP and <sup>3</sup>O<sub>2</sub>, thus

**Review Article** Chem Soc Rev

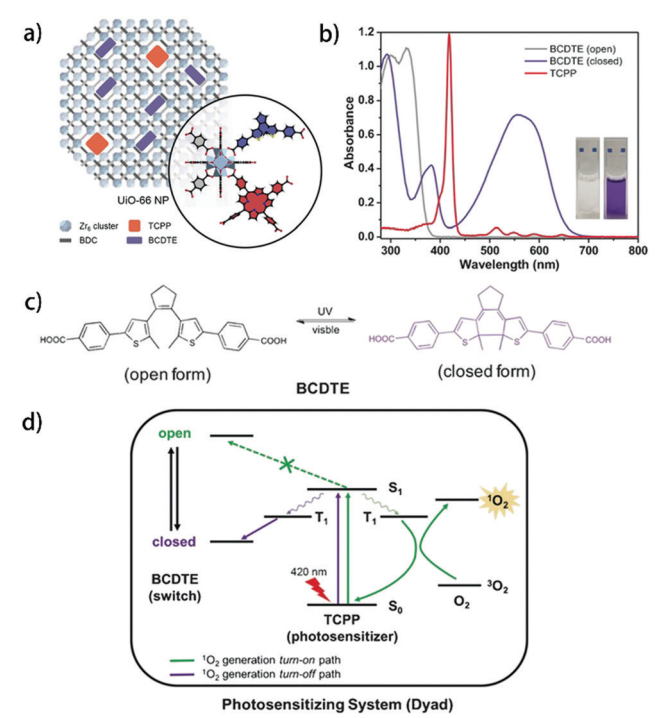


Fig. 7 (a) Defective structure of UiO-66 with inserted TCPP and BCDTE, and a proposed binding scheme of TCPP and BCDTE to a Zr<sub>6</sub> cluster. (b) UV/vis absorption spectra of BCDTE (30  $\mu$ M) and TCPP (2  $\mu$ M). Inset: Photographs of solutions of BCDTE open (left) and closed (right) isomers. (c) Chemical structures and photoisomerization of BCDTE. (d) Proposed scheme of <sup>1</sup>O<sub>2</sub> control via competitive energy-transfer pathways upon photoisomerization. Reprinted with permission from ref. 151. Copyright 2016 Wiley.

quenching <sup>1</sup>O<sub>2</sub> generation (Fig. 7d). More importantly, the ratio of BCDTE to TCPP can be tuned. When the ratio of BCDTE to TCPP was the highest, the quenching ability was the best as well. This strategy was proved to be effective in the cell model, which could serve as a protective system in PS delivery.

#### 3.2 Modifications via photodynamic agents

Fabricating composites using PSs and non-intrinsic photodynamic MOF is another way to make MOF-based PDT agents. The reported structures include PSs encapsulation, surface attachment and core-shell structure. In this strategy, PSs are not limited to porphyrin and its derivatives. The choices of MOF are also more varied, such as ZIF-8, UiO-66 and MIL-101, etc. (ZIF, UiO, MIL refer to the zeolitic imidazolate framework, Universitetet i Oslo, Materials Institute Lavoisier, respectively), which are frequently used in biomedical applications. Recent advances are summarized in Table 3, and the chemical structures of typical organic linkers and encapsulated PSs are summarized in Fig. 8. 148,151–153,155,157,158,160,161,164,179

3.2.1 PS encapsulation. PS encapsulation is the most widely used strategy to cause non-intrinsic MOF photodynamic activity. MOF here serves as the carrier of PSs, creating a "ship in a bottle" structure. The loaded PSs should have certain functional groups, such as -COOH and -SO<sub>3</sub>H, or have the opposite charge to the MOF. 66,188 The loading can be achieved

through two strategies: loading during MOF synthesis and postsynthetic loading. 109 The advantages of PS encapsulation include the following: (i) preventing PS aggregation; (ii) blocking the contact of PSs and O<sub>2</sub>, thus the ROS generation of PSs can be inhibited before reaching the tumor area; (iii) preventing preleakage of PSs during transportation; (iv) improving the tumor specificity of PSs, etc. 50,157,168 In 2015, Zhang et al. encapsulated tetrakis(1-methylpyridinium-4-yl)porphyrin (TMPyP) in a Znbased MOF as a PS with a loading efficiency of 32.8%. 152 The final product was named PS@MOF. With methylene blue as a standard agent, the  $^{1}O_{2}$  yield of PS@MOF was  $0.61 \pm 0.05$ , which was higher than that of TMPyP (0.10  $\pm$  0.02). The unshifted fluorescence emission spectra and blue-shifted phosphorescence emission spectra of PS@MOF indicated that compared to free TMPyP, PS@MOF showed the same energy gap between the higher-energy singlet excited state (S<sub>1</sub>) and the ground state  $(S_0)$ , and widened the energy gap between the triplet state  $(T_1)$ and the S<sub>0</sub> energy level. Hence, the energy gap between S<sub>1</sub> and T<sub>1</sub> was narrowed, which resulted in enhanced intersystem crossing. The phosphorescence quantum yield of encapsulated TMPyP was  $\sim 34\%$ , which means that most of the triplet state PS was used for reacting with <sup>3</sup>O<sub>2</sub>, leading to more <sup>1</sup>O<sub>2</sub> generation. Furthermore, compared to free TMPyP, the PS@MOF composite showed much less cytotoxicity.

More and more PSs have been reported to be encapsulated in MOFs for PDT, such as chlorine e6 (Ce6), zinc phthalocyanines (ZnPc), methylene blue and rose bengal, as shown in Table 3. Taking Ce6 as an example, which is an efficient PS but suffers from aggregation-caused quenching,50 Wang and coworkers fabricated MOF-199 (composed of Cu nodes and 1,3,5benzenetricarboxylic acid (H3BTC) ligands) and loaded Ce6 in the MOF with a loading efficiency of 49 wt%. 168 The Ce6 was in an inert state in MOF-199. After the internalization of cells, Cu(II) nodes of MOF-199 reacted with GSH, leading to the collapse of the MOF structure. Hence, the loaded Ce6 was released and contacted the intracellular O2 to generate ROS. This GSH-controlled PS release strategy can minimize ROS loss and scavenge intracellular GSH at the same time. Xie et al. fabricated a O2-Cu/ZIF-8@Ce6/ZIF-8@F127 hybrid MOF (Fig. 9a),<sup>171</sup> in which the Cu<sup>2+</sup>-doped ZIF-8 was encapsulated by Ce6/ZIF-8@F127. The former was used as an O2 carrier and GSH scavenger, while the latter was employed for PDT. As a typical pH-responsive MOF, ZIF-8 will collapse in the mild acid environment of the tumor area, releasing O2, Ce6 and Cu2+. Due to a sufficient O2 supply, the PDT efficacy of Ce6 was enhanced. Moreover, Cu2+ could go through a Fenton-like reaction, thus reducing GSH content and the product Cu1+ can further generate cytotoxic OH for better PDT efficacy. Wang et al. encapsulated Ce6-functionalized DNAzyme into ZIF-8 to realize imaging-guided gene-photodynamic synergistic therapy (Fig. 9b).<sup>51</sup> ZIF-8 can improve the cellular uptake of DNA through enhanced permeability and the retention effect. In the tumor area, ZIF-8 would degrade and release Zn<sup>2+</sup>, which served as the DNAzyme cofactor to trigger the RNA-hydrolytic ability of DNAzyme. The mRNA, human early growth response-1, acted as the substrate for gene therapy. After the treatment of Chem Soc Rev

 Table 3
 Summary of MOFs modified by PSs in PDT. Particle size was measured by SEM, TEM or DLS

		Organic ligands	Photodynamic agents	PS loading	Materials for decoration	Particle size	Irradiation wavelength	Additional functionality	Ref
_	Zn <sup>2+</sup>	$H_3BTC$	ТМРуР	32.8%	GPTS, Cy3-labelled caspase-3 peptide, $\rm H_2N-PEG-FA$	_	660 nm	Targeting, fluorescence imaging	152
ZIF-8	$Zn^{2+}$	2-mIm	$g$ - $C_3N_4$	_	DOX	60 nm	Visible light	Drug loading, fluorescence imaging	153
	$Zn^{2+}$	2-mIm	AlPcS <sub>4</sub>	10.6%	Catalase, cancer cell membrane	110 nm	660 nm	O <sub>2</sub> supply, targeting	154
1IL- 01(Fe)	Fe <sup>3+</sup>	$H_2BDC$	Ce6-peptide	$32.3 \text{ mg g}^{-1}$	camptothecin, COOH-PEG-FA	95 nm	660 nm	Fluorescence imaging	155
IF-8	$Zn^{2+}$	2-mIm	$g$ - $C_3N_4$	_	NaGdF <sub>4</sub> :Yb, Tm@NaGdF <sub>4</sub> , PEI, carbon dots	∼150 nm	980 nm	Upconversion	156
F-8	$Zn^{2+}$	2-mIm	Methylene blue	1.97%	NaYF <sub>4</sub> :60%,2%Er, catalase	$\sim$ 450 nm for ZIF-8	980 nm	Upconversion, O <sub>2</sub> supply	157
O-66		$\rm H_2BDC$	ZnPc	_	Erlotinib	100 nm for UiO-66	670 nm	Targeting, drug loading	158
IL-88	Fe <sup>3+</sup>	$H_2BDC$	Methylene blue	4.3 wt%	DOX	152 nm	635 nm	Drug loading	159
-	Hf <sup>4+</sup>	BATA	Ce6	80% (w/w)	DOX, PEG	∼90 nm	660 nm	Drug loading, CT imaging	160
F-90	$Zn^{2+}$	IcaH	2I-BodipyPhNO <sub>2</sub>	$25.4\pm1.0$ wt%	_	<80 nm	540 nm	_	161
F-8	$Zn^{2+}$	2-mIm	ZnPc-COOH	$0.296 \mathrm{~g~g^{-1}}$	CTAB	83.5 nm	670 nm	Drug loading	162
F-8	Zn <sup>2+</sup>	2-mIm	ZnPc	5.9 μg mg <sup>-1</sup>	_	255 nm (in	650 nm	_	163
	Fe <sup>3+</sup>	H <sub>3</sub> BTC	Ce6, TPEDC,	49, 42 and	F127	PBS for 72 h) 340 nm	White light	O <sub>2</sub> supply	50
00		-3-10	TPETCF	58 wt%		(average)		- 2 ~ F P*J	- 0
F-8	$Zn^{2+}$	2-mIm	Rose bengal	$35.3~\mu g~mg^{-1}$	$SiO_2$	93.8 ±	532 nm	_	16
	_ 2+		_ , ,		ala /	17.3 nm		_ , , ,,	
·-90	Zn <sup>2+</sup>	IcaH	Rose bengal	5.6%	SiO <sub>2</sub> , NaYF <sub>4</sub> :Yb/ Er@NaYbF <sub>4</sub> :Nd@NaGdF <sub>4</sub> ,DOX,	140 nm	808 nm	Drug loading, upconversion,	16
	1±				PEGFA			MRI, targeting	
<b>D-66</b>	Zr <sup>4+</sup>	$H_2BDC$	Photochlor	0.38%	AQ4N, PEG, <i>p</i> -azidomethylbenzoic acid	95 nm	671 nm	Drug loading, fluorescence	16
7-8	$Zn^{2+}$	2-mIm	Ce6 modified	10 wt%	_	167 nm	660 nm	imaging Gene therapy	51
F-8	$Zn^{2+}$	2-mIm	DNAzyme Ce6	28.3 wt%	Bovine serum albumin-MnO <sub>2</sub>	100 nm for	650 nm	O <sub>2</sub> supply, MRI	16
	$Cu^{2+}$	$H_3BTC$	TPAAQ, Ce6	58 wt% and	NPs F-127	Ce6@ZIF-8 150 nm	White light	GSH depletion	16
9	2.1			49 wt%					
OF-	Cu <sup>2+</sup>	H <sub>3</sub> BTC	PEG conjugated TBD	_	Pt(IV) NPs	160 nm	White light	GSH depletion, drug loading, O <sub>2</sub> supply	16
7-8	$Zn^{2+}$	2-mIm	Ce6	67.4%	PVP, Au NPs	106 ± 7.3 nm	660 nm	O <sub>2</sub> supply O <sub>2</sub> supply	17
-8	Zn <sup>2+</sup> , Cu <sup>2+</sup>	2-mIm 2-mIm	Ce6	3.34 wt%	F127	95 nm	650 nm	Drug loading, oxygen deliv- ery, GSH	17
F-8	$Zn^{2+}$	2-mIm	Ce6	_	Si-Gd NPs, DOX, HOOC- PDMAEMA-SH, PEG-FA	70 nm	630 nm	depletion Drug loading, fluorescence	17
								imaging, MRI	
L- 1	Fe <sup>3+</sup>	$H_2BDC$	Methylene blue	54.5%	DHA, PLA, PEG	120 nm	650 nm	MRI, drug loading, O <sub>2</sub>	17
F-8	$Zn^{2+}$	2-mIm	Methylene blue	5%	Catalase, PDA NPs	_	660 nm	supply PTT, O <sub>2</sub> supply	17
F-8	Zn <sup>2+</sup>	2-mIm	TAPP	_	Catalase, GOx, NaYF <sub>4</sub> :Yb,Tm	_	980 nm	O <sub>2</sub> supply, starvation	17
								therapy	
	$Fe^{3+}$	Tannic acid	Self-assembled Ce6 and	13.89% for Ce6	Catalase	_	_	O <sub>2</sub> supply	17
			rapamycin core						
8-8	$Zn^{2+}$	2-mIm	Ammonium methylbenzene	From 1.5 $\pm$ 0.2 wt% to 99.5 $\pm$ 6.0 wt%	Polyacrylic acid, AgNPs, vancomycin/NH <sub>2</sub> –PEG	150 nm	650 nm	Bacteria killing, biofilm	17
. 0	$Zn^{2+}$	0	blue	76.000/	TTA	150 nm	CC0 n	inhibition	4-
F-8	ZII 7n <sup>2+</sup>	2-mIm	Ce6	76.80%	НА	150 nm	660 nm	—	17
o- OF-1	Zn <sup>2+</sup>	H <sub>2</sub> BPDC	$[Ru(bpy)_3]^{2+},$ $[Ru(phen)_3]^{2+},$	_	_		490 and 800 nm	Two-photon activation PDT	17
0	2.+	II DD= =	$[Ru(phen)_2hipp]^{2+}$	40.05 :0/		0.2	****	m 1 .	
O-67	Zn	$H_2BPDC$	$\left[Ru(bpy)_3\right]^{2^+}$	13.85 wt%	_	∼92 nm	wnite light	Two-photon activation PDT	18

**Review Article** Chem Soc Rev

Table 3 (continued)

MOF		Organic ligands	Photodynamic agents	PS loading	Materials for decoration	Particle size	Irradiation wavelength	Additional functionality	Ref.
ZIF-8	Zn <sup>2+</sup>	2-mIm	Au <sub>25</sub> (Capt) <sup>18-</sup>	_	Fe <sub>3</sub> O <sub>4</sub>	100 nm	808 nm	PTT	181
PB	Fe <sup>3+</sup> , Fe <sup>2+</sup>	-CN <sup>-</sup>	AlPc	_	PDA, bovine serum albumin	~108 nm	660 nm	PTT, MRI, photoacoustic imaging, fluorescence imaging	182
UiO-66	$\mathrm{Zr}^{4^+}$	H <sub>2</sub> BDC	Ce6	5.95%	Pt, Au shell	60 nm without Au shell	808 nm PTT, 670 nm PDT	PTT	183
UiO-66	$\mathrm{Zr}^{4^+}$	$\rm H_2BDC$	ICG	_	Red blood cell membrane	64.7 nm	808 nm	PTT, immune escape	184
MIL-53	Fe <sup>3+</sup>	$H_2BDC$	Cypate	_	PEG, transferrin	250 nm	785 nm	PTT, targeting	185
MIL- 101	Fe <sup>3+</sup>	H <sub>2</sub> BDC	Black phosphorus	15.8 wt%	HOOC-PEG-folic acid	140 nm	808 nm PTT, 660 nm PDT	PTT, targeting, O <sub>2</sub> supply	186
UiO-68	Zr <sup>4+</sup>	TPDC	Protoporphyrin IX	29.1 wt%	_	$\sim$ 120 nm (diameter), $\sim$ 20 nm (thickness)	635 nm	PTT	187

DNAzyme@ZIF-8, the substrate RNA showed down-regulated expression in MCF-7 cells (Fig. 9c). Ce6 provided the MOF

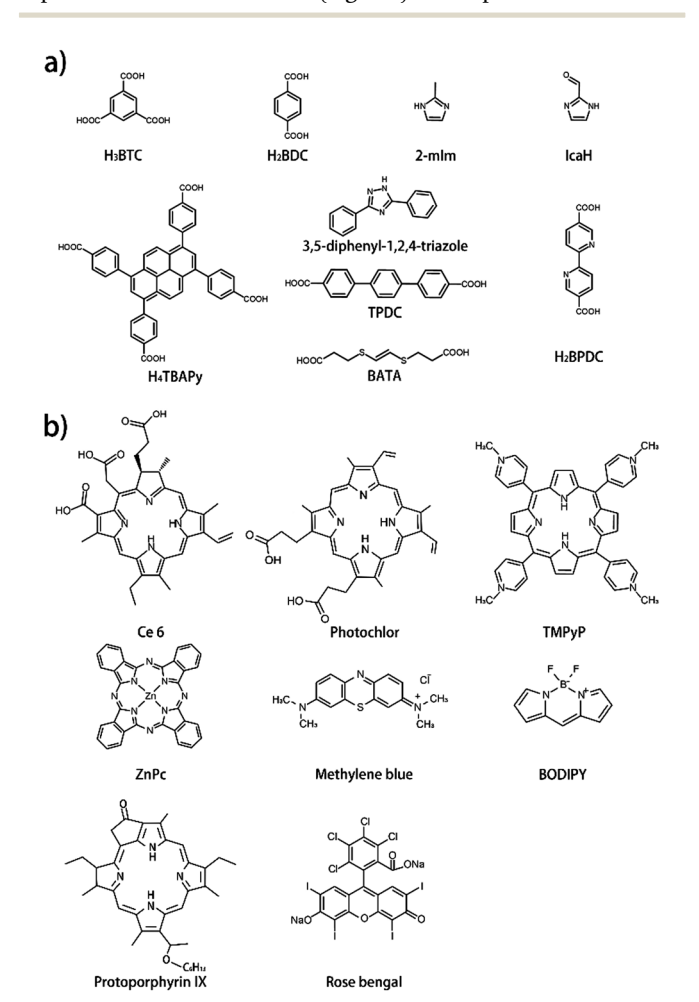


Fig. 8 Chemical structures of (a) MOF ligands and (b) PSs that can be used for MOF modification.

imaging guidance and ROS generation. Under light irradiation, the early apoptotic ratio increased to 44.9%, which was much higher than individual PDT (33.6%) and gene therapy (19.85%).

3.2.2 Surface attachment. Besides encapsulation, PSs can also be attached to the exterior of the MOF. There are two types of surface attachment: covalent and coordinative modification, both of which are post-synthetic modifications. 189-191 In the former strategy, the MOF should be modified with certain functional groups (e.g. -NH2 and -COOH), which can bind the targeted agents on the surface of MOF. 190,192 The attachment of PSs is irreversible, which can prevent the pre-leakage of agents. 109,193 The attached functional agents should maintain their properties while on the MOF, or be released in certain environments due to the cleavage of the linkage with MOF, and then restore their function. 109 The latter strategy refers to binding targeted agents to the unsaturated metal sites or linkers of MOF, such as metal nodes that coordinate with solvent molecules and linkers containing functional groups that do not participate in the MOF formation. 189,190 This strategy is more straightforward than the former and usually does not affect the topology of the MOF. 189 Although these two strategies have been widely applied in MOF modification, the reported surface-attached PSs on the MOF are few. Here are some examples.

Liu and coworkers firstly modified MIL-101(Fe) MOF with -NH<sub>2</sub> (referred to as MOF-NH2). The amino groups were used as an anchor to attach the Ce6-labelled cathepsin B (CaB) substrate peptide. 155 The fluorescence of Ce6 was inhibited because the electron of the excited Ce6 was transferred to MOF-NH2. CaB is a lysosomal cysteine endopeptidase that exhibits higher expression in cancer cells. In this therapeutic system, CaB acted as an intracellular target to trigger PDT. When in contact with CaB, the substrate peptide was cut off, then the photodynamic activity of Ce6 was restored. Moreover, MIL-101(Fe) was loaded with the anticancer drug camptothecin. This drug-release combined PDT

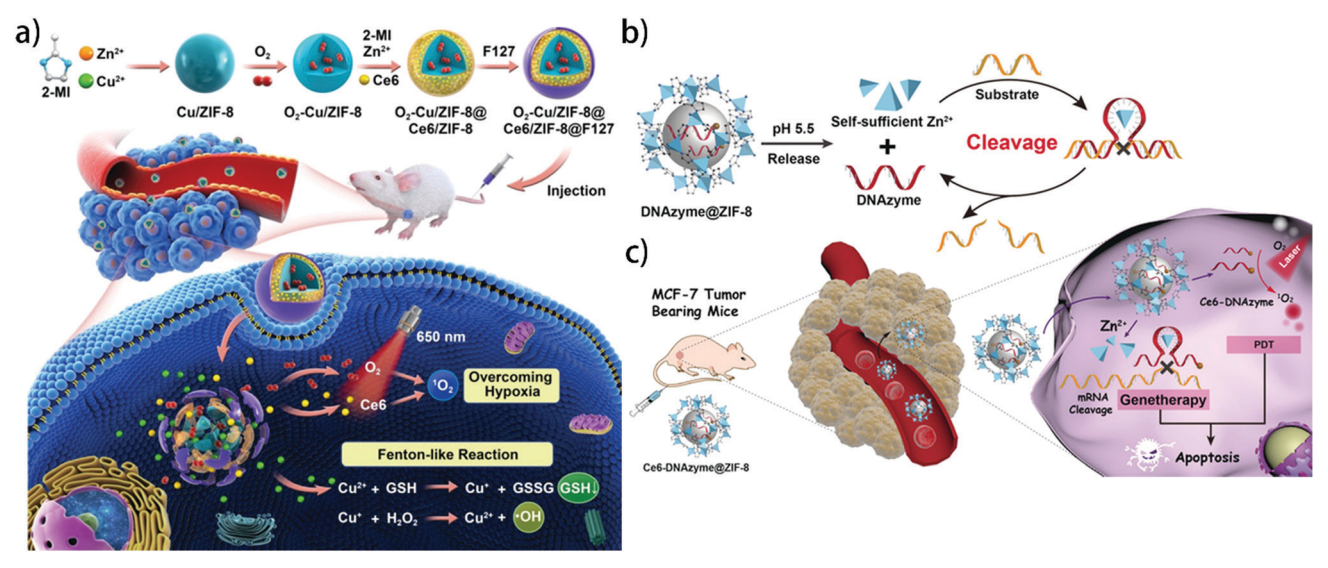


Fig. 9 (a) Schematic illustration of the fabrication process of the tumor microenvironment-responsive  $O_2$ –Cu/ZIF-8@Ce6/ZIF-8@F127 nanoplatform for enhanced PDT and chemotherapy through GSH depletion and  $O_2$  replenishment. Reprinted with permission from ref. 171. Copyright 2019 American Chemical Society. (b) The pH-triggered release of DNAzyme and the corresponding  $Zn^{2+}$ -ion cofactors for efficient gene silencing therapy, and an all-in-one DNAzyme@ZIF-8 nanosystem for fluorescence imaging-guided combined gene/photodynamic therapy. Reprinted with permission from ref. 51. Copyright 2019 Wiley.

can reduce drug resistance and PDT's dependence on  $O_2$ . Nian  $et\ al.$  attached the carboxyl substituted ZnPc and anticancer drug erlotinib on  $N_3$ -UiO-66-NH $_2$  by covalent modification. <sup>158</sup> ZnPc was connected to  $-N_3\ via$  amidation and erlotinib was connected to  $-NH_2\ via$  click chemistry. The final product, E-UiO-66-Pc, had higher ROS generation than ZnPc alone. This strategy provides accessibility for functional group-guided PS and drug surface attachment.

3.2.3 Core-shell structure. The core-shell structure refers to growing the MOF shell on the PS. The core-shell structure can combine the properties of the core and shell material while keeping the stability and activity of the inner PS core by the MOF shell protection.<sup>142</sup> For example, Chen and coworkers synthesized a ZIF-8 shell on the g-C<sub>3</sub>N<sub>4</sub> core, and loaded doxorubicin (DOX) in ZIF-8. 153 Under visible light irradiation, the g-C<sub>3</sub>N<sub>4</sub>@ZIF-8 nanocomposite showed similar <sup>1</sup>O<sub>2</sub> generation to that of g-C<sub>3</sub>N<sub>4</sub>, indicating that the MOF shell did not influence the properties of the g-C<sub>3</sub>N<sub>4</sub> shell, but facilitated the diffusion of <sup>1</sup>O<sub>2</sub> through the porous structure of the MOF. Moreover, the MOF shell was loaded with DOX. The drug release was responsive to an acid environment, which added more potency to the therapy. However, g-C<sub>3</sub>N<sub>4</sub> was excited under visible light, which has limited penetration depth. To solve this problem, Yang et al. decorated g-C<sub>3</sub>N<sub>4</sub> with upconversion nanoparticles and carbon dots (CDs), which were protected by the ZIF-8 shell. 156 Since the absorption of g-C<sub>3</sub>N<sub>4</sub> in the visible light region was stronger than that in NIR light region, when irradiated by a 980 nm laser, upconversion nanoparticles converted NIR light to UV-vis light, thus triggering g-C<sub>3</sub>N<sub>4</sub> to produce ROS. Simultaneously, CDs converted the UV-vis light generated from upconversion nanoparticles into blue visible light, which once again triggered g-C<sub>3</sub>N<sub>4</sub> for a second ROS

generation. Therefore, the ROS generation of the final product was much higher than that of free g-C<sub>3</sub>N<sub>4</sub>. It was noted that this dual-model PDT system was protected by the ZIF-8 shell. As a result, the composite showed little change in particle size, even when immersed in solution for 5 days. Moreover, the outside shell of ZIF-8 also provided space to store  $O_2$  and  $H_2O$  as the raw material for ROS production.

#### 3.3 Optimizing the efficacy of photodynamic therapy

We have discussed how to synthesize a MOF-based PS based on MOF construction and PS agent selection. To successfully apply these PSs in clinical trials with potent therapeutic efficacy, the therapeutic system is not limited to ROS generation. On the other hand, is hard to cure advanced cancer with PDT alone without recurrence. Hence, more elaborate designs of MOF-based PSs and more complex combined systems have been developed by researchers, which will be discussed in this section.

### 3.3.1 Utilizing the properties of the therapeutic environment.

PDT is usually applied to the tumor or bacterial infected area. Hypoxia is one typical feature of the tumor microenvironment and biofilms, 110,195 however, excessive acidity, highly expressed GSH levels and the presence of adenosine-5'-triphosphate (ATP) also exist. 196 It is known that PDT is strongly dependent on oxygen concentration. 2,67 In an oxygen insufficient area, PDT will have much less efficacy. GSH is an important antioxidant in tumor cells, which can protect cells from the attack of free radicals including ROS. Thus, the PDT efficacy will also be affected. 197,198 One straightforward way to solve these problems is by increasing the amount of PS, however, a PS overdose could arouse serious side effects. 128 As such, researchers have made efforts to design

specific structures of MOFs or make targeted modifications to achieve self-oxygen generation and GSH depletion.

**Review Article** 

As mentioned in Sections 3.1 and 3.2, Mn(III)<sup>105</sup> and Cu(II)<sup>128,169</sup> can reduce GSH to oxidized GSH (GSSG); Fe(II),<sup>57</sup>  $Mn(II)_{137}^{137}$  Fe(III)<sup>50,173</sup> and Cu(I)<sup>148,199</sup> can react with both intraand extra-cellular H2O2 through the Fenton or Fenton-like action to produce O2. Taking Fe3+ and Fe2+ as examples, the related Fenton reaction (eqn (7)) and Fenton-like reaction (eqn (8)) processes are presented below:<sup>200</sup>

$$Fe^{2+} + H_2O_2 \rightarrow Fe^{3+} + {}^{\bullet}OH + OH^-$$
 (7)

$$Fe^{3+} + H_2O_2 \rightarrow Fe^{2+} + {}^{\bullet}OH_2 + H^+$$
 (8)

The MOF mentioned above is H2O2 or GSH-responsive, which means that the material will decompose after reaching the therapeutic area. On the other hand, modifications based on these elements and other catalytical agents have also been reported, such as MnO<sub>2</sub> NPs and coating, 121,122,132,201 Pt NPs, 48,63 catalase, 154,157,175 etc., which have similar functions. For instance, Liu and coworkers. Synthesized a MnO2 shell on the Zr-TCPP core by mixing the MOF solution with KMnO<sub>4</sub> solution under vigorous stirring.201 The MnO2 coating quenched the ROS generation and the fluorescence of the inner core due to the fluorescence resonance energy transfer. When in contact with GSH, the MnO<sub>2</sub> shell was reduced to Mn<sup>2+</sup>, resulting in GSH depletion and GSSG generation. Therefore, the properties of Zr-TCPP were recovered. As the consumption of MnO2 shell was fast, it was unable to offer consistent catalyzing ability. In this regard, Yin et al. fabricated a core-shell structure composed of a MnFe<sub>2</sub>O<sub>4</sub> core and Zr-TCPP shell, which was termed as MnFe<sub>2</sub>O<sub>4</sub>@MOF (Fig. 10a).<sup>57</sup> MnFe<sub>2</sub>O<sub>4</sub> features both catalase-like and GSH peroxidase-like activities. Both Fe<sup>2+</sup> and Mn<sup>2+</sup> firstly went through the Fenton reaction to generate Fe<sup>3+</sup> and Mn<sup>4+</sup>, which were further reduced by GSH and H<sub>2</sub>O<sub>2</sub> to produce GSSG and O<sub>2</sub>, creating a reaction cycle. Therefore, the total content of Fe<sup>3+</sup> and Mn<sup>2+</sup> in

MnFe<sub>2</sub>O<sub>4</sub> was not consumed, which leads to its continuous catalytic ability. In hypoxia, the <sup>1</sup>O<sub>2</sub> generation of MnFe<sub>2</sub>O<sub>4</sub>@MOF was improved due to the O2 supply. In the presence of GSH, after 3 min of irradiation, only 17.6% of <sup>1</sup>O<sub>2</sub> generated by MnFe<sub>2</sub>O<sub>4</sub>@MOF was depleted by GSH, while the <sup>1</sup>O<sub>2</sub> depletion percentage for bare Zr-TCPP was 57.4%. The MnFe<sub>2</sub>O<sub>4</sub> core can also be used for MRI. Recently, Wang and coworkers annealed Mn<sub>3</sub>[Co(CN)<sub>6</sub>]<sub>2</sub> MOF to fabricate the mesoporous Mn<sub>1.8</sub>Co<sub>1.2</sub>O<sub>4</sub> nanoenzyme, which was loaded with Ce6 as PS.202 The nanoenzyme was coated with polydopamine (PDA) and polyethylene glycol (PEG) for better biocompatibility. The final product was named MCOPP-Ce6. The Mn atoms in the nanoenzyme served as active sites that can be used to coordinate with Ce6 molecules and decompose H<sub>2</sub>O<sub>2</sub> by the Fenton reaction without self-consumption. Because of the highly porous structure of the MOF-derived nanoenzyme, the H<sub>2</sub>O<sub>2</sub> decomposition rate of the composite was 0.0438 min<sup>-1</sup>, which was much higher as compared to MnO<sub>2</sub>  $(0.0233 \text{ min}^{-1})$ . The porosity of the nanoenzyme also assisted the O2 diffusion to contact Ce6. Hence, MCOPP-Ce6 showed around 95.2% tumor cell killing in an O<sub>2</sub> insufficient environment.

Besides the above-mentioned strategies, Meng et al. found that the disulfide-containing ligand of MOF can also deplete GSH through the disulfide-thiol exchange reaction.<sup>203</sup> In their work, the MOF (referred to as Ce6@RMOF) was composed of a disulfide-bearing imidazole ligand and Zn node. Ce6 was loaded in the MOF with a loading efficiency of 14.9  $\pm$  2.7%, which acted as the PS. Compared to the disulfide-free MOF, Ce6@RMOF showed obvious GSH depleting ability. The ligand was also responsive to low pH and <sup>1</sup>O<sub>2</sub> due to ligand ionization. Therefore, Ce6 can be released in the presence of GSH, tumor acidity or under light irradiation. More importantly, the authors mentioned that glutathione peroxidase 4 can repair lipid peroxidation, which requires the participation of GSH. The GSH depletion (both by reacting with ROS and ligand) can inhibit this process, thus leading to cell death.

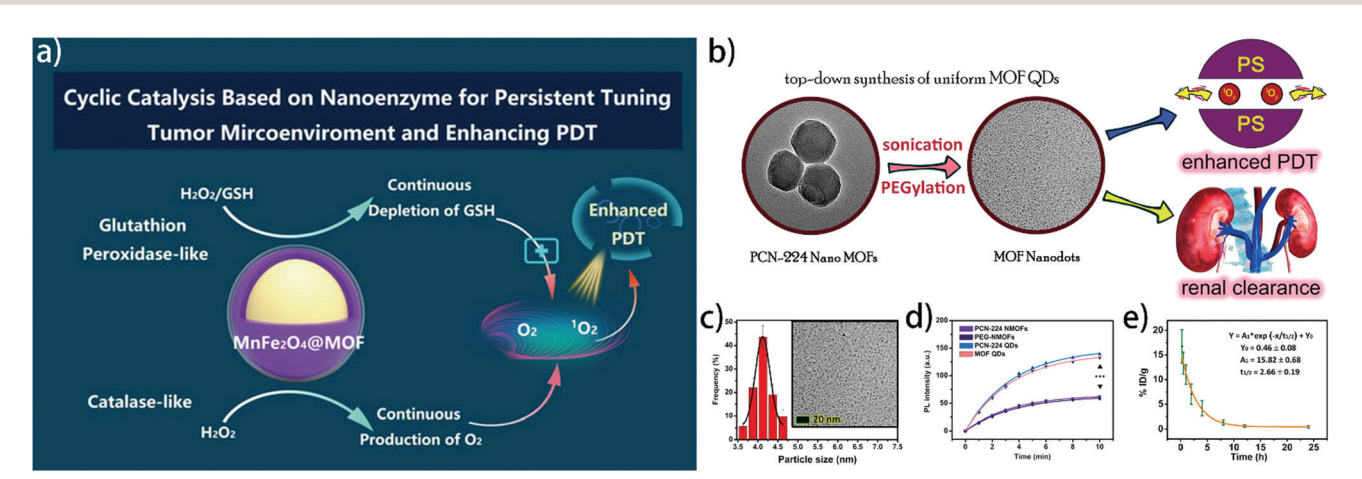


Fig. 10 (a) Schematic illustration of MnFe<sub>2</sub>O<sub>4</sub>@MOF for persistently providing O<sub>2</sub> and consuming GSH to efficiently enhance PDT. Reprinted with permission from ref. 57. Copyright 2019 Wiley. (b) Schematic illustration of the rational design of MOF QDs and their usage as renal-clearable nanoagents for enhanced PDT of cancer. (c) Size distribution and TEM image of MOF QDs. (d) Light-induced ROS generation from PCN-224 NMOFs, PEG-NMOFs, PCN-224 QDs and MOF QDs. (e) Pharmacokinetics of MOF QDs from tumor-bearing mice after intravenous injection. Reprinted with permission from ref. 116. Copyright 2019 American Chemical Society

This phenomenon is called ferroptosis, which is a newly-found contributor to PDT efficacy. Moreover, ferroptosis can be tuned by ligand content. Hence, their work inspired future researchers to consider the coexisting mechanism of PDT and find out more about the relation between PDT and the immune system.

3.3.2 Changing particle size. Particle size is another important factor that deals with ROS generation, cellular uptake, clearance from the body, and biofilm penetration. In general, due to the abnormal tumor vascularization, therapeutic NPs with a size of 5-200 nm can preferentially enter tumor tissue and be retained in it because of poor lymphatic clearance. 204-206 This is called enhanced permeability and retention effect, which endows nano-sized therapeutic agents with a much higher drug delivery efficiency by passive targeting.<sup>207</sup> When the particle size is smaller than 5 nm, the enhanced permeability and retention effect become negligible. This kind of smaller-sized particles can be cleared by the kidneys, which means they have fewer side effects, but their targeting ability is also poorer. 206,208 On the other hand, lager-sized NPs (>300 nm) will be recognized as "foreign substances" by the reticuloendothelial system organs such as the liver and spleen, and are retained in the body for a long time, thus increasing the risk of side effects. 116,205 Hence, exploring the influence of particle size is necessary to simultaneously achieve higher therapeutic efficacy and fewer potential side effects.

Park et al. modulated the size of PCN-224 by analyzing the equilibrium of MOF formation.<sup>58</sup> Using benzoic acid as a competing agent that can form coordination bonds with the Zr<sub>6</sub> cluster, the size of PCN-224 increased with higher concentrations of benzoic acid. They also suggested that other factors included in the formation equation of PCN-224 such as TCPP concentration can also influence the diameter of the product. Their research shed light on controlling the particle size of MOF, which is beneficial for investigating the influence of particle size on PDT efficacy and cellular response. More recently, Wang and coworkers fabricated PCN-224 nanodots by sonication (PCN-224 QDs), which were further PEGylated and referred to as MOF QDs (Fig. 10b). 116 The sonication process could attack the defect sites of PCN-224, thus resulting in smaller fragments with new defect sites, which were further attacked by ultrasound. The final MOF QDs had an average hydrodynamic diameter of 4.5 nm (Fig. 10c), which was smaller than the renal filtration threshold. Moreover, the PCN-224 QDs presented 2-fold ROS yield as compared to the nanosized PCN-224 (Fig. 10d), due to the better utilization of <sup>1</sup>O<sub>2</sub> from the interior PCN-224 nanodots. Animal tests manifested that the MOF QDs could be excreted from the mouse bodies mostly through renal clearance within 1 week, with a blood circulation half-life of 2.66  $\pm$  0.19 h and high tumor accumulation (Fig. 10e). This strategy offered insight into the fabrication of ultrasmall MOF with high therapeutic efficacy and biosafety.

3.3.3 Combined therapy. Since it is hard to cure advanced cancers without recurrence with PDT alone, PDT can be combined with various therapies such as chemotherapy, gas therapy, starvation therapy and immunotherapy. Due to the synergistic effect between PDT and these therapies, the combined therapy usually shows a "1 + 1 > 2" effect. In this regard, MOFs can act as an

Fig. 11 Chemical structures of typical drugs and other modifying agents for MOF modification

ideal platform for combined therapy through modification methods such as encapsulation, surface attachment, and coreshell structure, etc. Hence, in this part, we mainly focus on the therapeutic systems composed of MOF-based PDT and other therapies. The chemical structures of typical drugs and other modifying agents are presented in Fig. 11.61,111,112,115,142,266

Chemotherapy functions by using anticancer drugs to stop or slow the growth of tumor cells.209 In MOF-based PDT therapeutic systems, drugs are usually loaded in photodynamic MOF. The loaded drugs are not limited to traditional anticancer drugs such as DOX and camptothecin (Fig. 11). Li et al. loaded hypoxia-activated tirapazamine (TPZ) in PCN-224, and coated PCN-224 with the cancer cell membrane. 111 Unlike the design of hypoxia alleviation mentioned above, this strategy further decreased the intracellular O2 content by PDT under irradiation. This resulted in extremely low-oxygen environmentactivated TPZ, which released transient oxidizing radicals to kill cancer cells. Therefore, TPZ@PCN@Mem showed better cancer cell inhibition in hypoxia, and the cancer cell viability decreased with increasing the content of TPZ. Min and coworkers incorporated apatinib in PCN-224, and coated it with MnO2 and cancer cell membrane. 60 Angiogenesis in the tumor area will lead to tumor regrowth and metastasis. Apatinib is a vascular endothelial growth factor inhibitor that can effectively inhibit angiogenesis. Apatinib was released in the presence of GSH due to the decomposition of MnO2. Their results showed that apatinib had little influence at the early-stage of treatment but several days later, the groups that were not treated with apatinib resumed the tumor growth, indicating that apatinib-assisted PDT had long-term tumor inhibition. Cheng et al. reported a cancer cell membrane-coated PCN-222 as the carrier of alkaloid piperlongumine (PL) (Fig. 12a).61 The thioredoxin/thioredoxin reductase (Trx/TrxR) system is another way that cancer cells develop to confront oxidative stress, which maintains the cellular redox homeostasis but also leads to the ROS resistance of cancer cells. The dithiol group in Trx can react with ROS through the thiol-disulfide exchange reaction, and the reduced Trx can take

electrons from NADPH catalyzed by TrxR. 210 In this regard, PL can inhibit the activity of TrxR, thus breaking the redox homeostasis in tumor cells. Hence, the ROS level in cells was promoted by 1.6 times after the treatment with PCN-PL@CM, which proved that the effect of ROS was guaranteed, and tumor cells also

**Review Article** 

became more sensitive to ROS.

Starvation therapy refers to cutting off the nutrition supply of cells by glucose decomposition, <sup>25,211</sup> which is usually achieved by glucose oxidase (GOx) or enzyme-like agents according to the following equation:25,62

Glucose + 
$$O_2$$
 +  $H_2O \rightarrow$  Gluconic acid +  $H_2O_2$  (9)

Similar to PDT, starvation therapy also requires an O<sub>2</sub> supply. Therefore, Li et al. fabricated a cascade bioreactor mCGP by encapsulating glucose oxidase (GOx) and catalase in PCN-224.<sup>62</sup> PCN-224 was further camouflaged with the cancer cell membrane. Endogenous  $H_2O_2$  was consumed by catalase to generate  $O_2$ , which was important for ROS production and glucose consumption. Simultaneously, glucose was decomposed by GOx, breaking the glucose metabolism balance of tumor cells. The H<sub>2</sub>O<sub>2</sub>

produced by glucose decomposition could further react with catalase for O2 production. Therefore, this strategy presented enhanced PDT efficacy and tumor proliferation inhibition. Another nano-

reactor was made by Liu et al. 63 They made a sandwich structure where the Pt NPs was embedded between the outer PCN shell and the inner PCN core. The outer PCN was further incorporated with Au NPs (Fig. 12b). Afterwards, folic acid was incorporated for active targeting. The Pt NPs and Au NPs showed catalase-like and glucose oxidase-like activity, respectively. The tumor inhibition of the final product was 90.88%, much higher than that of folic acid attached PCN-224 (41.93%), due to the combined photodynamic and starvation therapy.

Gas therapy is an emerging therapy that uses gaseous transmitters to kill cancer cells with negligible negative effect.<sup>212</sup> Gas molecules are cytotoxic under appropriate concentrations without harming normal cells. 213 Taking NO as an example, NO not only participates in many physiological processes, but also shows a dose-dependent anti-tumor effect. When the concentration of NO is higher than 1 µM, it can directly kill cancer cells

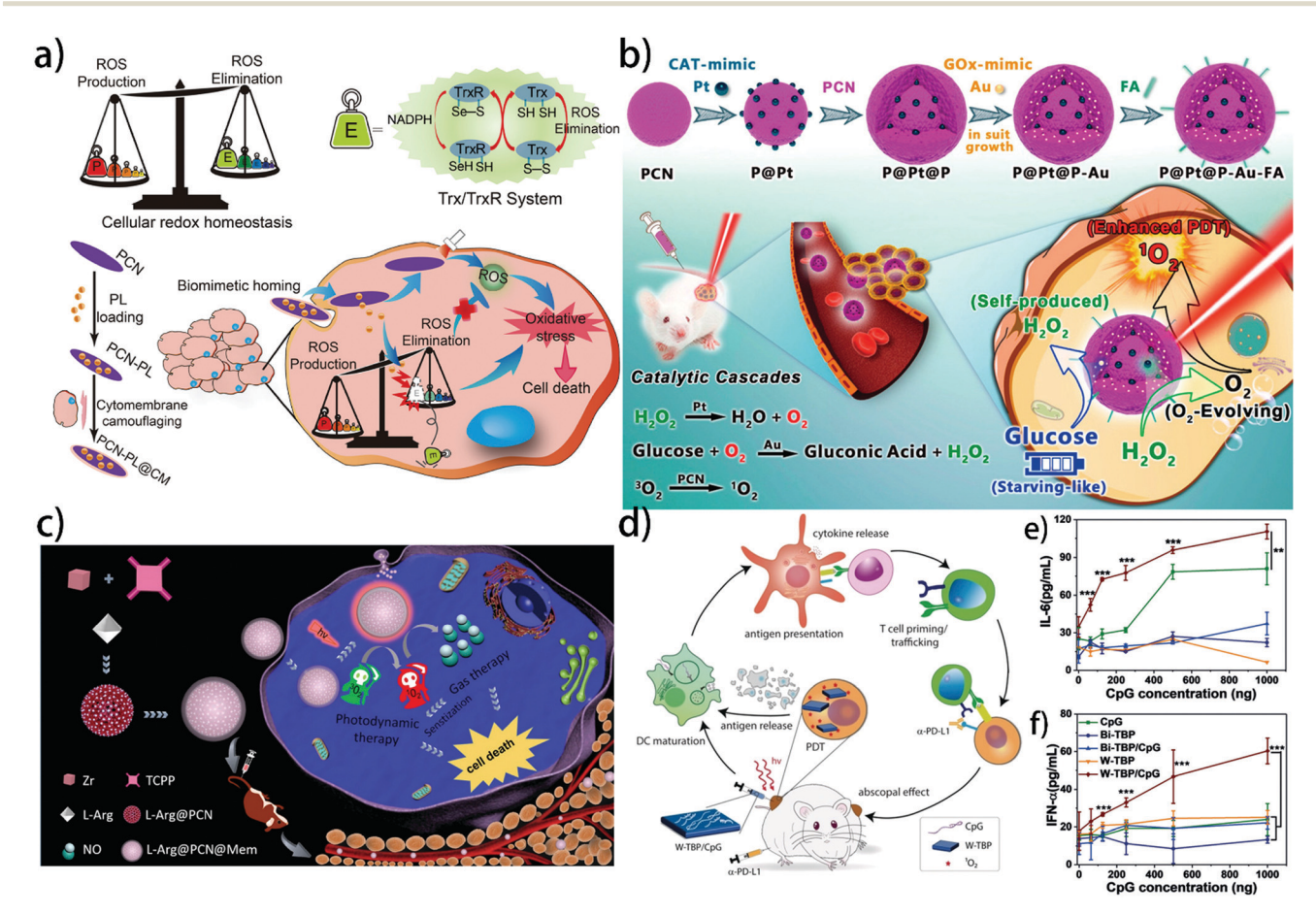


Fig. 12 (a) Schematic illustration of interfering with redox homeostasis in cancer cells for improved PDT. Reprinted with permission from ref. 61. Copyright 2019 Elsevier. (b) Schematic illustration of the catalytic cascades-enhanced synergistic cancer therapy driven by dual-inorganic nanozymesengineered PCNs. Reprinted with permission from ref. 63. Copyright 2019 American Chemical Society. (c) Schematic illustration of L-Arg@PCN@Mem preparation and lethal mechanism of gas therapy and sensitized PDT against tumors. Reprinted with permission from ref. 112. Copyright 2018 Elsevier. (d) W-TBP/CpG promoted antigen presentation via immunogenic PDT and CpG delivery synergizes with checkpoint blockade immunotherapy to afford systemic antitumor immunity. Concentration-dependent IFN- $\alpha$  (e) and IL-6 (b) levels by ELISA, n = 3. Reprinted with permission from ref. 139. Copyright 2020 Wiley.

by mitochondria and DNA nitrosation. 212 Moreover, NO molecules can react with  ${}^{\bullet}O_2^-$  to produce cytotoxic peroxynitrite (ONOO<sup>-</sup>), which has efficient oxidizing and nitrating ability. 214 Generally, gas therapy requires the loading of gas donors or the attachment of gas molecules, and the release of gas is stimuli-triggered. Light irradiation is a suitable stimulus due to minimal side effects, and it also provides the possibility for combining gas therapy and PDT to enhance the therapeutic potency. As an ideal gas carrier, MOF is also appropriate for loading the gas donor and storing the generated gas. Wan and coworkers encapsulated biocompatible L-arginine (L-Arg) in PCN-224 as the NO donor for combined gas therapy (Fig. 12c). 112 Upon irradiation, the donor L-Arg can react with H<sub>2</sub>O<sub>2</sub> and ROS to generate NO with a long half-life and wide diffusion range. More importantly, in a hypoxic environment, due to the free diffusion and penetration of NO, NO can sensitize tumor cells to ROS. Although NO generation consumed part of the ROS, their results showed that the combination of the released NO and PDT achieved much better therapeutic efficacy than PDT alone, almost completely eliminating the tumor. Guan et al. firstly synthesized the UiO-66-OH(Hf) MOF composed of Hf nodes and H2BDC ligand.64 Afterwards, 2I-BODIPY, which acted as a PS, was attached to UiO-66-OH(Hf) by etherification, and the gas donor, MnCO, was further coordinated to Hf cluster nodes. In the presence of oxidizing agents such as H<sub>2</sub>O<sub>2</sub> and <sup>1</sup>O<sub>2</sub>, the Mn(I) in MnCO can be oxidized to Mn(II), thus releasing CO molecules. Hence, light irradiation not only triggered the PDT effect but also CO release through <sup>1</sup>O<sub>2</sub> generation. CO can hinder the ATP generation in tumor cells by activating the oxidative phosphorylation process, thus preventing tumor cell proliferation and tumor metastasis. The selectivity of the MOF and lightcontrolled release of CO also prevented the side effects of CO.

Besides directly releasing cytotoxic agents to kill cancer cells as mentioned above, the response of the immune system is worth considering. In this regard, immunotherapy was put forward, which harnesses immune cells in the tumor microenvironment or host lymphoid tissues to target and eradicate tumor cells, thus preventing tumor metastasis and facilitating systemic immune surveillance. 215,216 Generally, during PDT, the death of tumor cells will result in the release of tumor-assisted antigens, which are then presented to T cells by antigenpresenting cells (especially dendritic cells). 139,216,217 However, the tumor can release immunosuppressive signals through the expression of proteins or interfering with the receptors on T cells, thus leading to T cell apoptosis and preventing the response of the immune system. 107,216,218 On the other hand, tumor-assisted antigens are deficient in the tumor microenvironment, and the antigen-presenting efficiency of dendritic cells is also poor, which all hinder the immune response. 123,139,219 Hence, several strategies have been put forward, such as blocking the inhibitory signals of T cells or improving the efficiency of antigen presentation.216 The former is referred to as checkpoint blockade immunotherapy. These strategies usually utilize immunostimulatory agents, such as antibodies and small molecules, which can be loaded in the MOF, thus preventing their degradation and improving their targeting ability. 215,216,220

For checkpoint blockade immunotherapy, the commonly used checkpoints are T-lymphocyte-associated protein 4 (CTLA4), programmed cell death 1 (PD-1), programmed cell death 1 ligand (PD-L1), and indoleamine 2,3-dioxygenase (IDO), etc. 215,221 Lu et al. loaded IDO inhibitor in a TBC-Hf MOF with a content of 4.7 wt%. 97 IDO is highly expressed in the tumor microenvironment, which can inhibit the clonal expansion of T cells, thus promoting the immune escape of tumors. The IDO inhibitor in MOF can effectively block the activity of IDO, and the combination of the TBC-Hf and the IDO inhibitor under light irradiation showed the best tumor suppression. Notably, when TBC-Hf and the IDO inhibitor were applied without light irradiation, the tumor growth was slightly inhibited, indicating that the PDTinduced tumor cell death and the following release of tumorassociated antigens are necessary for immunotherapy. Moreover, in this combined therapy, the immune cells can migrate to other tumor areas, causing a strong abscopal effect. Hence, the tumor at the untreated site can also be attacked by immune cells.

As for improving the efficiency of antigen presentation, Ni et al. fabricated a cationic W-TBP MOF (TBP refers to 5,10,15,20tetra(p-benzoato)porphyrin), which can adsorb anionic cytosinephosphate-guanine (CpG) (Fig. 12d). 139 CpG is a toll-like receptor agonist. When internalized by dendritic cells, CpG can bind to toll-like receptor-9, thus promoting the maturation of dendritic cells. The dendritic cells then release cytokine (e.g., immunostimulatory cytokines type I Interferon (IFN-α) and interleukin-6 (IL-6)) as the marker of maturation. Hence, the activated dendritic cells will present more tumor-associated antigens to T cells, which then prime and traffic to activate other T cells. In their work, W-TBP absorbed CpG with an efficiency of 89.9%, which is attributed to the high positive zeta-potential of W-TBP (37.2  $\pm$  0.6 mV). The MOF carrier endowed CpG with higher internalization by dendritic cells, as evidenced by the highest dendritic maturation in Fig. 12e (IFN- $\alpha$ ) and Fig. 12f (tested by IL-6). The combination of PDT and CpGinduced immunotherapy showed 96.6% of tumor regression, much higher than free CpG and PDT alone. Afterwards, the authors demonstrated that this immunotherapy can be combined with checkpoint blockade immunotherapy by injecting the mice with the α-PD-L1 antibody. This combination caused a strong and consistent abscopal effect, which can take effect on distant tumors.

3.3.4 Enhancing the penetration depth. Limited penetration depth is one of the biggest shortcomings of phototherapy. Especially for PDT, the frequently used wavelength of light was 650–800 nm, which can only penetrate the tissue for 3–10 mm.<sup>2</sup> Hence, traditional PDT can only treat lesions that are superficial or within 1 cm of depth. 6,222 Two factors cause this problem. One is that the absorption peak of most PSs is located in the visible range, which means that the longer-wavelength but deeper-penetrating light is not suitable for the excitation of these PSs. 222 Another concern is that when the wavelength of light is longer than 800 nm, the light cannot provide enough energy for the excitation of <sup>3</sup>O<sub>2</sub>. <sup>7</sup> In this regard, the use of two-photon activated PSs and upconversion nanoparticles was put forward.

Most PSs are single-photon excitation PS, which means the PS can only absorb one photon under irradiation. By comparison, simultaneously absorbing two photons, namely two-photon

Review Article Chem Soc Rev

activation, features long-wavelength two-photon absorption, which renders deep-tissue treatment and prevents the energy loss of light. 223 One typical example of two-photon-excited PS is the polypyridyl ruthenium complex (RCs). Zhang and coworkers encapsulated cationic RCs ([Ru(bpy)<sub>3</sub>]<sup>2+</sup>, [Ru(phen)<sub>3</sub>]<sup>2+</sup> and [Ru(phen)<sub>2</sub>hipp]<sup>2+</sup>) in anionic bio-MOF-1 by means of ion exchange. 180 The MOF carrier hindered the intramolecular rotation and  $\pi$ - $\pi$  interactions of RCs, which reduced their aggregation. Moreover, bio-MOF-1 also provided an extended  $\pi$ -conjugation system, which improved the light harvesting ability of RCs. The single-photon activation of bio-MOF-1&RCs was measured under 490 nm light irradiation. The singlet oxygen yields of bio-MOF-1&[Ru(bpy)<sub>3</sub>]<sup>2+</sup> under single-photon activation was 0.86, which was higher than that of [Ru(bpy)<sub>3</sub>]<sup>2+</sup> (0.81) due to the reduced aggregation of RCs. In terms of two-photon activation, the maximum two-photon activation wavelength was in the range of 800-820 nm. Under 800 nm light irradiation, owing to the stronger electron delocalization conjugate system of bio-MOF-1&[Ru(phen)<sub>3</sub>]<sup>2+</sup> and bio-MOF-1&[Ru(phen)<sub>2</sub>hipp]<sup>2+</sup>, they had higher <sup>1</sup>O<sub>2</sub> generation than bio-MOF-1&[Ru(bpy)<sub>3</sub>]<sup>2+</sup>. Therefore, the therapeutic wavelength shifted to the longer region, which rendered deeper light penetration.

Another way to improve the penetration depth of PDT is by using upconversion nanoparticles (UCNPs), which can absorb two or more low-energy photons and generate one high-energy photon. 224,225 In this way, NIR light can be converted into visible light, thus activating PSs. The frequently used UCNPs are lanthanide-doped UCNPs<sup>224,226</sup> and quantum dots.<sup>227,228</sup> In MOFbased therapeutic systems, UCNPs can be attached to the surface of MOF, 96 or covered by MOF as the core material of the core-shell structure. 89,165 For example, He et al. firstly fabricated a coreshell-shell UCNP (NaYb<sub>0.92</sub>F<sub>4</sub>:Er<sub>0.08</sub>@NaYF<sub>4</sub>) with a diameter of  $29.8 \pm 2.2$  nm. <sup>89</sup> Under 980 nm laser irradiation, this UCNP can convert the light source into 524, 542 and 660 nm light, with a quantum yield of  $6.55 \pm 0.34\%$ , which is much higher than that of traditional UCNPs. The UCNP was then coated with the PCN-222 MOF shell (composed of Zr nodes and FeTCPP ligands) and further decorated with Au NPs. The absorption of PCN-222 was located at 554 and 646 nm, which matches well with the emission of UCNPs. Au NPs serve as glucose oxidases to trigger glucose starvation therapy and generate a large amount of H<sub>2</sub>O<sub>2</sub>. The chelated Fe atom in the FeTCPP further reacted with H<sub>2</sub>O<sub>2</sub> for O<sub>2</sub> generation. Hence, the Au NPs and PCN-222 together caused a cascade reaction, and the UCNPs also deepened the therapeutic depth of PDT. After 8 days of 980 nm light treatment, the tumor-bearing mice showed complete tumor eradication without recurrence.

3.3.5 Typical modifications towards antibacterial applications. Bacteria-killing is another important application of PDT, and the mechanism is similar to the anticancer mechanism. Under light irradiation, bacteria are killed by ROS due to the damage of the bacterial cell membrane and the DNA inside. However, the strategies in PDT are not completely suitable for antibacterial applications due to the following reasons. Firstly, bacteria can be divided into Gram-positive (e.g., Staphylococcus aureus) and Gram-negative (e.g., Escherichia coli) bacteria. The cytoplasmic membrane of Gram-positive bacteria is covered by porous peptidoglycan and

lipoteichoic acid, which is easy for PSs to cross. Whereas, besides the cytoplasmic membrane, Gram-negative bacteria have another outer membrane that acts as a barrier to prevent the penetration of PSs. 229 Therefore, traditional PDT has limited efficacy against Gram-negative bacteria. In view of this, PS requires modifications that increase the outer membrane permeability. It is known that bacteria usually bear a negative charge, hence, cationic PSs have greater affinity for bacteria. Another concern is the formation of biofilms, which is a consortium of bacteria growing compactly on living tissues or implant materials. 230,231 The extracellular polymeric substances form a dense and protective shelter that hinders the contact of PSs and the inner bacteria. 232 The biofilm area also features acidity (pH  $\sim 5.5$ ) and hypoxia. Therefore, many strategies have been put forward to accommodate MOF-based PSs for antibacterial applications.

Ag ions are an important biocide that can react with biomolecules such as DNA and peptides due to their affinity for thiols, amines and phosphates, thus causing the irreversible aggregation of these biomolecules and finally leading to the inactivation of bacteria.<sup>233</sup> Zhang et al. loaded Ag ions into PCN-224 and sealed it with surface-adaptive HA. 113 The HA shell can be decomposed by hyaluronidase secreted by Gram-positive bacteria. PCN-224-Ag<sup>+</sup> was able to attack bacteria due to charge interaction, leading to bacterial death. Their results showed that the antibacterial abilities of PCN-224 and PCN-224-HA against methicillin-resistant Staphylococcus aureus (MRSA) were similar under light irradiation, suggesting that the HA coating was degraded by MRSA. After the encapsulation of Ag+, PCN-224-Ag-HA exhibited obvious bacterial inhibition, which was more potent than PCN-224-HA and AgNO<sub>3</sub>. The results confirmed that loading Ag<sup>+</sup> in PCN-224 was effective for bacteria-killing by the synergistic action of both Ag<sup>+</sup> and PDT. It also provided insight for loading other kinds of antibacterial agents in MOF-based PSs, such as Cu<sup>2+</sup> and Zn<sup>2+</sup>.<sup>234-237</sup>

Bacterial adhesion is the initial stage of biofilm formation, which is promoted by ATP stimulated cell lysis and extracellular DNA release. At this time point, the bacteria are easily attacked by PS because of the absence of biofilm protection. In view of this, Qiu et al. decorated PCN-224 with CeO<sub>2</sub> NPs of 4 nm in size to form a shell structure on PCN-224 with L-arg as the capping agents to perform ATP deprivation and PDT (Fig. 13). 114 The Ce<sup>3+</sup> and Ce<sup>2+</sup> in CeO<sub>2</sub> can react with ATP through the nitrogen and oxygen on adenine and triphosphate of ATP. Therefore, the biofilm formation was inhibited because of ATP deprivation, and the planktonic bacteria were subsequently killed by PDT. Results showed that after incubation with different contents of MOF@CeO2, the ATP content decreased with the higher concentration of MOF@CeO2, while the ATP content showed no obvious variation with different concentrations of PCN-224. Therefore, the decoration of CeO2 could effectively eliminate ATP, which led to 40% of biofilm inhibition for MOF@CeO2 (50 μg mL<sup>-1</sup>). When light irradiation (638 nm) was introduced, the biofilm inhibition was 90% for MOF@CeO2 at the concentration of 200  $\mu g \text{ mL}^{-1}$ .

Different from the initial stage, once the biofilm forms, the inner bacteria are protected by the biofilm.<sup>238</sup> In this case, the

DME Zr, cluster PCN-224 PCN-224@CeO

Chem Soc Rev

ATP

CeO

Fig. 13 Schematic illustration of the preparation process of CeO<sub>2</sub>decorated PCN-224 and the inhibition of biofilm formation through the synergy of adhesion-related molecule deprivation and cytotoxic ROS generation. Reprinted with permission from ref. 114. Copyright 2019 Wiley.

ATP deprivation

diffusion of PS and ROS should be taken into consideration. Reducing the particle size of therapeutic agents is a feasible way to penetrate the biofilm. Deng and coworkers fabricated a MOF dot composed of Hf nodes and TCPP ligands, which was further covered with human serum albumin and MnO<sub>2</sub>. The final product was named MMNPs. The diameter of MMNPs was about 105 nm. The outer MnO2 would degrade in the mildly acidic environment or in the presence of H<sub>2</sub>O<sub>2</sub>, releasing porphyrinbased MOF and O2 for hypoxia alleviation. The ultrasmall MOF dot was about 5 nm in size and positively charged, which had excellent penetration ability through the biofilm and a high affinity for the negatively charged bacteria. Therefore, the MMNPs showed 99% and 90% of the antibacterial ratio against E. coli and S. aureus, respectively. Compared to the bulk MOF, this MOF dot showed 12 times higher accumulation in the biofilm. Animal testing manifested that the abscesses of S. aureus-infected mice healed with no obvious inflammation in 5 days after MMNPs treatment and visible light irradiation.

## 4. Photothermal therapy

#### 4.1 Intrinsic photothermal MOF

Intrinsic photothermal MOF refers to MOF that can be directly used as PTAs without the need for extra PTA decoration. One of the most important branches of intrinsic photothermal MOF is Prussian blue (PB) and its analogues. Other intrinsic photothermal MOF is based on (i) photothermal building units and (ii) the ligand-to-metal charge transfer mechanism to have photothermal ability. Hence, in this section, we will introduce the composition as well as typical modification methods for intrinsic photothermal MOF.

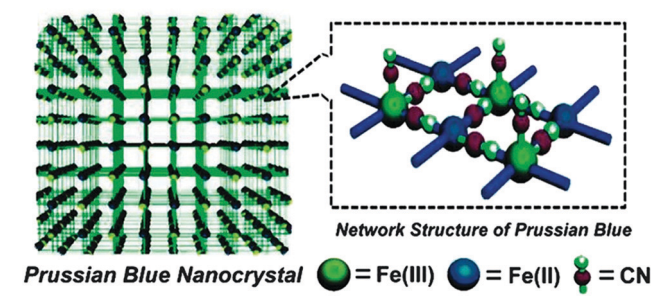


Fig. 14 Basic cubic network structure of PB. Reprinted with permission from ref. 239. Copyright 2015 Royal Society of Chemistry.

4.1.1 Prussian blue-based MOF. PB is one of the oldest synthetic MOFs that has been intensively studied. 239 The chemical structure of PB is presented in Fig. 14. The carbon atom and nitrogen atom of -C≡N- in PB is coordinated with Fe(II) and Fe(III), respectively, creating a face-centered cubic structure. 239,240 The PB has two categories: soluble PB (KFe<sup>III</sup>[Fe<sup>II</sup>(CN)<sub>6</sub>]) and insoluble PB (Fe<sup>III</sup>[Fe<sup>II</sup>(CN)<sub>6</sub>]<sub>3</sub>·nH<sub>2</sub>O).<sup>240</sup> As for insoluble PB, depending on the coordination site of water molecules, it can be divided into coordinative type (water molecules coordinate to iron ions) and zeolitic type (water molecules occupy cavities).<sup>240</sup>

In biomedical applications, PB has been approved by FDA to treat radioactive exposure as clinical medicine with good biocompatibility and biosafety. 100,241 Owing to the charge transfer between Fe(II) and Fe(III), PB can generate heat under NIR irradiation for tumor ablation and bacteria disinfection. 100 The Fe(III) nodes in PB can also react with H<sub>2</sub>O<sub>2</sub> and generate OH through the Fenton reaction. 242 Moreover, the coordination between Fe(III) and water molecules in insoluble PB renders an inner-sphere longitudinal relaxation time with a longitudinal relaxivity of 0.14 mM<sup>-1</sup>, which can be used for MRI-guided therapy.<sup>243</sup>

PB can directly serve as PTA in PTT. Yue et al. fabricated PB by mixing a solution of FeCl<sub>3</sub> and K<sub>4</sub>[Fe(CN)<sub>6</sub>] with citric acid as the surface capping agent. 100 In their work, the size of PB could be controlled by different concentrations of citric acid, ranging from 10 to 50 nm. In addition, their PB had a broad absorption band at 500-900 nm, and the absorption peak was located at 712 nm. Under 808 nm irradiation, the molar extinction coefficient was  $1.09 \times 10^9 \,\mathrm{M}^{-1} \,\mathrm{cm}^{-1}$ , which was slightly lower than that of Au nanorods. The temperature of PB rose to 43  $^{\circ}$ C under less than 3 min of irradiation. After the PTT treatment by PB, the viability of HeLa cells was lower than 10%. However, the absorption peak of PB was near the edge of the near-infrared region (700-900 nm), and the photothermal conversion efficiency was merely 20% under 808 nm irradiation. 54,56 The subsequent research mainly focused on improving the therapeutic efficacy by doping, etching, drug loading and auxiliary methods such as imaging guidance.

Doping is a common modifying method for PB. Up to now, the doped metal ions include Mn<sup>2+</sup>, <sup>244</sup> Zn<sup>2+</sup>, <sup>54,245</sup> Cu<sup>2+</sup> (ref. 246) and Gd<sup>2+</sup>, <sup>247-249</sup> etc., which are usually located at the interstitial site or lattice site (Fig. 15a). 249 The dopant size, distribution and concentration will affect the chemical properties of PB,

rendering PB with tunable photothermal behavior.<sup>54</sup> Besides, imaging guidance can also be introduced through doping. Zhu et al. doped Mn2+ in PB, and coated PB with poly(allylamine hydrochloride) (PAH), polyacrylic acid (PAA) and PEG through the laver-by-laver method. 244 The dopant changed the electron density and orbital energy of PB. Thus, the absorption peak of PB red-shifted to 718, 730, and 768 nm, corresponding to the Mn<sup>2+</sup> doping ratio of 5%, 15% and 25%, respectively. On the other hand, Mn<sup>2+</sup> also increased the longitudinal relaxivity of PB, which showed much-enhanced contrast in MRI. Shou et al. doped 10% Zn2+ in PB (SPBZn(10%)), which resulted in ultrasmall PB particles (3.8  $\pm$  0.90 nm). The SPBZn(10%) showed a 1.3 times higher absorption peak than the non-doped PB. When the doping concentration changed, the photothermal conversion efficiency varied from 37.73% to 47.33%. Besides, the doped Zn<sup>2+</sup> could replace Fe<sup>2+</sup>, giving rise to higher Fe<sup>3+</sup> concentration, and the magnetic saturation value was also

**Review Article** 

The pore size is another important factor that affects the photothermal performance of PB MOF and the drug-loading efficacy. Generally, the pore size of PB is smaller than 1 nm, 250 and the loading capacity is also limited, which is not suitable for drug loading.<sup>251</sup> Therefore, many researchers have reported the hollow mesoporous PB (HMPB) structure by chemical etching or the hydrothermal method. Under light irradiation, the elevated local temperature can accelerate the drug diffusion. For example, Zhou and coworkers used hydrochloric acid to etch PB crystals.25 Nitrogen absorption isotherms manifested that the Brunauer-Emmett-Teller (BET) surface area of PB increased from 302.56 m<sup>2</sup> g<sup>-1</sup> to 922.14 m<sup>2</sup> g<sup>-1</sup> with a pore diameter of 10.12 nm. Cai and coworkers synthesized HMPB by the hydrothermal method and chemical etching. 241 Afterwards,

improved, which was beneficial for the MRI guidance.

the authors added Mn<sup>2+</sup> and [Fe(CN)<sub>6</sub>]<sup>2-</sup> as sources to fabricate a Mn-containing PB analogue shell on both the exterior and interior surfaces of HMPB (Fig. 15b). The final product was termed as HMPB-Mn. DOX was loaded in HMPB-Mn with an efficiency of 97.5%, which was attributed to its coordination with Fe2+ and Mn2+ nodes. In an acidic environment, the Mn-C≡N-Fe structure will decompose, thus releasing Mn<sup>2+</sup> and DOX. The release efficiency of Mn<sup>2+</sup> and DOX at pH 5.0 was 95% and 34.7%, respectively. The pH-induced Mn<sup>2+</sup> release facilitated the MRI ability of HMPB-Mn, which showed the brightest MRI images at pH 5.0 with a molar relaxivity of 7.43 mM<sup>-1</sup> s<sup>-1</sup>. Therefore, this pH-triggered smart therapeutic agent can be used for MRI-monitored drug release, which was synergized with PTT. In another work, Cai et al. loaded DOX and perfluoropentane (PFP) in HMPB.<sup>252</sup> HMPB had a higher intrinsic molar extinction coefficient at 808 nm, which could be used for photoacoustic (PA) imaging. When the temperature increased, the bubbles generated by PFP could act as the contrast agent of ultrasound (US) imaging. The combination of PA and US imaging was beneficial for the early diagnosis of cancer. Therefore, this nanoplatform combined PTT, chemotherapy and diverse imaging on the basis of HMPB, showing almost complete eradiation of tumor.

The Fe<sup>2+</sup>, Fe<sup>3+</sup> and -CN<sup>-</sup> in PB can be active sites for coordination with therapeutic agents. One of the major applications of coordination modification is gas combined therapy. Gas therapy utilizes gas molecules (e.g., CO, 253 NO 212, 254 and H2 104) as cytotoxic agents, which can be attached to a carrier such as MOFs and then released under certain environment conditions. Besides ROS (as mentioned in Section 3.3.3), light-induced temperature increase is also an ideal trigger for gas release. For example, Li et al. coordinated Fe(CO)<sub>5</sub> on mesoporous PB by replacing -CN<sup>-</sup> with

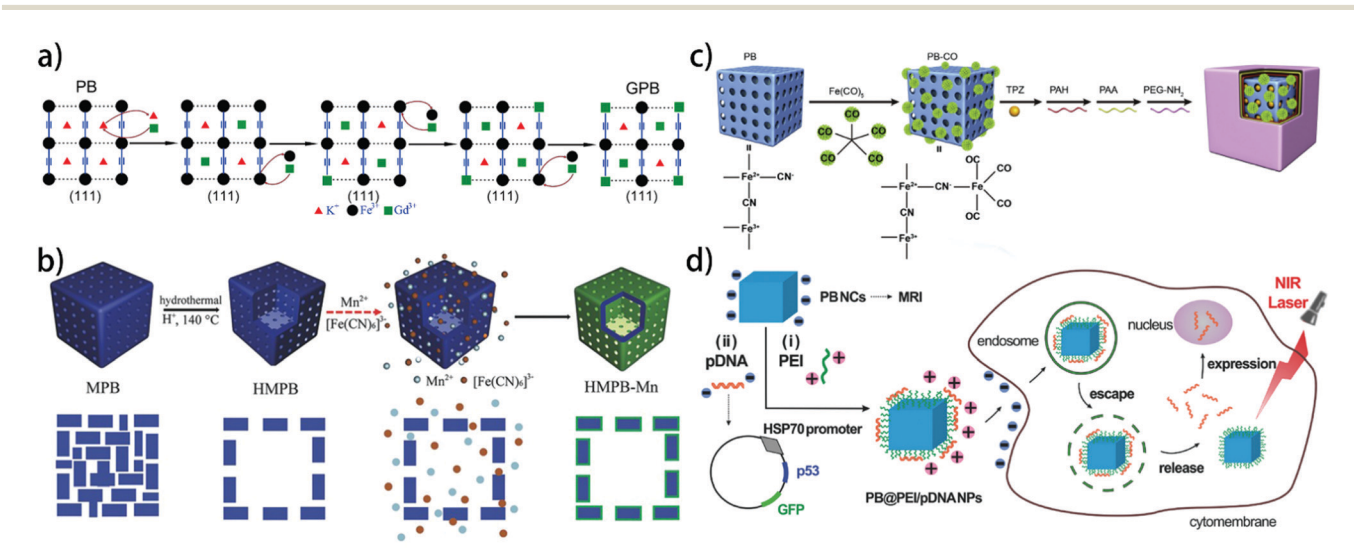


Fig. 15 Different modification methods of PB. (a) Doping: schematic of Gd<sup>3+</sup> simultaneously optimizing the properties of PB nanocrystals. Reprinted with permission from ref. 249. Copyright 2016 American Chemical Society. (b) Hollow mesoporous PB: schematic illustration of the synthetic procedure of HMPB-Mn. Reprinted with permission from ref. 241. Copyright 2015 Wiley. (c) Coordination modification: schematic illustration of PB-CO-TPZ NPs with enhanced bioreductive chemotherapy and CO-mediated pro-apoptotic gas therapy. Reprinted with permission from ref. 255. Copyright 2019 Elsevier. (d) PB-based composites: schematic illustration of HSP70 promoter-based PB theranostic platform for gene therapy/PTT. Reprinted with permission from ref. 257. Copyright 2018 Wiley.

one of the CO moieties of Fe(CO)5.46 CO can lead to cancer cell apoptosis by inducing mitochondria disorder. However, CO can also bind with hemoglobin and oxygen, showing acute toxicity to normal tissues. In order to avoid CO poisoning, the CO release amount was controlled by irradiation time and intensity. The CO release was suppressed in blood circulation. Only under irradiation can the photothermal effect of PB cleave the Fe-CO bond for CO release. Since CO treatment can accelerate mitochondrial respiration in the second stage, which facilitates O2 consumption, Li et al. introduced hypoxia-activated TPZ in Fe(CO)5 and PB therapeutic system, and coated it with PAH, PAA and NH2modified PEG (Fig. 15c).<sup>255</sup> Another coordination method was reported by Feng et al. During the fabrication process of PB, the authors doped PB with sodium nitroprusside (SNP), which is a NO donor. 256 As SNP was embedded in the crystal structure of PB, some of the Fe3+ nodes in PB were coordinated with NO. Afterwards, the PB was loaded with the anticancer drug docetaxel (DTX), generating DTX@m-PB-NO. Upon irradiation, the heat led to the cleavage of Fe-NO bonds, while no NO release was detected at 37 °C, indicating its safety in blood circulation. The highest NO release amount was 10.43 µM. When the NO content reached the micromolar level, it could inhibit tumor growth and metastasis by nitrosation.

Besides the above PB-based PTAs, some other PB-based composites can be derived by coating specific materials on the surface of PB or employing PB as the coating. The former can be categorized into polymer coating (PEI, 257 PEG, 258, 259 chitosan,260 gelatin,261 and PDA,262 etc.), inorganic coating (SiO<sub>2</sub>, <sup>251,263,264</sup> etc.), and MOF coating (ZIF-8, <sup>265</sup> MIL-100(Fe), <sup>169,266</sup> UiO-66, 267 etc.), which is mainly used for stability enhancement, drug loading, and other combined therapy. Wang et al. fabricated the PB@MIL-100(Fe) dual-MOF structure. 266 The outer MOF shell was used as a carrier of anticancer drug artemisinin (ART) with a loading efficiency of 848.4 mg g<sup>-1</sup>. ART was released under an acidic environment because of MIL-100 shell decomposition. Moreover, as the MIL-100 shell increased the dielectric constant of the composite NPs, the absorption peak of PB red-shifted 35 nm. Hence, the temperature of PB@MIL-100(Fe) increased 30 °C at a concentration of 0.2 mg  $\mathrm{mL}^{-1}$  with excellent photostability. Liu et al. coated PB with PEI, which was loaded with pDNA by electrostatic interactions (Fig. 15d).<sup>257</sup> The pDNA was HSP70p53-GFP, wherein HSP70 has higher expression in the moderate temperature region (39-43 °C) and acted as a promoter to activate gene therapy, while p53 and GFP was the targeted tumorsuppressive gene and reporter, respectively. After the endocytosis of PB@PEI/pDNA NPs, the low heat (≤43 °C) can facilitate the endosomal escape of material by destroying the endosomal membrane, thus releasing the pDNA, which was then expressed to the nucleus. When the temperature was about 41  $^{\circ}\text{C}$ , HSP70 initiated the expression of p53, which resulted in tumor apoptosis. When the temperature exceeded 50 °C, the hyperthermia led to cell necrosis. Therefore, the gene therapy and PTT showed a synergistic effect, which was controlled by PB-induced heat generation.

In the latter case, the most reported strategies were to coat PB on contrast agents such as Au, 268,269 Fe<sub>3</sub>O<sub>4</sub>, 270 and MnO<sub>2</sub>, 271 etc., to enhance the imaging properties (MRI, PA imaging, and

Fig. 16 Typical photothermal ligands for intrinsic photothermal MOF

computed topography (CT), etc.) of PB. The core material also provides synergistic functions. Peng et al. coated PB on MnO<sub>2</sub> and encapsulated the NP with red cell membrane (RCM).272 DOX was loaded within RCM by coextruding. The MnO2 core decomposed H<sub>2</sub>O<sub>2</sub> at the tumor site with O<sub>2</sub> generation, which resulted in RCM disruption and DOX release. Moreover, the RCM prolonged the circulation time of NPs and increased the aggregation of NPs at the tumor site, which resulted in a higher PTT temperature (59.6 °C) as compared to the non-coated samples (49.3 °C). This group also demonstrated that the PB/MnO<sub>2</sub> nanocomposite has a high diamagnetic transverse relaxation time  $(T_2)$  signal intensity, which was promising in MRI and PAI.<sup>271</sup>

4.1.2 Utilizing photothermal agents as building units. MOFs with intrinsic photothermal effect can be synthesized by employing various kinds of PTAs as ligands, as schematically shown in Fig. 16. 49,93,103

For instance, Yang et al. synthesized a MOF using Mn as nodes and IR825 as ligands, and they covered this MOF with PDA and PEG for better biocompatibility. 93 On the one hand, as a common NIR dye with NIR light absorption peak at 825 nm, IR825 endowed the composite with photothermal performance. Under 808 nm light irradiation, the mass extinction coefficient of MOF at 808 nm was 78.2 L g<sup>-1</sup> cm<sup>-1</sup>, and the temperature quickly rose to  $\sim$  52  $^{\circ}$ C within 5 min. In addition, their results showed that this material possessed photothermal cycling ability. On the other hand, the Mn nodes also offered the MOF with MRI guidance. More recently, Lü et al. reported a Zr-PDI (PDI refers to perylenediimide) MOF with high photothermal conversion efficiency. 49 PDI can be reduced into PDI • -, which is a delocalized radical anion with red-shifted absorption compared to the PDI molecule. However, PDI - is unstable in ambient conditions. To solve this problem, the authors coordinated PDI with Zr<sub>6</sub> clusters, forming Zr-PDI MOF (Fig. 17a-c). The Zr<sub>6</sub> cluster was coordinated with 12 carboxyl groups, and the PDIs showed axial chirality (Fig. 17b). Zr-PDI can obtain electrons from electron donors (e.g., amine vapors) through photo-induced electron transfer (PET), generating radical anion Zr-PDI•-. In this work, the PET process was performed by irradiating Zr-PDI with blue light (455 nm) in amine vapor (Fig. 17d). The absorption of Zr-PDI • was obviously red-shifted (Fig. 17e). Due to the shielding effect of the MOF structure, the quenching of radical anions was efficiently prevented. Zr-PDI• is the first reported stable isolated radical anion, which retained the high light-to-thermal conversion of PDI • with a photothermal conversion efficiency of 52.3% (Fig. 17f), showing great promise in PTT. More recently, Deng et al. used 1,1'ferrocenedicarboxylic acid (Fc(COOH)2) as a ligand that was coordinated with Zr nodes. 103 The final product was termed as Zr-Fc MOF, which is a 16.4 nm thick MOF nanosheet. The PTT

**Review Article** Chem Soc Rev

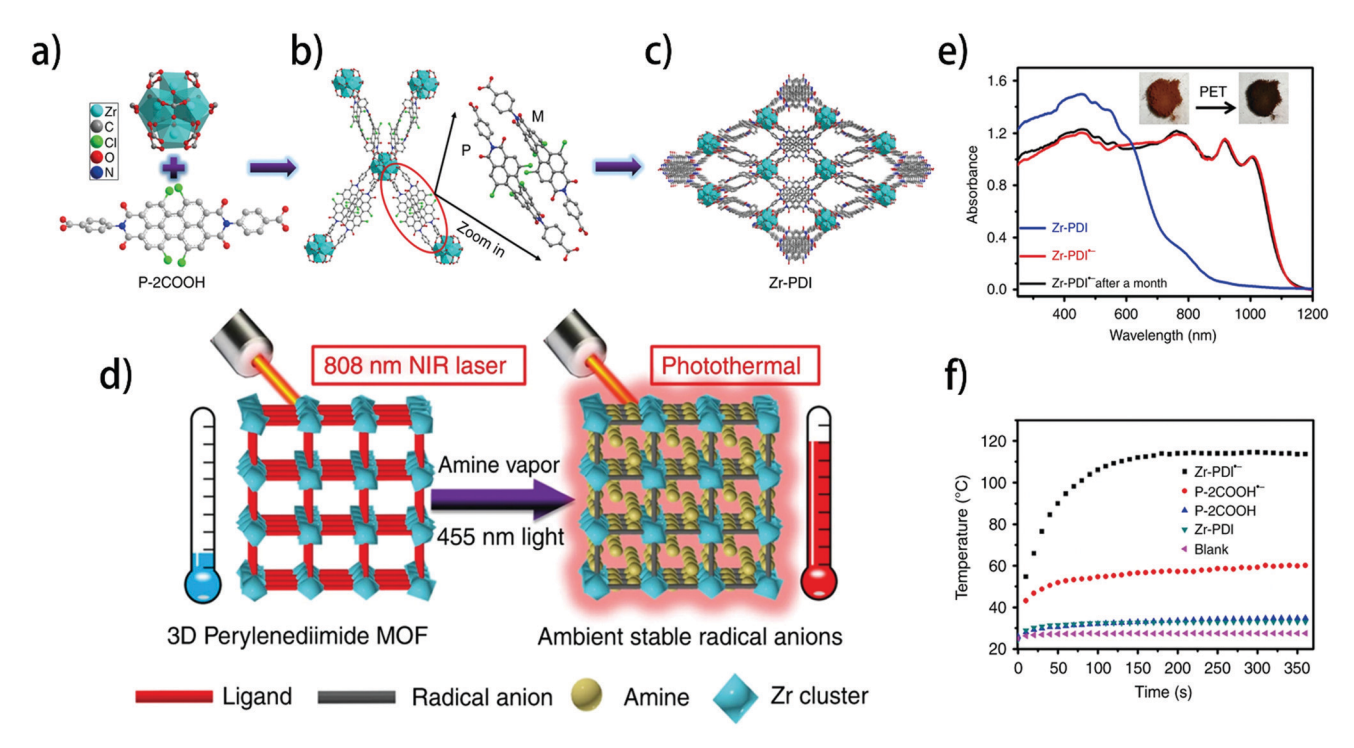


Fig. 17 (a) Structures of the Zr-cluster and P-2COOH. (b) Connection mode of the Zr-cluster (the Zr-cluster is fully coordinated by 12 carboxylate units) and the molecular arrangement of chiral P-2COOH. (c) c-Axis crystal structure of Zr-PDI. (d) UV-vis-NIR absorption of Zr-PDI, Zr-PDI. and Zr-PDI. after a month. The insets show the photographs of color changes. (e) Illustration of the colored PDI\*- formation and photothermal conversion of Zr-PDI<sup>•-</sup>. (f) Photothermal conversion curves of Zr-PDI<sup>•-</sup> films on quartz glass under laser irradiation (808 nm, 0.7 W cm<sup>-2</sup>). Reprinted with permission from ref. 49, Copyright 2019 Nature.

effect was attributed to the ferrocene ligand. Zr-Fc MOF showed broad absorption in the region of 350-1350 nm. Under 808 nm light irradiation, the temperature of Zr-Fc reached 92 °C in 3 min, while for Fc(COOH)<sub>2</sub>, the highest temperature was merely 46.8 °C. This difference was derived from the greater stability of Zr-Fc MOF. Besides, the radiative decay of Zr-Fc MOF was inhibited as manifested by the fluorescence emission, which indicates that more excited photo-electrons decayed through nonradiative pathways, thus more heat was generated for PTT. Moreover, Zr-Fc can also act as a Fenton catalyst, which showed 3.3 times higher OH production at 45 °C as compared to that at 25 °C. Hence, when incorporated in the MOF structure, the ferrocene ligand could provide chemo- and photothermalsynergistic therapy, which was simple and straightforward.

As for mixed-ligand MOFs, Zheng et al. incorporated tetratopic porphyrin (TCPC) into Hf-UiO-66 with a content of 8 wt% (referred to as TCPC-UiO).273 As a porphyrin derivative, TCPC had photodynamic activity. However, the ROS yield of TCPC-UiO was much less than the free TCPC molecule, which was probably ascribed to the weakened confinement of TCPC and the resulting aggregation. Instead, the photothermal ability of TCPC played a dominant role in this therapeutic system. Under 630 nm light irradiation, the temperature increased to 42 °C within 5 min at the lowest NPs concentration. The tumor inhibition also reached up to 90% after treatment. Therefore, the photothermal ability of porphyrin-based MOF is also worth exploring.

In terms of photothermal nodes, Zhou et al. reported a porphyrin-palladium MOF (Pd-MOF) composed of Pd nodes and 5,10,15,20-tetrakis(4-pyridyl)-21H,23H-porphine (TPyP) ligands for hydrogen-thermal therapy. 104 The photothermal effect was attributed to a single-atom Pd unit, and the photothermal efficacy was up to 44.2%. More importantly, Pd nodes have specific coordination ability with hydrogen. After hydrogenation, the obtained PdH-MOF had high hydrogen loading. The continuous hydrogen release could effectively scavenge OH and ONOO, causing the disorder of tumor energy metabolism. Hydrogen therapy also lowered the required intensity of light in PTT.<sup>274</sup>

4.1.3 Photothermal effect by ligand-to-metal charge transfer. For coordination structures such as MOF, the electrons go through not only interband transition, but also various charge transfer processes such as metal-to-ligand charge transfer and ligand-to-metal charge transfer, etc. 91 Ligand-to-metal charge transfer (LMCT) occurs when the metal nodes are in a relatively low valence state. When the material is excited, the electron will move from the donor orbital of the ligand to the accepting orbital of the metal nodes. 91 LMCT endows materials with strong absorption in the low-energy regions, such as the visible light and NIR light region, which facilitates photothermal ability. 91,275 The reported combinations of metal nodes and linkers used in PTT are given in Fig. 18.275-277

Liu et al. fabricated Fe-CPND composed of Fe3+ nodes and gallic acid ligand, which was protected by PVP. 275 The Fe-CPND was 5.3 nm in size, which can be cleared by the kidneys, thus

**Fig. 18** Typical combinations of intrinsic photothermal MOFs based on ligand-to-metal charge transfer.

lowering the toxicity of the material. In an acidic environment, the gallic acid ligand gradually disassociated from Fe-CPND and the Fe3+-gallic acid complex changed from tris- to biscoordination, which was attributed to the change in the coordination number of gallic acid. This pH-induced structural change endowed Fe-CPND with higher longitudinal relaxivity at pH = 5.0. Hence, the MRI ability of Fe-CPND can be triggered by tumor acidity. The LMCT effect was attributed to the phenolic oxygen on gallic acid. Under 808 nm light irradiation, the temperature of Fe-CPND quickly rose to 50 °C, which significantly inhibited tumor growth. Moreover, the absorption of Fe-CPND did not change after being irradiated for 60 min, which indicates the good photostability of Fe-CPND. More recently, it has been reported that MOFs composed of Fe<sup>3+</sup> metal nodes and ellagic acid<sup>277</sup> or hydrocaffeic acid ligands<sup>276</sup> can be used as PTAs due to the LMCT effect. Similar to the gallic acid ligand mentioned above, both ellagic acid and hydrocaffeic acid can form complexes with Fe<sup>3+</sup>. The photothermal ability of this kind of MOF originated from the Fe-phenol structure, which resulted in the LMCT effect. Hence, these findings could inspire the design of MOF compositions in the future exploration of intrinsic photothermal MOF.

## 4.2 Modifications via photothermal agents

Photothermal MOFs can be fabricated by the encapsulation of PTAs, such as indocyanine green (ICG) and its derivatives. The chemical structures are presented in Fig. 19. 66,185,278

Cai et al. loaded indocyanine green (ICG) in HA-coated MIL-100(Fe) with a loading content of 40%. <sup>278</sup> In vitro tests manifested that under 808 nm light irradiation for 3 min, the temperature could reach up to 70 °C, and the temperature could remain for 10 min, while free ICG solutions reached 65.47 °C after 3 min of irradiation but soon decreased due to the poor photostability of ICG. This result indicates that the

Fig. 19 Chemical structures of PTAs that can be encapsulated in MOFs

encapsulation in MOF can improve the photothermal ability of ICG, which was ascribed to the better photostability of ICG under the protection of the MOF. Moreover, Fe nodes and HA also rendered the integration of fluorescence imaging, PA imaging and MRI guidance. Zhu et al. encapsulated Pd nanosheets and DOX in ZIF-8 through a one-pot strategy, and coated ZIF-8 with PDA. 279 The Pd nanosheets acted as a PTA, which was 17 nm in size. After the encapsulation of Pd nanosheets, the particle size of ZIF-8 increased from  $\sim 150$  to  $\sim$  300 nm. After the coating of PDA, the photothermal conversion efficiency of the final product was 45%. Besides the photothermal effect, this material also has pH-controlled drug release ability. Zhang and coworkers used IR820 as the bond between the anticancer drug cytarabine (Ara) and ZIF-8 to improve the interaction between the model drug and MOF.66 ZIF-8 was further covered with HA to realize active targeting through enhanced permeability and the retention effect. Due to the small molecular size and lack of strong bonding functional groups, Ara was hard to load in the MOF without leaking. In their work, the amino bond of Ara was firstly bonded with the carboxyl bond of IR820, forming a prodrug. Then, the prodrug was loaded in ZIF-8 by coordinating with the sulfonic group of IR820 with a loading content of 39.8%. In the acidic tumor area, ZIF-8 would decompose, after which the amide linkage was hydrolyzed by amidase, releasing Ara for chemotherapy. ZIF-8 also improved the photostability of IR820, which resulted in higher photothermal conversion efficacy and high-temperature increase (26.7 °C).

#### 4.3 MOF-derived carbon materials

MOF-derived carbon materials are fabricated by MOF pyrolysis, which possess high porosity and controllable structures. 280-282 During pyrolysis, the metal cations in the MOF are reduced to isolated metal sites, and the organic linkers are changed into carbon supports due to carbonization.<sup>283</sup> The heteroatoms on organic linkers (e.g., N atoms on the 2-mIm linkers of ZIF-8) remained on the carbon framework. 280,284 To add more metal sites to this carbon material, metal precursors can be preencapsulated in the MOF before pyrolysis.285 Moreover, the carbon defects, metal sites and the graphitic contents can be tuned by different pyrolysis conditions.<sup>284</sup> Like the traditional carbon materials, MOF-derived carbon materials also have light-to-thermal conversion ability, which can be used for PTT. More importantly, the doped metal atoms and heteroatoms can be used for single-atom catalysts. 283,285,286 To be specific, if the organic linker contains nitrogen, a M-N-C structure (M refers to Co, Fe, Mn, Zn, etc.) can be generated after pyrolysis under certain environments, wherein the metal centers are coordinated with several N atoms, forming the M-Nx structure, and each metal site is isolated.<sup>287</sup> Compared to the bulk or nanocatalysts, single-atom catalysts are on the atom scale, which means they have much higher efficiency than traditional catalysts.<sup>283</sup> Therefore, single-atom catalysts have been widely applied in the O2 reduction reaction288 and CO2 reduction reaction, etc. 289 In biomedical applications, it can also generate

**Review Article** Chem Soc Rev

OH through the Fenton reaction, which is comparable to natural enzymes. 287,290

Huo et al. fabricated a single-atom catalyst based on an Fe-decorated ZIF-8 precursor that could combine PTT with OH generation chemotherapy (Fig. 20a).<sup>290</sup> The authors firstly encapsulated Fe<sup>III</sup> acetylacetone in ZIF-8 by a precursor isolation strategy, and the composite was then subjected to pyrolysis at 800 °C. After the pyrolysis, Fe atoms from Fe<sup>III</sup> acetylacetone were coordinated with neighboring N atoms, forming the Fe<sub>1</sub>-N<sub>x</sub> structure, which was used for single-atom Fe nanocatalysts, termed as SAF NCs (Fig. 20b). The loading of the Fe single-atom was 1.54 wt%. The OH production rate of this material is much higher than that of Fe<sub>3</sub>O<sub>4</sub>, and the OH production is accelerated in an acid environment. The \*OH generation mechanism is shown in Fig. 20c and d. When an H<sub>2</sub>O<sub>2</sub> molecule approached SAF NCs, it was firstly absorbed on the Fe atom of the Fe-N<sub>4</sub> structure, and then cleaved by the homolytic path, releasing a OH and leaving a hydroxyl group on the Fe atom. In an acidic environment, the residual hydroxyl group can be desorbed from the Fe atom in the form of a H<sub>2</sub>O molecule by reacting with a protonated hydrogen atom. Hence, this Fe-N<sub>4</sub> structure can be used for decomposing another H<sub>2</sub>O<sub>2</sub> molecule. However, in a neutral environment the desorption of OH\* is much harder (Fig. 20d) due to a lack of protonated hydrogen atoms. Although the residual hydroxyl group can be attached to another H<sub>2</sub>O<sub>2</sub> group through hydrogen bonding, the OOH formation and desorption is hard to occur due to a high energy barrier. Hence, in a neutral environment, the catalytic activity of the single-atom catalyst is inhibited. To improve its biocompatibility, SAF NCs was further PEGylated, referred to as PSAF NCs, which could induce the ferroptosis of tumor cells. The resulting lipid peroxidation also contributed to tumor cell death. The tumor

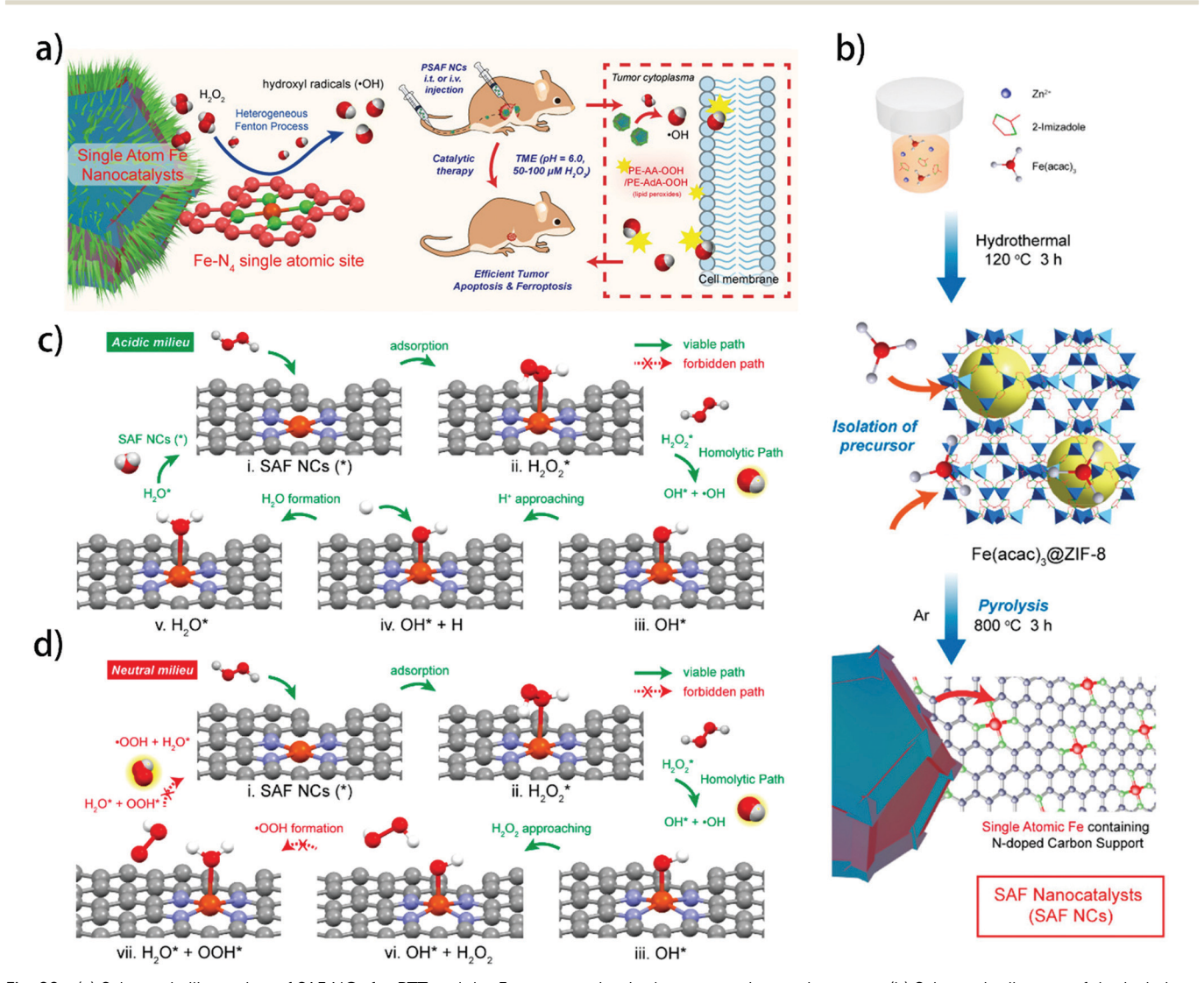


Fig. 20 (a) Schematic illustration of SAF NCs for PTT and the Fenton reaction in the tumor microenvironment. (b) Schematic diagram of the isolationpyrolysis approach to synthesizing SAF NCs. Proposed reaction mechanism schematics for SAF NCs in the heterogeneous Fenton reaction toward generating \*OH under (c) acidic (protonated) and (d) neutral catalytic milieu. Reprinted with permission from ref. 290. Copyright 2019 American Chemical Society.

Chem Soc Rev

inhibition rate of PSAF NCs without light irradiation was up to 63.5%. As for PTT, under 808 nm light irradiation, the temperature of PSAF NCs increased by 45  $^{\circ}$ C. With the assistance of PTT, PSAF NCs could achieve complete eradication of tumor.

For ion release-related applications, Yang et al. annealed ZIF-8 under an Ar atmosphere, 800 °C and O2 atmosphere, 200 °C, respectively, after which the ZIF-8 was turned into ZnOdoped carbon NPs with a diameter of 50 nm. 291 Afterwards. poly(N-isopropylacrylamide) (PNIPAM) was coated, which served as a thermo-responsive gel layer. The final product was called ZnO-CNP-TRGL. Under 5 min of 808 nm light irradiation, the temperature of ZnO-CNP-TRGL increased to 55 °C, confirming the photothermal ability of this ZIF-8-derived carbon material. Moreover, when immersed in phosphate buffer solution (PBS), about 0.63 wt% of Zn<sup>2+</sup> from ZnO-CNP-TRGL was released, which can destroy the membranes of the bacteria and cause the denaturation of proteins and enzymes. Moreover, the thermoresponsive gel layer changed from highly hydrophilic to hydrophobic when the temperature increased from room temperature to higher than the lower critical solution temperature of PNIPAM. Hence, at a higher temperature, ZnO-CNP-TRGL can form bacterial aggregations due to its hydrophobicity and the hydrophilic adhesin proteins on bacteria. The bacteria trapping process occurred at 40 °C, and the material showed complete bacterial eradication of S. aureus when the temperature was higher than 45 °C, due to the synergistic effect of PTT, Zn<sup>2+</sup> release and bacteria trapping. Fan and coworkers in situ fabricated ZIF-8 on graphene oxide nanosheets, which was then carbonized under an Ar and O2 atmosphere, successively.292 The as-obtained ZnOdoped graphene was grafted with transformable thermal-responsive brushes, giving rise to TRB-ZnO@G. When the temperature rose to 56 °C by the PTT effect, the polymer brushes changed from hydrophilic to hydrophobic, which can be used for bacteria trapping. The 2D morphology of graphene nanosheets can also kill bacteria via physical cutting.

#### 4.4 MOF-based composites

4.4.1 MOF-photothermal polymer composites. Polymers have been widely applied in MOF-based therapeutic systems for better stability and biocompatibility.<sup>293</sup> Besides this property, polypyrrole (PPy), <sup>39,294</sup> PDA<sup>295</sup> and polyaniline (PAN), <sup>296</sup> etc. have additional photothermal ability. In the hybridization of photothermal polymers and MOF, polymers are usually in the form of surface coating, core structure, decoration NPs or in situ polymerized in the pores of MOF. Zhu et al. synthesized PPy NPs, and introduced PVP on PPy NPs to facilitate the nucleation of MIL-100. 294 Afterwards, DOX was loaded in MIL-100. The release of DOX was influenced by both low-pH-induced MOF decomposition and NIR irradiation-induced temperature increase. In their work, PPy served as the PTA, and its combination with MIL-100 provided feasibility for drug loading-assisted PTT. Wang et al. utilized UiO-66 to absorb aniline monomer through electrostatic interaction. Afterwards, the oxidizing agent, ammonium persulfate, was added to trigger the polymerization. PAN was polymerized on the surface of UiO-66, giving a smooth surface of the particle. Due to the strong absorption of PAN in the NIR region, the

maximum temperature under irradiation was 57.2  $^{\circ}$ C, and its photothermal conversion efficiency was 21.6%.

The small size of the polymer monomer makes it easy to be introduced and subsequently polymerized in the nanopores of MOF; this method is called in situ polymerization. By this method, it is easy to control the polymer size and generate a uniform hybrid of MOF and polymers. 293 Huang et al. fabricated MIL-53, which has mixed-valent Fe nodes.<sup>297</sup> The unsaturated coordination of the Fe3+ node can be used to oxidize the polymerization of Py. After the in situ polymerization of PPy, MIL-53 retained its structure and drug loading capacity. The DOX loading content in MIL-53 was up to 90%, and the release of DOX was triggered in an acidic environment. Under 808 nm light irradiation, the temperature increased by 22.1 °C at 0.50 mg mL<sup>-1</sup> with good photostability. The PPy@MIL-53 composite can also act as a contrast agent for MRI. Wang et al. firstly blended dopamine monomer with manganese acetate, which formed coordination bonds through phenolic hydroxyl groups.<sup>53</sup> Afterwards, the ligand precursor, K<sub>3</sub>[Co(CN)<sub>6</sub>], was added to the mixture. Hence, the dopamine monomer was loaded in the pores of MnCo MOF, which is a PB analogue. After 24 h of stirring, dopamine was in situ polymerized, forming the composites of PDA and MnCo, referred to as MCP, which was further attached with PEG and tumor-targeting peptide cRGD-SH (cyclic arginine-glycine-aspartic acid). Due to the  $\pi$ - $\pi$  stacking between -C≡N and dopamine, the absorption of MCP showed an extra absorption at 550-700 nm, which indicates that the absorption of MCP was enhanced. The photothermal conversion efficiency of MCP was 41.3%, which was higher than that of PDA NPs (36.9%). Hence, in situ polymerization could enhance the therapeutic efficacy of photothermal polymers, and the MnCo structure also provided feasibility for MRI and targeting molecule attachment.

4.4.2 Core-shell structure. Traditional photothermal NPs such as Au-based particles (Au nanorods, 298 Au nanostars, 52,299 and Au NPs300-302), Pd nanocubes,99 magnetic carbon,303 PB, and photothermal polymers, etc., usually lack homogeneous targeting and drug loading capacity. Moreover, the particles also suffer from aggregation. Coating the MOF shell on the photothermal core not only makes up for these shortcomings but also improves the crystallinity of the composite. 304 As PBand polymer-based core-shell structures have been discussed above, we firstly take Au-based particles as an example. The photothermal ability of Au particles mainly stems from the LSPR effect under light irradiation. 82 Li et al. fabricated a single gold nanorod (AuNR) of 47 nm in diameter and 12 nm in length.<sup>298</sup> Afterwards, ZIF-8 was synthesized on PVP-stabilized gold nanorods and loaded with DOX. The LSPR absorption peak of AuNR@ZIF-8 shifted to ~810 nm as compared to the sole AuNR ( $\sim$  790 nm), which was attributed to the influence of the ZIF-8 shell. Owing to the AuNR core, the nanocomposite showed potent photothermal efficacy under 808 nm NIR light irradiation. The release of DOX was triggered by the acidic environment and NIR light irradiation because of ZIF-8 decomposition, thus enhancing the potency of therapy. Deng and coworkers reported a ZIF-8-covered Au nanostar, which was

further etched by tannic acid.<sup>52</sup> The cavity between ZIF-8 and the Au nanostar was utilized to store DOX. The Au nanostar has strong absorption in the second NIR light (NIR-II) region (1000–1350 nm). Owing to the deeper penetration and larger maximum permissible exposure, the NIR-II-based PTT has better therapeutic efficacy. The composite had higher photothermal conversion efficiency under 1064 nm light (48.5%) as compared to 808 nm light irradiation (30.2%). The generated heat also dissociated the Zn–O coordination bond, thus accelerating the DOX release. Moreover, the strong absorption also provided PA imaging and infrared photothermal imaging.

**Review Article** 

Besides Au-based NPs, Deng *et al.* coated MIL-100 on magnetic carbon NPs.  $^{303}$  The MOF shell was PEGylated and subsequently modified with Mn carbonyl. Finally, DOX was loaded in MIL-100. The magnetic carbon core served as a PTA for PTT, and it also provided PA imaging and MRI response for imaging guidance. The  $[Mn(CO)_5]^+$  moiety was used as the CO source for gas therapy, and the CO capacity was 1.16% (w/w). Under 808 nm light irradiation, the temperature elevation not only accelerated the DOX release, but also triggered CO therapy. The combined CO therapy facilitated the escape of the composite from lysosomes, guaranteeing the efficacy of the drug, and also made up for the deficiency of the relatively low photothermal temperature.

#### 4.5 Enhancing the efficacy of photothermal therapy

4.5.1 Improving photothermal conversion efficiency. Generally, for PTAs, high photothermal conversion efficiency can decrease the irradiation time, laser power density and PTA dose, thus minimizing tissue damage.305 Therefore, many methods have been devoted to increasing the photothermal conversion efficiency. As mentioned in Section 2, two processes are related to the photothermal effect: light absorption and nonradiative relaxation of electrons. To improve the photothermal conversion efficiency, researchers can optimize the absorption of the material or create more nonradiative pathways. To date, several strategies have been put forward as follows: (i) increasing the density of DLDs;<sup>70</sup> (ii) introducing more electron circuit loops through the heterostructure;306 (iii) narrowing the bandgap;307 (iv) introducing more CR pathways;<sup>56</sup> (v) optimizing LSPR absorption;<sup>249</sup> (vi) transferring electron transition from the bandgap to the LSPR,54 etc. Here, we listed some examples of enhancing the photothermal conversion efficiency of MOF-based materials.

Cai *et al.* doped  $Gd^{3+}$  in PB for the tunable LSPR and enhanced MRI ability. <sup>249</sup> It is known that LSPR is based on the collective oscillations of free charge carriers. In PB, the free charge carrier mainly refers to  $[Fe(CN)_6]$ . The position of the  $Gd^{3+}$  dopant was firstly at the interstitial site, which had no impact on the  $[Fe(CN)_6]$  vacancy. With the increase of  $Gd^{3+}$  concentration, the dopant position changed to the lattice site, forming the  $Fe-C \equiv N-Gd$  structure. The number of  $[Fe(CN)_6]$  vacancies was therefore decreased. Simultaneously, the electron density and orbital energies of  $-C \equiv N-$  were also affected by lattice  $Gd^{3+}$ . As a result, the LSPR absorption peak red-shifted from 710 to 910 nm. The authors adjusted the absorption peak to around 808 nm, which was beneficial for applying 808 nm irradiation, giving rise to a much enhanced photothermal efficacy.

Additionally, as a typical contrast agent,  $Gd^{3+}$  improved the MRI efficacy of PB. Moreover, the Gd-doped PB can also reduce oxidative stress by scavenging ROS.

Li et al. doped PB with Zn with increasing doping levels, which were called ZnPB-1, -2, and -3.54 Fe2+ in PB was replaced by Zn<sup>2+</sup>, forming the Fe-C≡N-Zn structure. As shown in Fig. 21a, the structure of PB was simplified into two kinds of octahedrons with Fe located at the center (Fe(III)-N and Fe(III)-C). The Zn doping gave rise to another octahedron that was centered with the Zn atom (Zn(II)-C). Along with increasing the Zn dopant concentration, the bandgap of ZnPB decreased from 1.72 to 1.65 eV according to density functional theory, which was also proved by experimental calculations (Fig. 21b). On the other hand, the electronic density also increased with more Zn doping, which gave rise to the major electron transition changing from bandgap to LSPR. Due to the hybridization of Zn dopant and crystal structure interaction, the NIR absorption peak of PB red-shifted to the lower energy region (Fig. 21c). Owing to the narrowed bandgap and redshifted LSPR, the photothermal conversion efficiency of Zn-doped PB reached up to 39.79% (ZnPB-3). Under 808 nm light irradiation, the temperature of ZnPB-3 could increase to above 50 °C, which is the required temperature for bacteria-killing. Moreover, the heat generated from the enhanced photothermal effect also facilitated the diffusion of interstitial Zn<sup>2+</sup>, which improved the collagen deposition for wound healing. To sum up, ZnPB-3 had excellent short-term and long-term antibacterial ability against E. coli, S. aureus, and MRSA biofilm.

Yu et al. coated PB on NaNdF4 particles, forming a core-shell structure (NdNP@PB).56 During fabrication, citric acid was applied as a surfactant to provide growth sites for PB and improve the stability of NP (Fig. 21d). The ladder-like energy levels of Nd<sup>3+</sup> have cross-relaxation (CR) pathways between Nd3+ ions. Since the CR process and the subsequent photon relaxation to the ground state can contribute to heat generation (Fig. 21e), NaNdF4 can be used as PTA, but its photothermal conversion efficiency was merely 8.7%. One way to improve the photothermal conversion efficiency was by increasing the Nd3+ concentration to generate more CR pathways between the same lanthanide ions (Fig. 21f). However, increasing the doping content of Nd3+ to even 100% cannot provide enough photothermal effect. Therefore, new CR pathways needed to be introduced. PB has a continuous energy band. When the energy band of PB was in close contact with that of NaNdF4, new CR pathways with shorter distances were generated (Fig. 21g). Therefore, the nonradiative relaxation distance was much longer, leading to better PTT effects. Hence, NdNP@PB showed a much enhanced photothermal conversion efficiency of up to 60.8%, and the tumor growth inhibition of NdNP@PB was 76.7%.

**4.5.2 Low-temperature photothermal therapy.** Another important factor of PTT is therapeutic temperature. As high-temperature PTT will result in serious damage to ambient healthy tissue, researchers put forward the low-temperature PTT (*e.g.*, 43 °C) strategy. The main concern of low-temperature PTT is the cell's resistance to hyperthermia, which is related to a higher expression of heat shock proteins (HSPs) in the low-temperature region. Zhang and coworkers encapsulated siRNA, which is an HSP 70 inhibitor, in the Zr-ferriporphyrin MOF

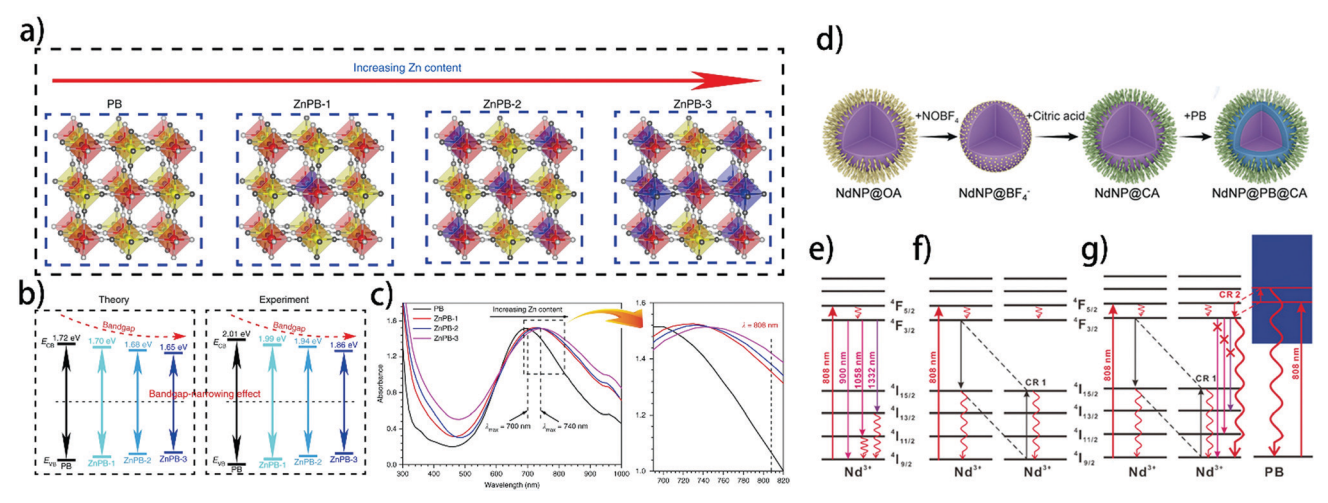


Fig. 21 (a) Simplified geometrical structure of PB and ZnPB with various doping levels (color coding: Fe(III) - red, Fe(II) - yellow, Zn - blue, N - grayish and C - dark gray). (b) Scheme of bandgap-narrowing effect with the increase of Zn-doped density by theory and experiment. (c) UV-vis-NIR spectra of PB, ZnPB-1, ZnPB-2 and ZnPB-3. Reprinted with permission from ref. 54. Copyright 2019 Nature. (d) Synthesis of NdNP@PB. Simplified diagrams of the (e) radiative and nonradiative processes in a single Nd3+ ion, (f) CR between Nd3+ ions, (g) generation of new CR pathways between Nd3+ ions and PB. Reprinted with permission from ref. 56. Copyright 2019 Wiley.

(siRNA/Zr-FeP) with a loading capacity of 76.13%. 145 Under 635 nm light irradiation, the temperature increased to 45.4 °C, and the photothermal conversion efficiency was 33.7%. The release of siRNA was triggered by tumor acidity and heat. It was observed that the expression of HSP 70 was inhibited after treatment with siRNA/Zr-FeP. Animal testing manifested that siRNA/Zr-FeP had the best therapeutic efficacy due to the inhibited thermal resistance. Another strategy is inhibiting the generation of ATP, which is related to the expression of HSP. This strategy can be used for combining PTT with starvation therapy. Zhou et al. loaded GOx in HMPB and coated them with HA. Upon irradiation for 5 min, the temperature reached 45 °C by HMPB. 25 After endocytosis, the intracellular GSH can cleave the disulfide bond between HMPB and HA, triggering the release of GOx. HMPB then decomposed H<sub>2</sub>O<sub>2</sub> to increase the O<sub>2</sub> content for the oxidization of glucose. Results showed that after the treatment, the ATP level of HepG2 and HL-7702 cells decreased and the expressions of both HSP70 and HSP90 were dramatically inhibited. Therefore, the efficacy of low-temperature PTT was improved, and the combined starvation therapy also contributed to tumor growth suppression.

4.5.3 Drug release controlled by phase-change material. Drug loading is a ubiquitous combined therapy for MOFbased PTT, as MOF is an ideal drug carrier and photothermal heat can accelerate the diffusion of the drug. PTT also enhances the sensitivity of chemotherapy. <sup>252</sup> Based on these properties, precise control over drug release was achieved by introducing phase-change materials (PCM) such as 1-pentadecanol, 308,309 tetradecanol<sup>295</sup> and lauric acid.<sup>310</sup> Only when the temperature rises above the melting point of PCM will the loaded drug be released. Therefore, in blood circulation, this strategy can realize "zero drug leakage". Zhang et al. incorporated DOX and losartan with lauric acid, and encapsulated them in HMPB.<sup>310</sup> After 10 min of 808 nm NIR light irradiation, the

maximum temperature of the composite rose to 59.2 °C, which was above the melting point of lauric acid (44.7 °C), thus triggering the release of DOX and losartan. After 21 min of irradiation, the release rate of DOX was up to 21.9%, while almost no release was observed under 3 min of irradiation. Moreover, the released losartan could enhance the penetration of DOX by degrading extracellular matrices. Therefore, the combination of controlled-drug release and PTT gave rise to a tumor inhibition rate of up to 81.3%. Wu and coworkers covered ZIF-8 with PCM and PDA after loading DOX in the MOF.<sup>295</sup> The melting point of the PCM, tetradecanol, was 38-40  $^{\circ}$ C. The photothermal ability was attributed to PDA coating. The DOX release was controlled by both NIR irradiation and pH value, and NIR light-triggered PCM degradation was more critical. Within 5 min of 808 nm light irradiation, the temperature increase in aqueous solution was 34.6 °C (500 μg mL<sup>-1</sup>), which was above the melting point of the PCM shell. Additionally, the tumor acidity-induced ZIF-8 decomposition also accelerated the DOX release. Hence, the drug release amount under both NIR irradiation and pH 5.0 was up to 78%.

# 5. Photodynamic and photothermal synergistic therapy

Although both PDT and PTT have been reported to be efficient strategies in clinical applications, there are still some drawbacks in each therapy. First of all, due to the hypoxia in the therapeutic area, it is hard to satisfy the O2 demand of PDT, which hinders the ROS generation.<sup>67</sup> As for PTT, improving photothermal conversion efficiency requires complex modification. 141 Another concern is that to achieve sufficient ROS yield or temperature increase, the laser power density is usually high, which might cause lesions in healthy tissues. 187 To solve these problems,

combined therapies have been put forward, such as chemotherapy, <sup>263,311,312</sup> gas therapy, <sup>46,112,255,256</sup> etc., which adds to the complexity of the design. As PDT and PTT can be simultaneously triggered by light irradiation, combining PDT and PTT in one therapeutic system is a promising way to overcome the disadvantages of PDT and PTT. Moreover, the heat generated by PTT can improve the blood flow, and consequently increase the ambient O<sub>2</sub> content to alleviate hypoxia. <sup>145</sup> On the other hand, targeted cells also become more sensitive to heat due to the interference of PDT. <sup>145</sup> Therefore, PDT and PTT can work synergistically. In this section, we will discuss how to construct PDT and PTT synergic therapeutic systems based on MOFs.

**Review Article** 

The "all-in-one" strategy means incorporating both photothermal and photodynamic ability in one MOF without further modification. Han et al. introduced Cu2+ into the porphyrin ligands of PCN-224 with various doping levels (5%, 10%, 15% and 25%). 146 The Cu2+ dopant could trap electrons, thus hindering the recombination of electron-hole pairs. After the electron trapping, Cu<sup>2+</sup> was reduced to Cu, which could react with holes and decrease the photocatalytic ability. Therefore, the dopant concentration should be moderate. Their results showed that PCN-224 with 10% Cu2+ dopant (denoted as Cu<sub>10</sub>MOF) had the highest <sup>1</sup>O<sub>2</sub> generation and relatively higher absorption at 660 nm. Moreover, the d-d transition of the chelated Cu<sup>2+</sup> provided the photothermal effect. Under 660 nm light irradiation, the temperature of Cu<sub>10</sub>MOF was the highest (48.4 °C). Therefore, the synergistic therapy of Cu<sub>10</sub>MOF exhibited 99.71% and 97.14% of bacteria-killing against S. aureus and E. coli, respectively. Li et al. reported a Cu-TCPP MOF nanosheet. 144 The thickness of the nanosheet was 5.1  $\pm$  0.3 nm, which rendered a quicker response to light as compared to the bulk material. The PDT effect of the TCPP ligand was triggered by 660 nm laser. Owing to the d-d transition of Cu<sup>2+</sup> nodes, Cu-TCPP also efficiently transforms light into heat. Under 5 min of 808 nm light irradiation, the temperature quickly increased 34.5 °C. Moreover, due to the unpaired 3d electrons of Cu<sup>2+</sup> nodes, the nanosheets could be used for MRI and infrared thermal imaging.

As mentioned in Section 4.3, the high-temperature pyrolysis of MOFs can generate MOF-derived carbon materials, which features photothermal conversion ability. If the ligand is N-containing, the MOF-derived carbon material can show a porphyrin-like M-N-C structure (M denotes metal center) under appropriate pyrolysis conditions, wherein the metal cations are dispersed and each of them is coordinated with 4 pyridinic nitrogen, which is similar to the coordination environment in porphyrin.313-315 Therefore, the porphyrinlike structure further endows this material with PDT ability. Wang and coworkers coated ZIF-8 with mesoporous silica, followed by high-temperature pyrolysis.313 Afterwards, mSiO2 was removed by NaOH etching. This surface protection prevented the aggregation of the M-N-C structure during pyrolysis. The diameter of the as-obtained material (referred to as PMCS) was about 140 nm, and it retained the porosity of the ZIF-8 precursor. Similar to other carbon materials, PMCS had strong absorption in the NIR region. PDT and PTT were simultaneously triggered by

the 808 nm laser. The singlet oxygen quantum yield of PMCS was comparable to that of ICG, and the photothermal conversion efficiency was 33.0%. Due to the strong absorption, PMCS can serve as the contrast agent for PA imaging. The combination of imaging guidance, PTT, and PDT showed complete eradication against tumors.

Some dyes have been reported to have both ROS generation and light-to-heat conversion ability. Gao et al. applied UiO-66 as the O<sub>2</sub> carrier and coordinated ICG on the surface of UiO-66. 184 Afterwards, the nanoparticles were coated with red blood cell membrane. ICG served as both PS and PTA. Under 808 nm light irradiation, the temperature increased to 43.5 °C. The generated heat accelerated the diffusion of O<sub>2</sub> from the inner UiO-66 core, which in turn facilitated the PDT efficacy of ICG. Cypate is another organic dye that features photodynamic, photothermal, and versatile imaging abilities. Yang and coworkers introduced cypate during the fabrication process of MIL-53, denoting as CMNP. 185 CMNP was then coated with PEG and transferrin (referred to as CMNP-Tf). During fabrication, a cypate-Fe<sup>3+</sup> precursor was firstly formed owing to the coordination bond between the carboxyl of cypate and Fe<sup>3+</sup>. Then after the addition of ligand solution, MIL-53, with defects, was created. The defects can be used to control the pore size of MIL-53, which increased with increasing the concentration of cypate. This method increased the druggability and bioavailability of cypate, and also avoided its photobleaching. Due to the successful loading and versatility of cypate, CMNP-Tf showed complete tumor ablation with good biocompatibility.

Lastly, to synthesize MOF-based composites with PDT and PTT dual functions, researchers usually combine the above-mentioned PSs (dye, porphyrin-based MOF, etc.) and PTAs (Au-based PTA and photothermal polymer, etc.), which all achieved superior therapeutic efficacy. 142,182,186,267 Here, we mainly illustrate examples of multi-MOF core-shell structure. Liu et al. fabricated a dual MIL-101 core-shell structure by the in situ growth method, and decorated the outer shell with PEG-FA and cyanine 3-labelled peptide (referred to as BQ-MIL@cat-fMIL) (Fig. 22a). 186 The inner MIL-101 was loaded with black phosphorus dots (BQ), while the outer MIL-101 was loaded with catalase. Because of quantum confinement and edge effects, BQ is promising for combining PDT and PTT. The photosensitivity of MIL-101 resulted in a widened gap between the triplet state and the ground state of the composite, indicating that the excited BQ-MIL@cat-fMIL mainly reacted with <sup>3</sup>O<sub>2</sub> rather than went through phosphorescence emission. Therefore, the 1O2 generation of BQ-MIL@cat-fMIL was increased to 88.3%. Moreover, the catalase in the outer shell of MIL-101 efficiently provided O2 for the inner BQ by decomposing H<sub>2</sub>O<sub>2</sub>. Under 660 nm light irradiation, the apoptotic percentage was 52.1% by PDT, which was 8.7 times higher than that without catalase. On the other hand, the photothermal effect was triggered by 808 nm light, and the photothermal conversion efficiency was 23.3%, which provided 28.7% of cell apoptosis. After applying dual-light irradiation, the combination of PDT and PTT led to 75.6% of cell apoptosis.

Luo et al. coated PB with the UiO-66 MOF shell (Fig. 22b), which was used for bacteria-infected wound healing under

Chem Soc Rev a) b)

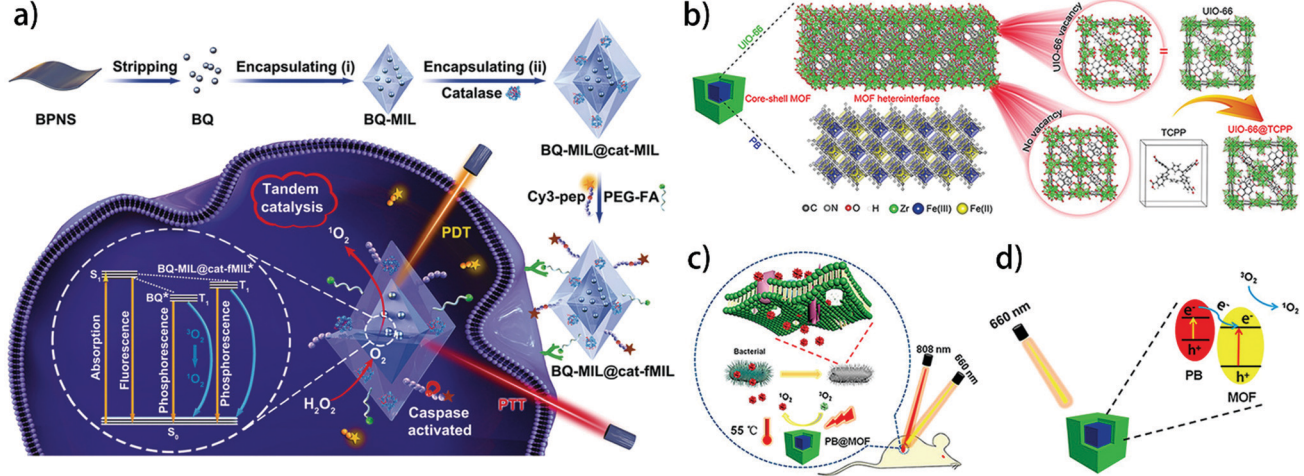


Fig. 22 (a) The stepwise assembly of BQ and catalase in MOF layers and its application as a tandem catalyst for enhanced therapy against hypoxic tumor cells. Reprinted with permission from ref. 186. Copyright 2019 Wiley. (b) Schematic illustration of the core-shell structure of PB@MOF. (c) Schematic illustration of the bacteria killing processes with the PB@MOF under dual light irradiation. (d) Schematic illustration of the rational photocatalytic mechanism for PB@MOF heterojunction photocatalysts. Reprinted with permission from ref. 267. Copyright 2019 American Chemical Society.

dual-light irradiation (660 nm light for PDT and 808 nm light for PTT (Fig. 22c)). 267 Taking advantage of the defects in the MOF structure, the outer UiO-66 was doped with TCPP, which served as PS. The core-shell structure not only combined two therapies, but also enhanced the photocatalytic ability by forming a heterojunction structure. Both PB and TCPP-doped UiO-66 (referred to as MOF) were n-type semiconductors. Their results showed that PB had a lower CB than the MOF (Fig. 22d). Hence, the photo-induced electrons of PB could move to MOF, accelerating the photo-electron transfer and inhibiting photoelectron-hole recombination. Though the photothermal effect of PB was partially hindered by the UiO-66 shell, the temperature still exceeded 50 °C within 5 min of irradiation. Moreover, the composite released trace amounts of Fe and Zr element during degradation, which facilitated the wound healing. Therefore, this core-shell dual-MOF composite is superior for bacterial infection treatment. Under dual-light irradiation, the PB@MOF composite showed more than 99% of antibacterial efficiency against S. aureus and E. coli.

# 6. Conclusions and perspectives

In the last decade, the applications of MOFs in phototherapy have presented a booming trend, as illustrated in this review. Due to the tunability of the MOF structure, MOFs could directly serve as PSs or PTAs by applying photo-responsive building units, or act as the carrier of phototherapeutic agents. The periodic array of MOFs prevent the aggregation and self-quenching of PSs and PTAs, which greatly enhances their efficacy. Moreover, the active sites and cavities of MOFs make numerous modifications feasible, such as combined therapy, active targeting and imaging guidance, etc. To date, many complex and elaborate designs have been put forward, indicating the great potential of

MOF in phototherapy. However, to push this field forward, we have listed some issues that need to be addressed.

In spite of the advantages mentioned in this review, phototherapy still has many limitations such as O2-dependence, inhomogeneous distribution of heat, and limited tissue penetration, etc. Future research on phototherapy may be combined with various therapies, including but not limited to chemotherapy, radiotherapy, gas therapy, starvation therapy and immunotherapy. Another concern is that the limited penetration is a big problem for phototherapy. Although the use of upconversion nanoparticles and two-photon activated PSs can improve the therapeutic depth, it is still difficult for phototherapy to cure deep-sited tumors or infections. Imaging guidance is another important auxiliary method in phototherapy, which can determine the location and morphology of lesions and monitor the distribution of therapeutic agents in order to provide the appropriate irradiation. More importantly, with the guidance of fluorescence, it is desirable to implant a light source in solid organs, which can be used for treating deep lesions.6 In view of these concerns, the MOF is an ideal carrier for these functions. To date, the combined therapy and imaging-assisted therapy based on MOFs have achieved good results. However, improvements are still needed for precise control, potent efficacy, resistance prevention and lowering tissue lesions before being applied in clinical settings.

Many researchers have mainly focused on improving the ROS yield and photothermal conversion efficiency of PSs and PTAs. However, other physiochemical properties of materials need to be taken into consideration as well, such as crystallinity, aqueous stability and degradability, etc. The specific mechanisms of photodynamic and photothermal effects should be further clarified, such as the electron transition pathway, and the correlation between radiative and nonradiative decays, which will shed light on the future design of MOFs with desirable ROS yields, photothermal conversion efficiency and other photorelated functions. On the other hand, the requirement of **Review Article** Chem Soc Rev

combined therapy gives rise to the integration of various therapeutic agents, and each of them has separate functions. More studies towards the synergistic effect of these agents are needed, from synthesis to treatment mechanisms. For example, the influence on MOF morphology and crystallinity, the interface interactions of core-shell structure, the synergistic effects of the drug and ROS, etc. After the in-depth understanding of the underlying mechanisms, researchers can build up a comprehensive correlation between composition, structure, properties, and efficacy, which is beneficial for fabricating highly effective rather than purely structurally sophisticated medical materials.

In terms of clinical applications, the most important concern is the biosafety of materials. Unfortunately, up to now, none of these therapeutic agents have been approved by the FDA, indicating that more attempts towards improving biosafety are needed. Although there have been reports about different surface coatings to improve the stability and biocompatibility of materials, researchers still need to consider every process of materials in the body, such as drug administration, circulation in the blood flow, degradation, and elimination from the body. The related properties including biodegradability, particle size and the release of various agents during degradation should be carefully designed. Many researchers have reported the features of the therapeutic area, such as hypoxia and the generation of acidity, GSH, ATP and H<sub>2</sub>S, etc., and they have put forward various responsive methods. However, the understanding of the therapeutic area is not enough, as the real microenvironment is more complex. The immune response and physiological properties of different tumors, bacteria, biofilms and other diseases still need further investigation.

Although most reported MOF-based PSs or PTAs are aiming at cancer treatment, ROS generation and temperature increase induced by light irradiation are promising in many other fields as well. For example, many researchers have applied PDT and PTT in antibacterial applications, which can be divided into water disinfection, 316,317 medical device sterilization, 318 wound healing, 319,320 and implant modification, 321-323 with light source ranging from the visible to NIR range. Moreover, the combination of PTAs and PCMs has been applied to fabricate the anticorrosion coating of magnesium alloy implants, which has light-induced self-healing ability.324 Therefore, the applications of PDT and PTT can be extended in various fields, which have different requirements for light penetration, ROS yield, and temperature increase. Besides the traditional material fabrication methods such as encapsulation and surface coating, some novel techniques such as biomineralization, 325-327 which combines materials with bacteria and viruses, can be used in phototherapy as well. As the penetration depth of light is limited, researchers can focus on superficial diseases such as dental antibacterial applications, which can better utilize the light source. MOFs have been successfully fabricated in the form of nanoparticles, membranes, 328 mixed-matrix membranes 117 and coatings, 329,330 which make it possible for MOF-based PSs and PTAs to adapt to different therapeutic conditions. Due to the unique structure of the MOF, it can be used as a precursor or template for fabricating new porous materials such as MOFbased carbon single-atom catalysts. Hence, on the basis of the reported phototherapy in cancer treatment, researchers can consider using these materials in other medical applications.

In conclusion, the applications of MOFs in phototherapy have been put forward and rapidly developed in the last decade. Under rational design, MOFs can improve the efficacy of traditional phototherapy with multiple combined functions, which is now attracting more and more attention. However, although we have seen the elaborate design of MOFs and good therapeutic efficacy in recent publications, the research on MOFs in phototherapy is in its infancy. Numerous efforts are still needed before it reaches clinical trials. We believe that the applications of MOFs in phototherapy will continue to expand, and finally become an important part of medical treatment.

## **Abbreviations**

ROS	Reactive oxygen species
PDT	Photodynamic therapy
PTT	Photothermal therapy
PS	Photosensitizer
${}^{ullet}\mathrm{O_2}^-$	Superoxide anion radical
•OH	Hydroxyl radical
$H_2O_2$	Hydrogen peroxide
$^{1}O_{2}$	Singlet oxygen
HPD	Hematoporphyrin derivative
FDA	Food and Drug Administration
$g-C_3N_4$	Graphic carbon nitride
PTA	Photothermal agent
MOF	Metal-organic framework
NP	Nanoparticle
$^{3}O_{2}$	Molecular oxygen
LSPR	Localized plasmon surface resonance
NIR	Near infrared
CB	Conduction band
VB	Valence band
DLD	Deep-level defect
CR	Cross relaxation
UV	Ultraviolet
SEM	Scanning electron microscope
TEM	Transmission electron microscope
DLS	Dynamic light scattering
$H_2DBP$	5,15-Di(p-benzoato)porphyrin
$H_2DBC$	5,15-Di(p-methylbenzoato)chlorin
LI TDC	E 10 1E 20 Totro(n honzoeto)

H<sub>4</sub>TBC 5,10,15,20-Tetra(*p*-benzoato) **PCN** Porous coordination network Terphenyl-4,4"-dicarboxylic acid **TPDC TCPP** Tetrakis(4-carboxyphenyl)-porphyrin

TBP Tetrabenzoporphyrin or

5,10,15,20-tetra(p-benzoato)porphyrin H<sub>2</sub>DBBC 5,15-Di(p-benzoato)bacteriochlorin MRI Magnetic resonance imaging

**GSH** Glutathione

H<sub>4</sub>TBAPy 1,3,6,8-Tetrakis(p-benzoic acid)pyrene

DHA Dihydroartemisinin  $H_2BDC$ 2-Hydroxyterephthalic acid

PA

US

SNP

DTX

ART

CT

**RCM** 

TCPC

LMCT

**ICG** 

Ara

Fc(COOH)2

PDI

Chem Soc Rev **Review Article** 

Boron-dipyrromethene	PNIPAM	Poly(N-isopropylacrylamide)	
		Phosphate buffer solution	
		Polypyrrole	
=	-	Polyaniline	
		Cyclic arginine–glycine–aspartic acid	
		Heat shock protein	
		Phase-change material	
		Hyaluronic acid	
		(3-Glycidyloxypropyl)trimethoxysilane	
		Folic acid	
		Al(III) phthalocyanine chloride tetrasulfonic acid	
		2-Methylimidazole	
		Poly(ethylenimine)	
		Bis-(alkylthio) alkene	
		Imidazole-2-carboxaldehyde	
		2-((4'-(2,2-Bis(4-methoxyphenyl)-1-phenylvinyl)-	
	TFEDC	[1,1'-biphenyl]-4-yl)(phenyl)methylene)	
		malononitrile	
	TDETCE	( <i>E</i> )-2-(4-(4-(2,2-Bis(4-methoxyphenyl)-1-	
	IFEICE	phenylvinyl)styryl)-3-cyano-5,5-dimethylfuran-	
		2(5 <i>H</i> )-ylidene)malononitrile	
	AO AN		
		Banoxantrone	
1 0	TPAAQ	2-(4-(Diphenylamino)phenyl)anthracene-9,	
	DDMAEMA	10-dione	
		Poly(2-(diethylamino)ethylmethacrylate)	
	=	5,10,15,20-Tetrakis(4-pyridyl)-21 <i>H</i> ,23 <i>H</i> -porphine	
		Polylactic acid	
		Polyvinyl pyrrolidone	
		5,10,15,20-Tetrakis(4-aminophenyl)porphyrin	
		2,2'-Bipyridine-5.5'-dicarboxylic acid	
		Aluminum phthalocyanine	
		Polycaprolactone	
		NH <sub>2</sub> -poly(ethylene glycol) modified folic acid	
		Cetyltrimethylammonium bromide	
• • •		Escherichia coli	
*** *	S. aureus	Staphylococcus aureus	
	Conflic	ts of interest	
• • •	Confided of interest		
· ·	There are no	o conflicts to declare.	
	٠	ulo de o sociato	
Perfluoropentane	Acknowledgements		
	Boron-dipyrromethene Inductively coupled plasma-mass spectrometer 1,3,6,8-Tetrakis(p-benzoic acid)pyrene Highest occupied molecular orbital Lowest unoccupied molecular orbital 1,2-Bis(5-(4-carbonxyphenyl)-2-methylthien- 3-yl)cyclopent-1-ene Zeolitic imidazolate framework Universitetet i Oslo Materials Institute Lavoisier Tetrakis(1-methylpyridinium-4-yl)-porphyrin Zinc phthalocyanines Chlorine e6 1,3,5-Benzenetricarboxylic acid Cathepsin Doxorubicin Carbon dot Adenosine triphosphate Oxidized glutathione Polydopamine Polyethylene glycol Tirapazamine Piperlongumine Thioredoxin Thioredoxin reductase Glucose oxidase Peroxynitrite 1-Arginine Cytosine-phosphate-guanine Immunostimulatory cytokines type I Interferon Interleukin-6 T-lymphocyte-associated protein 4 Programmed cell death 1	Inductively coupled plasma-mass spectrometer  1,3,6,8-Tetrakis(p-benzoic acid)pyrene Highest occupied molecular orbital Lowest unoccupied molecular orbital 1,2-Bis(5-(4-carbonxyphenyl)-2-methylthien- 3-yl)cyclopent-1-ene Zeolitic imidazolate framework Universitetet i Oslo Materials Institute Lavoisier Tetrakis(1-methylpyridinium-4-yl)-porphyrin Zinc phthalocyanines Chlorine e6 1,3,5-Benzenetricarboxylic acid Cathepsin Doxorubicin Carbon dot Adenosine triphosphate Oxidized glutathione Polyethylene glycol Tirapazamine Polyethylene glycol Tirapazamine Polyethylene glycol Thioredoxin Thioredoxin Thioredoxin reductase Glucose oxidase Peroxynitrite 1-Arginine Cytosine-phosphate-guanine Immunostimulatory cytokines type I Interferon Interleukin-6 T-lymphocyte-associated protein 4 PCL Programmed cell death 1 Programmed	

## Acknowledgements

This work is jointly supported by the National Science Fund for Distinguished Young Scholars (no. 51925104), National Natural Science Foundation of China (no. 51871162, 51671081), Natural Science Fund of Hubei Province, (no. 2018CFA064), RGC/NSFC (N\_HKU725-1616), Hong Kong ITC (ITS/287/17, GHX/002/14SZ), as well as Health and Medical Research Fund (no. 03142446).

### References

- 1 D. E. J. G. J. Dolmans, D. Fukumura and R. K. Jain, Nat. Rev. Cancer, 2003, 3, 380-387.
- 2 G. Lan, K. Ni and W. Lin, Coord. Chem. Rev., 2019, 379, 65-81.

Cytarabine

Photoacoustic

Sodium nitroprusside

Computed tomography

1,1'-Ferrocenedicarboxylic acid

Ligand-to-metal charge transfer

Red cell membrane

Tetratopic porphyrin

Indocyanine green

Perylenediimide

Ultrasound

Docetaxel

Artemisinin

3 K. K. Ng and G. Zheng, Chem. Rev., 2015, 115, 11012-11042.

**Review Article** 

- 4 L. Cheng, C. Wang, L. Feng, K. Yang and Z. Liu, *Chem. Rev.*, 2014, **114**, 10869–10939.
- 5 M. Ethirajan, Y. Chen, P. Joshi and R. K. Pandey, *Chem. Soc. Rev.*, 2011, 40, 340–362.
- 6 P. Agostinis, K. Berg, K. A. Cengel, T. H. Foster, A. W. Girotti, S. O. Gollnick, S. M. Hahn, M. R. Hamblin, A. Juzeniene, D. Kessel, M. Korbelik, J. Moan, P. Mroz, D. Nowis, J. Piette, B. C. Wilson and J. Golab, *Ca-Cancer J. Clin.*, 2011, 61, 250–281.
- 7 A. P. Castano, T. N. Demidova and M. R. Hamblin, *Photo-diagn. Photodyn. Ther.*, 2004, 1, 279–293.
- 8 J. S. Dysart and M. S. Patterson, *Phys. Med. Biol.*, 2005, 50, 2597–2616.
- J. P. Celli, B. Q. Spring, I. Rizvi, C. L. Evans, K. S. Samkoe,
   S. Verma, B. W. Pogue and T. Hasan, *Chem. Rev.*, 2010, 110,
   2795–2838.
- 10 M. C. DeRosa and R. J. Crutchley, Coord. Chem. Rev., 2002, 233–234, 351–371.
- 11 X. Li, S. Kolemen, J. Yoon and E. U. Akkaya, Adv. Funct. Mater., 2017, 27, 1604053.
- 12 J. Ge, M. Lan, B. Zhou, W. Liu, L. Guo, H. Wang, Q. Jia, G. Niu, X. Huang, H. Zhou, X. Meng, P. Wang, C.-S. Lee, W. Zhang and X. Han, *Nat. Commun.*, 2014, 5, 4596.
- 13 L. Tan, J. Li, X. Liu, Z. Cui, X. Yang, K. W. K. Yeung, H. Pan, Y. Zheng, X. Wang and S. Wu, Small, 2018, 14, 1703197.
- 14 Q. Zhang, X. Liu, L. Tan, Z. Cui, Z. Li, Y. Liang, S. Zhu, K. W. K. Yeung, Y. Zheng and S. Wu, *Chem. Eng. J.*, 2020, 383, 123088.
- P. Yu, Y. Han, D. Han, X. Liu, Y. Liang, Z. Li, S. Zhu and S. Wu, J. Hazard. Mater., 2020, 390, 122126.
- 16 Y. Xiang, C. Mao, X. Liu, Z. Cui, D. Jing, X. Yang, Y. Liang, Z. Li, S. Zhu, Y. Zheng, K. W. K. Yeung, D. Zheng, X. Wang and S. Wu, *Small*, 2019, 15, 1900322.
- 17 Y. Li, X. Liu, L. Tan, Z. Cui, D. Jing, X. Yang, Y. Liang, Z. Li, S. Zhu, Y. Zheng, K. W. K. Yeung, D. Zheng, X. Wang and S. Wu, *Adv. Funct. Mater.*, 2019, 29, 1900946.
- 18 R. Long, Y. Li, L. Song and Y. Xiong, Small, 2015, 11, 3873-3889.
- 19 D. Jaque, L. Martínez Maestro, B. del Rosal, P. Haro-Gonzalez, A. Benayas, J. L. Plaza, E. Martín Rodríguez and J. García Solé, *Nanoscale*, 2014, 6, 9494–9530.
- 20 C. S. S. R. Kumar and F. Mohammad, Adv. Drug Delivery Rev., 2011, 63, 789–808.
- 21 J. Beik, Z. Abed, F. S. Ghoreishi, S. Hosseini-Nami, S. Mehrzadi, A. Shakeri-Zadeh and S. K. Kamrava, J. Controlled Release, 2016, 235, 205–221.
- 22 A. Hervault and N. T. K. Thanh, Nanoscale, 2014, 6, 11553-11573.
- 23 N. R. Datta, S. G. Ordóñez, U. S. Gaipl, M. M. Paulides, H. Crezee, J. Gellermann, D. Marder, E. Puric and S. Bodis, Cancer Treat. Rev., 2015, 41, 742–753.
- 24 X. Huang, P. K. Jain, I. H. El-Sayed and M. A. El-Sayed, *Lasers Med. Sci.*, 2007, 23, 217.
- 25 J. Zhou, M. Li, Y. Hou, Z. Luo, Q. Chen, H. Cao, R. Huo, C. Xue, L. Sutrisno, L. Hao, Y. Cao, H. Ran, L. Lu, K. Li and K. Cai, ACS Nano, 2018, 12, 2858–2872.

- 26 Y. Yang, W. Zhu, Z. Dong, Y. Chao, L. Xu, M. Chen and Z. Liu, Adv. Mater., 2017, 29, 1703588.
- 27 L. Tan, Z. Zhou, X. Liu, J. Li, Y. Zheng, Z. Cui, X. Yang, Y. Liang, Z. Li, X. Feng, S. Zhu, K. W. K. Yeung, C. Yang, X. Wang and S. Wu, *Adv. Sci.*, 2020, 7, 1902070.
- 28 D. Yoo, H. Jeong, S.-H. Noh, J.-H. Lee and J. Cheon, *Angew. Chem., Int. Ed.*, 2013, **52**, 13047–13051.
- 29 K. F. Chu and D. E. Dupuy, Nat. Rev. Cancer, 2014, 14, 199–208.
- 30 H. Y. Mao, S. Laurent, W. Chen, O. Akhavan, M. Imani, A. A. Ashkarran and M. Mahmoudi, *Chem. Rev.*, 2013, 113, 3407–3424.
- 31 L. Feng, L. Wu and X. Qu, Adv. Mater., 2013, 25, 168-186.
- 32 Y. Zou, Y. Zhang, Q. Yu and H. Chen, *Biomater. Sci.*, 2021, 9, 10–22.
- 33 B. Li, L. Tan, X. Liu, Z. Li, Z. Cui, Y. Liang, S. Zhu, X. Yang, K. W. Kwok Yeung and S. Wu, *J. Hazard. Mater.*, 2019, 380, 120818.
- 34 Y. Wang, T. Wei, Y. Qu, Y. Zhou, Y. Zheng, C. Huang, Y. Zhang, Q. Yu and H. Chen, ACS Appl. Mater. Interfaces, 2020, 12, 21283–21291.
- 35 Y. Qu, T. Wei, J. Zhao, S. Jiang, P. Yang, Q. Yu and H. Chen, J. Mater. Chem. B, 2018, 6, 3946–3955.
- 36 H. S. Jung, P. Verwilst, A. Sharma, J. Shin, J. L. Sessler and J. S. Kim, *Chem. Soc. Rev.*, 2018, 47, 2280–2297.
- 37 T. Wei, Q. Yu and H. Chen, Adv. Healthcare Mater., 2019, 8, 1801381.
- 38 C. Mao, Y. Xiang, X. Liu, Y. Zheng, K. W. K. Yeung, Z. Cui, X. Yang, Z. Li, Y. Liang, S. Zhu and S. Wu, ACS Appl. Mater. Interfaces, 2019, 11, 17902–17914.
- 39 X. Chen, M. Zhang, S. Li, L. Li, L. Zhang, T. Wang, M. Yu, Z. Mou and C. Wang, J. Mater. Chem. B, 2017, 5, 1772–1778.
- 40 X. Wang, K. Su, L. Tan, X. Liu, Z. Cui, D. Jing, X. Yang, Y. Liang, Z. Li, S. Zhu, K. W. K. Yeung, D. Zheng and S. Wu, ACS Appl. Mater. Interfaces, 2019, 11, 15014–15027.
- 41 L. Jiao, J. Y. R. Seow, W. S. Skinner, Z. U. Wang and H.-L. Jiang, *Mater. Today*, 2019, 27, 43–68.
- 42 S. Kitagawa, R. Kitaura and S.-i. Noro, *Angew. Chem., Int. Ed.*, 2004, **43**, 2334–2375.
- 43 A. Kirchon, L. Feng, H. F. Drake, E. A. Joseph and H.-C. Zhou, *Chem. Soc. Rev.*, 2018, 47, 8611–8638.
- 44 T. Simon-Yarza, A. Mielcarek, P. Couvreur and C. Serre, *Adv. Mater.*, 2018, **30**, 1707365.
- 45 M.-X. Wu and Y.-W. Yang, Adv. Mater., 2017, 29, 1606134.
- 46 W.-P. Li, C.-H. Su, L.-C. Tsao, C.-T. Chang, Y.-P. Hsu and C.-S. Yeh, ACS Nano, 2016, 10, 11027–11036.
- 47 K. Lu, C. He and W. Lin, J. Am. Chem. Soc., 2015, 137, 7600-7603.
- 48 Y. Zhang, F. Wang, C. Liu, Z. Wang, L. Kang, Y. Huang, K. Dong, J. Ren and X. Qu, ACS Nano, 2018, 12, 651–661.
- 49 B. Lü, Y. Chen, P. Li, B. Wang, K. Müllen and M. Yin, *Nat. Commun.*, 2019, **10**, 767.
- 50 F. Hu, D. Mao, Kenry, Y. Wang, W. Wu, D. Zhao, D. Kong and B. Liu, *Adv. Funct. Mater.*, 2018, **28**, 1707519.
- 51 H. Wang, Y. Chen, H. Wang, X. Liu, X. Zhou and F. Wang, Angew. Chem., Int. Ed., 2019, 58, 7380–7384.

- 52 X. Deng, S. Liang, X. Cai, S. Huang, Z. Cheng, Y. Shi, M. Pang, P. A. Ma and J. Lin, Nano Lett., 2019, 19, 6772-6780.
- 53 D. Wang, H. Wu, J. Zhou, P. Xu, C. Wang, R. Shi, H. Wang, H. Wang, Z. Guo and Q. Chen, Adv. Sci., 2018, 5, 1800287.
- 54 J. Li, X. Liu, L. Tan, Z. Cui, X. Yang, Y. Liang, Z. Li, S. Zhu, Y. Zheng, K. W. K. Yeung, X. Wang and S. Wu, Nat. Commun., 2019, 10, 4490.
- 55 K. Lu, C. He and W. Lin, J. Am. Chem. Soc., 2014, 136, 16712-16715.
- 56 Z. Yu, W. Hu, H. Zhao, X. Miao, Y. Guan, W. Cai, Z. Zeng, Q. Fan and T. T. Y. Tan, Angew. Chem., Int. Ed., 2019, 58, 8536-8540.
- 57 S.-Y. Yin, G. Song, Y. Yang, Y. Zhao, P. Wang, L.-M. Zhu, X. Yin and X.-B. Zhang, Adv. Funct. Mater., 2019, 29, 1901417.
- 58 J. Park, Q. Jiang, D. Feng, L. Mao and H.-C. Zhou, J. Am. Chem. Soc., 2016, 138, 3518-3525.
- 59 H. Guo, S. Yi, K. Feng, Y. Xia, X. Qu, F. Wan, L. Chen and C. Zhang, Chem. Eng. J., 2021, 403, 126432.
- 60 H. Min, J. Wang, Y. Qi, Y. Zhang, X. Han, Y. Xu, J. Xu, Y. Li, L. Chen, K. Cheng, G. Liu, N. Yang, Y. Li and G. Nie, Adv. Mater., 2019, 31, 1808200.
- 61 Q. Cheng, W. Yu, J. Ye, M. Liu, W. Liu, C. Zhang, C. Zhang, J. Feng and X.-Z. Zhang, *Biomaterials*, 2019, 224, 119500.
- 62 S.-Y. Li, H. Cheng, B.-R. Xie, W.-X. Qiu, J.-Y. Zeng, C.-X. Li, S.-S. Wan, L. Zhang, W.-L. Liu and X.-Z. Zhang, ACS Nano, 2017, 11, 7006-7018.
- 63 C. Liu, J. Xing, O. U. Akakuru, L. Luo, S. Sun, R. Zou, Z. Yu, Q. Fang and A. Wu, Nano Lett., 2019, 19, 5674-5682.
- 64 Q. Guan, L.-L. Zhou, Y.-A. Li and Y.-B. Dong, Chem. Commun., 2019, 55, 14898-14901.
- 65 J. Mu, L. He, W. Fan, W. Tang, Z. Wang, C. Jiang, D. Zhang, Y. Liu, H. Deng, J. Zou, O. Jacobson, J. Qu, P. Huang and X. Chen, Small, 2020, 16, 2004016.
- 66 H. Zhang, Q. Li, R. Liu, X. Zhang, Z. Li and Y. Luan, Adv. Funct. Mater., 2018, 28, 1802830.
- 67 M. Lismont, L. Dreesen and S. Wuttke, Adv. Funct. Mater., 2017, 27, 1606314.
- 68 A. Gellé, T. Jin, L. de la Garza, G. D. Price, L. V. Besteiro and A. Moores, Chem. Rev., 2020, 120, 986-1041.
- 69 J. Wang, Y. Li, L. Deng, N. Wei, Y. Weng, S. Dong, D. Qi, J. Qiu, X. Chen and T. Wu, Adv. Mater., 2017, 29, 1603730.
- 70 Y. Cheng, Y. Chang, Y. Feng, H. Jian, Z. Tang and H. Zhang, Angew. Chem., Int. Ed., 2018, 130, 252–257.
- 71 C. M. Marian, Wiley Interdiscip. Rev.: Comput. Mol. Sci., 2012, 2, 187-203.
- 72 J. Yao, M. Yang and Y. Duan, Chem. Rev., 2014, 114, 6130-6178.
- 73 J. F. Lovell, T. W. B. Liu, J. Chen and G. Zheng, Chem. Rev., 2010, 110, 2839-2857.
- 74 S. Mai, P. Marquetand and L. González, Int. J. Quantum Chem., 2015, 115, 1215-1231.
- 75 A. Juarranz, P. Jaén, F. Sanz-Rodríguez, J. Cuevas and S. González, Clin. Transl. Oncol., 2008, 10, 148-154.
- 76 W. M. Sharman, C. M. Allen and J. E. van Lier, Drug Discovery Today, 1999, 4, 507-517.

- 77 S. Kwiatkowski, B. Knap, D. Przystupski, J. Saczko, E. Kędzierska, K. Knap-Czop, J. Kotlińska, O. Michel, K. Kotowski and J. Kulbacka, Biomed. Pharmacother., 2018, 106, 1098-1107.
- 78 D. Van Straten, V. Mashayekhi, H. S. De Bruijn, S. Oliveira and D. J. Robinson, *Cancers*, 2017, **9**, 19.
- 79 C. A. Robertson, D. H. Evans and H. Abrahamse, J. Photochem. Photobiol., B, 2009, 96, 1-8.
- 80 Y. Liu, P. Bhattarai, Z. Dai and X. Chen, Chem. Soc. Rev., 2019, 48, 2053-2108.
- 81 G. Hong, S. Diao, A. L. Antaris and H. Dai, Chem. Rev., 2015, 115, 10816-10906.
- 82 P. K. Jain, X. Huang, I. H. El-Sayed and M. A. El-Sayed, Acc. Chem. Res., 2008, 41, 1578-1586.
- 83 J. M. Luther, P. K. Jain, T. Ewers and A. P. Alivisatos, Nat. Mater., 2011, 10, 361-366.
- 84 D. Choi, B. Yoon, D.-K. Kim, H. Baik, J.-H. Choi and K. S. Jeong, Chem. Mater., 2017, 29, 8548-8554.
- 85 J. Li, X. Liu, L. Tan, Y. Liang, Z. Cui, X. Yang, S. Zhu, Z. Li, Y. Zheng, K. W. K. Yeung, X. Wang and S. Wu, Small Methods, 2019, 3, 1900048.
- 86 X. Wang, H. Li, F. Li, X. Han and G. Chen, Nanoscale, 2019, 11, 22079-22088.
- 87 C. Liu, B. Liu, J. Zhao, Z. Di, D. Chen, Z. Gu, L. Li and Y. Zhao, Angew. Chem., Int. Ed., 2020, 59, 2634-2638.
- 88 Y. Shao, B. Liu, Z. Di, G. Zhang, L.-D. Sun, L. Li and C.-H. Yan, J. Am. Chem. Soc., 2020, 142, 3939-3946.
- 89 L. He, O. Ni, J. Mu, W. Fan, L. Liu, Z. Wang, L. Li, W. Tang, Y. Liu, Y. Cheng, L. Tang, Z. Yang, Y. Liu, J. Zou, W. Yang, O. Jacobson, F. Zhang, P. Huang and X. Chen, J. Am. Chem. Soc., 2020, 142, 6822-6832.
- 90 V. J. Pansare, S. Hejazi, W. J. Faenza and R. K. Prud'homme, Chem. Mater., 2012, 24, 812-827.
- 91 C. Gao, J. Wang, H. Xu and Y. Xiong, Chem. Soc. Rev., 2017, 46, 2799-2823.
- 92 S. Li, S. Zhou, Y. Li, X. Li, J. Zhu, L. Fan and S. Yang, ACS Appl. Mater. Interfaces, 2017, 9, 22332-22341.
- 93 Y. Yang, J. Liu, C. Liang, L. Feng, T. Fu, Z. Dong, Y. Chao, Y. Li, G. Lu, M. Chen and Z. Liu, ACS Nano, 2016, 10, 2774–2781.
- 94 M. Zheng, P. Zhao, Z. Luo, P. Gong, C. Zheng, P. Zhang, C. Yue, D. Gao, Y. Ma and L. Cai, ACS Appl. Mater. Interfaces, 2014, 6, 6709-6716.
- 95 E. Caballero-Mancebo, B. Cohen, S. Smolders, D. E. De Vos and A. Douhal, Adv. Sci., 2019, 6, 1901020.
- 96 L. He, M. Brasino, C. Mao, S. Cho, W. Park, A. P. Goodwin and J. N. Cha, Small, 2017, 13, 1700504.
- 97 K. Lu, C. He, N. Guo, C. Chan, K. Ni, R. R. Weichselbaum and W. Lin, J. Am. Chem. Soc., 2016, 138, 12502-12510.
- 98 X. Huang, I. H. El-Sayed, W. Qian and M. A. El-Sayed, J. Am. Chem. Soc., 2006, 128, 2115-2120.
- 99 Q. Yang, Q. Xu, S.-H. Yu and H.-L. Jiang, Angew. Chem., Int. Ed., 2016, 55, 3685-3689.
- 100 G. Fu, W. Liu, S. Feng and X. Yue, Chem. Commun., 2012, 48, 11567-11569.
- 101 Y. Zhou, Q. Bao, L. A. L. Tang, Y. Zhong and K. P. Loh, Chem. Mater., 2009, 21, 2950-2956.

Review Article Chem Soc Rev

- 102 K. Yang, H. Xu, L. Cheng, C. Sun, J. Wang and Z. Liu, Adv. Mater., 2012, 24, 5586–5592.
- 103 Z. Deng, C. Fang, X. Ma, X. Li, Y.-J. Zeng and X. Peng, *ACS Appl. Mater. Interfaces*, 2020, **12**, 20321–20330.
- 104 G. Zhou, Y. S. Wang, Z. Jin, P. Zhao, H. Zhang, Y. Wen and Q. He, *Nanoscale Horiz.*, 2019, 4, 1185–1193.
- 105 S.-S. Wan, Q. Cheng, X. Zeng and X.-Z. Zhang, ACS Nano, 2019, 13, 6561–6571.
- 106 Y. Ma, X. Li, A. Li, P. Yang, C. Zhang and B. Tang, Angew. Chem., Int. Ed., 2017, 56, 13752–13756.
- 107 J.-Y. Zeng, M.-Z. Zou, M. Zhang, X.-S. Wang, X. Zeng, H. Cong and X.-Z. Zhang, ACS Nano, 2018, 12, 4630–4640.
- 108 K. Zhang, Z. Yu, X. Meng, W. Zhao, Z. Shi, Z. Yang, H. Dong and X. Zhang, *Adv. Sci.*, 2019, **6**, 1900530.
- 109 C. He, D. Liu and W. Lin, *Chem. Rev.*, 2015, **115**, 11079–11108.
- 110 X.-S. Wang, J.-Y. Zeng, M.-K. Zhang, X. Zeng and X.-Z. Zhang, *Adv. Funct. Mater.*, 2018, **28**, 1801783.
- 111 S.-Y. Li, H. Cheng, W.-X. Qiu, L. Zhang, S.-S. Wan, J.-Y. Zeng and X.-Z. Zhang, *Biomaterials*, 2017, 142, 149–161.
- 112 S.-S. Wan, J.-Y. Zeng, H. Cheng and X.-Z. Zhang, *Biomaterials*, 2018, **185**, 51–62.
- 113 Y. Zhang, P. Sun, L. Zhang, Z. Wang, F. Wang, K. Dong, Z. Liu, J. Ren and X. Qu, *Adv. Funct. Mater.*, 2019, 29, 1808594.
- 114 H. Qiu, F. Pu, Z. Liu, Q. Deng, P. Sun, J. Ren and X. Qu, *Small*, 2019, **15**, 1902522.
- 115 K. Kim, S. Lee, E. Jin, L. Palanikumar, J. H. Lee, J. C. Kim, J. S. Nam, B. Jana, T.-H. Kwon, S. K. Kwak, W. Choe and J.-H. Ryu, ACS Appl. Mater. Interfaces, 2019, 11, 27512–27520.
- 116 H. Wang, D. Yu, J. Fang, C. Cao, Z. Liu, J. Ren and X. Qu, *ACS Nano*, 2019, **13**, 9206–9217.
- 117 M. Liu, L. Wang, X. Zheng and Z. Xie, *ACS Appl. Mater. Interfaces*, 2017, **9**, 41512–41520.
- 118 J. Hu, W. Wu, Y. Qin, C. Liu, P. Wei, J. Hu, P. H. Seeberger and J. Yin, *Adv. Funct. Mater.*, 2020, **30**, 1910084.
- 119 Z.-X. Chen, M.-D. Liu, M.-K. Zhang, S.-B. Wang, L. Xu, C.-X. Li, F. Gao, B.-R. Xie, Z.-L. Zhong and X.-Z. Zhang, *Adv. Funct. Mater.*, 2018, **28**, 1803498.
- 120 Q.-g. Zhao, J. Wang, Y.-p. Zhang, J. Zhang, A.-n. Tang and D.-m. Kong, *J. Mater. Chem. B*, 2018, **6**, 7898–7907.
- 121 X.-T. Tian, P.-P. Cao, H. Zhang, Y.-H. Li and X.-B. Yin, *Chem. Commun.*, 2019, 55, 6241–6244.
- 122 D. Zhang, Z. Ye, L. Wei, H. Luo and L. Xiao, ACS Appl. Mater. Interfaces, 2019, 11, 39594–39602.
- 123 Z. Cai, F. Xin, Z. Wei, M. Wu, X. Lin, X. Du, G. Chen, D. Zhang, Z. Zhang, X. Liu and C. Yao, *Adv. Healthcare Mater.*, 2020, **9**, 1900996.
- 124 S.-Y. Li, B.-R. Xie, H. Cheng, C.-X. Li, M.-K. Zhang, W.-X. Qiu, W.-L. Liu, X.-S. Wang and X.-Z. Zhang, *Biomaterials*, 2018, **151**, 1–12.
- 125 M. He, Y. Chen, C. Tao, Q. Tian, L. An, J. Lin, Q. Tian, H. Yang and S. Yang, ACS Appl. Mater. Interfaces, 2019, 11, 41946–41956.
- 126 T. Luo, K. Ni, A. Culbert, G. Lan, Z. Li, X. Jiang, M. Kaufmann and W. Lin, *J. Am. Chem. Soc.*, 2020, **142**, 7334–7339.
- 127 J. Liu, Y. Yang, W. Zhu, X. Yi, Z. Dong, X. Xu, M. Chen, K. Yang, G. Lu, L. Jiang and Z. Liu, *Biomaterials*, 2016, 97, 1–9.

- 128 W. Zhang, J. Lu, X. Gao, P. Li, W. Zhang, Y. Ma, H. Wang and B. Tang, *Angew. Chem., Int. Ed.*, 2018, 57, 4891–4896.
- 129 M. Liu, L. Wang, X. Zheng, S. Liu and Z. Xie, ACS Appl. Mater. Interfaces, 2018, 10, 24638–24647.
- 130 Y. Zhao, Y. Kuang, M. Liu, J. Wang and R. Pei, *Chem. Mater.*, 2018, 30, 7511–7520.
- 131 W. Zhu, L. Zhang, Z. Yang, P. Liu, J. Wang, J. Cao, A. Shen, Z. Xu and J. Wang, *Chem. Eng. J.*, 2019, 358, 969–979.
- 132 Q. Deng, P. Sun, L. Zhang, Z. Liu, H. Wang, J. Ren and X. Qu, Adv. Funct. Mater., 2019, 29, 1903018.
- 133 P. Ling, C. Qian, J. Yu and F. Gao, *Chem. Commun.*, 2019, 55, 6385–6388.
- 134 W. Zhu, Y. Yang, Q. Jin, Y. Chao, L. Tian, J. Liu, Z. Dong and Z. Liu, *Nano Res.*, 2019, 12, 1307–1312.
- 135 Y. Zhao, X. Cai, Y. Zhang, C. Chen, J. Wang and R. Pei, *Nanoscale*, 2019, **11**, 12250–12258.
- 136 X. Wan, H. Zhong, W. Pan, Y. Li, Y. Chen, N. Li and B. Tang, *Angew. Chem.*, *Int. Ed.*, 2019, **58**, 14134–14139.
- 137 J. Lu, L. Yang, W. Zhang, P. Li, X. Gao, W. Zhang, H. Wang and B. Tang, *Chem. Commun.*, 2019, 55, 10792–10795.
- 138 Z. Gao, Y. Li, Y. Zhang, K. Cheng, P. An, F. Chen, J. Chen, C. You, Q. Zhu and B. Sun, *ACS Appl. Mater. Interfaces*, 2020, 12, 1963–1972.
- 139 K. Ni, T. Luo, G. Lan, A. Culbert, Y. Song, T. Wu, X. Jiang and W. Lin, *Angew. Chem., Int. Ed.*, 2020, **59**, 1108–1112.
- 140 Y. Zhao, J. Wang, X. Cai, P. Ding, H. Lv and R. Pei, *ACS Appl. Mater. Interfaces*, 2020, **12**, 23697–23706.
- 141 W. Zhu, Y. Liu, Z. Yang, L. Zhang, L. Xiao, P. Liu, J. Wang, C. Yi, Z. Xu and J. Ren, J. Mater. Chem. B, 2018, 6, 265–276.
- 142 J.-Y. Zeng, M.-K. Zhang, M.-Y. Peng, D. Gong and X.-Z. Zhang, *Adv. Funct. Mater.*, 2018, **28**, 1705451.
- 143 X. Hu, Y. Lu, L. Zhou, L. Chen, T. Yao, S. Liang, J. Han, C. Dong and S. Shi, J. Mater. Chem. B, 2020, 8, 935–944.
- 144 B. Li, X. Wang, L. Chen, Y. Zhou, W. Dang, J. Chang and C. Wu, *Theranostics*, 2018, **8**, 4086.
- 145 K. Zhang, X. Meng, Y. Cao, Z. Yang, H. Dong, Y. Zhang, H. Lu, Z. Shi and X. Zhang, *Adv. Funct. Mater.*, 2018, 28, 1804634.
- D. Han, Y. Han, J. Li, X. Liu, K. W. K. Yeung, Y. Zheng,
  Z. Cui, X. Yang, Y. Liang, Z. Li, S. Zhu, X. Yuan, X. Feng,
  C. Yang and S. Wu, *Appl. Catal.*, B, 2020, 261, 118248.
- 147 S. J. Thompson, M. R. Brennan, S. Y. Lee and G. Dong, *Chem. Soc. Rev.*, 2018, 47, 929–981.
- 148 X. Cai, Z. Xie, B. Ding, S. Shao, S. Liang, M. Pang and J. Lin, *Adv. Sci.*, 2019, **6**, 1900848.
- 149 W. Wang, L. Wang, Z. Li and Z. Xie, Chem. Commun., 2016, 52, 5402–5405.
- 150 X. Zhao, Z. Zhang, X. Cai, B. Ding, C. Sun, G. Liu, C. Hu, S. Shao and M. Pang, ACS Appl. Mater. Interfaces, 2019, 11, 7884–7892.
- 151 J. Park, Q. Jiang, D. Feng and H.-C. Zhou, *Angew. Chem., Int. Ed.*, 2016, 55, 7188-7193.
- 152 L. Zhang, J. Lei, F. Ma, P. Ling, J. Liu and H. Ju, *Chem. Commun.*, 2015, **51**, 10831–10834.
- 153 R. Chen, J. Zhang, Y. Wang, X. Chen, J. A. Zapien and C.-S. Lee, *Nanoscale*, 2015, 7, 17299–17305.

154 H. Cheng, J.-Y. Zhu, S.-Y. Li, J.-Y. Zeng, Q. Lei, K.-W. Chen, C. Zhang and X.-Z. Zhang, *Adv. Funct. Mater.*, 2016, 26, 7847–7860.

Chem Soc Rev

- 155 J. Liu, L. Zhang, J. Lei, H. Shen and H. Ju, *ACS Appl. Mater. Interfaces*, 2017, **9**, 2150–2158.
- 156 D. Yang, G. Yang, S. Gai, F. He, C. Li and P. Yang, *ACS Appl. Mater. Interfaces*, 2017, **9**, 6829–6838.
- H.-J. Cai, T.-T. Shen, J. Zhang, C.-F. Shan, J.-G. Jia, X. Li, W.-S. Liu and Y. Tang, J. Mater. Chem. B, 2017, 5, 2390–2394.
- 158 F. Nian, Y. Huang, M. Song, J.-J. Chen and J. Xue, *J. Mater. Chem. B*, 2017, 5, 6227–6232.
- 159 S. Sharma, K. Sethi and I. Roy, New J. Chem., 2017, 41, 11860–11866.
- 160 J. Liu, G. Yang, W. Zhu, Z. Dong, Y. Yang, Y. Chao and Z. Liu, *Biomaterials*, 2017, 146, 40–48.
- 161 Q. Guan, L.-L. Zhou, Y.-A. Li and Y.-B. Dong, *Inorg. Chem.*, 2018, 57, 10137–10145.
- 162 M.-R. Song, D.-Y. Li, F.-Y. Nian, J.-P. Xue and J.-J. Chen, J. Mater. Sci., 2018, 53, 2351–2361.
- 163 D. Xu, Y. You, F. Zeng, Y. Wang, C. Liang, H. Feng and X. Ma, ACS Appl. Mater. Interfaces, 2018, 10, 15517–15523.
- 164 G. Hu, L. Yang, Y. Li and L. Wang, J. Mater. Chem. B, 2018,6, 7936–7942.
- 165 Z. Xie, X. Cai, C. Sun, S. Liang, S. Shao, S. Huang, Z. Cheng, M. Pang, B. Xing, A. A. A. Kheraif and J. Lin, *Chem. Mater.*, 2019, 31, 483–490.
- 166 Z. He, Y. Dai, X. Li, D. Guo, Y. Liu, X. Huang, J. Jiang, S. Wang, G. Zhu, F. Zhang, L. Lin, J.-J. Zhu, G. Yu and X. Chen, Small, 2019, 15, 1804131.
- 167 Q. Sun, H. Bi, Z. Wang, C. Li, C. Wang, J. Xu, D. Yang, F. He, S. Gai and P. Yang, ACS Appl. Mater. Interfaces, 2019, 11, 36347–36358.
- 168 Y. Wang, W. Wu, J. Liu, P. N. Manghnani, F. Hu, D. Ma, C. Teh, B. Wang and B. Liu, ACS Nano, 2019, 13, 6879–6890.
- 169 Y. Wang, W. Wu, D. Mao, C. Teh, B. Wang and B. Liu, Adv. Funct. Mater., 2020, 30, 2002431.
- 170 Y.-C. Ma, Y.-H. Zhu, X.-F. Tang, L.-F. Hang, W. Jiang, M. Li,
  M. I. Khan, Y.-Z. You and Y.-C. Wang, *Biomater. Sci.*, 2019,
  7, 2740–2748.
- 171 Z. Xie, S. Liang, X. Cai, B. Ding, S. Huang, Z. Hou, P. a. Ma, Z. Cheng and J. Lin, *ACS Appl. Mater. Interfaces*, 2019, 11, 31671–31680.
- 172 Y.-T. Qin, H. Peng, X.-W. He, W.-Y. Li and Y.-K. Zhang, *ACS Appl. Mater. Interfaces*, 2019, **11**, 34268–34281.
- 173 C. Wang, X. Jia, W. Zhen, M. Zhang and X. Jiang, *ACS Biomater. Sci. Eng.*, 2019, 5, 4435–4441.
- 174 J. Feng, W. Yu, Z. Xu and F. Wang, *Chem. Sci.*, 2020, 11, 1649–1656.
- 175 Y. You, D. Xu, X. Pan and X. Ma, *Appl. Mater. Today*, 2019, **16**, 508–517.
- 176 P. Liu, X. Xie, X. Shi, Y. Peng, J. Ding and W. Zhou, *ACS Appl. Mater. Interfaces*, 2019, **11**, 48261–48270.
- 177 H. Chen, J. Yang, L. Sun, H. Zhang, Y. Guo, J. Qu, W. Jiang, W. Chen, J. Ji, Y.-W. Yang and B. Wang, *Small*, 2019, 15, 1903880.

- 178 X. Fu, Z. Yang, T. Deng, J. Chen, Y. Wen, X. Fu, L. Zhou, Z. Zhu and C. Yu, *J. Mater. Chem. B*, 2020, **8**, 1481–1488.
- 179 R. Chen, J. Zhang, J. Chelora, Y. Xiong, S. V. Kershaw, K. F. Li, P.-K. Lo, K. W. Cheah, A. L. Rogach, J. A. Zapien and C.-S. Lee, ACS Appl. Mater. Interfaces, 2017, 9, 5699–5708.
- 180 W. Zhang, B. Li, H. Ma, L. Zhang, Y. Guan, Y. Zhang, X. Zhang, P. Jing and S. Yue, *ACS Appl. Mater. Interfaces*, 2016, 8, 21465–21471.
- 181 D. Yang, G. Yang, S. Gai, F. He, G. An, Y. Dai, R. Lv and P. Yang, *Nanoscale*, 2015, 7, 19568–19578.
- 182 Y. Wang, X. Pang, J. Wang, Y. Cheng, Y. Song, Q. Sun, Q. You, F. Tan, J. Li and N. Li, J. Mater. Chem. B, 2018, 6, 2460-2473.
- 183 C. Liu, L. Luo, L. Zeng, J. Xing, Y. Xia, S. Sun, L. Zhang, Z. Yu, J. Yao, Z. Yu, O. U. Akakuru, M. Saeed and A. Wu, Small, 2018, 14, 1801851.
- 184 S. Gao, P. Zheng, Z. Li, X. Feng, W. Yan, S. Chen, W. Guo, D. Liu, X. Yang, S. Wang, X.-J. Liang and J. Zhang, *Biomaterials*, 2018, **178**, 83–94.
- 185 P. Yang, Y. Men, Y. Tian, Y. Cao, L. Zhang, X. Yao and W. Yang, ACS Appl. Mater. Interfaces, 2019, 11, 11209–11219.
- 186 J. Liu, T. Liu, P. Du, L. Zhang and J. Lei, *Angew. Chem., Int. Ed.*, 2019, **58**, 7808–7812.
- 187 R. Chen, W.-C. Chen, L. Yan, S. Tian, B. Liu, X. Chen, C.-S. Lee and W. Zhang, J. Mater. Chem. B, 2019, 7, 4763–4770.
- 188 Y. Wang, J. Yan, N. Wen, H. Xiong, S. Cai, Q. He, Y. Hu, D. Peng, Z. Liu and Y. Liu, *Biomaterials*, 2020, 230, 119619.
- 189 K. K. Tanabe and S. M. Cohen, *Chem. Soc. Rev.*, 2011, **40**, 498–519.
- 190 S. Wang, C. M. McGuirk, A. d'Aquino, J. A. Mason and C. A. Mirkin, *Adv. Mater.*, 2018, **30**, 1800202.
- 191 A. Pandey, N. Dhas, P. Deshmukh, C. Caro, P. Patil, M. Luisa García-Martín, B. Padya, A. Nikam, T. Mehta and S. Mutalik, Coord. Chem. Rev., 2020, 409, 213212.
- 192 A. Zimpel, T. Preiß, R. Röder, H. Engelke, M. Ingrisch, M. Peller, J. O. Rädler, E. Wagner, T. Bein, U. Lächelt and S. Wuttke, *Chem. Mater.*, 2016, 28, 3318–3326.
- 193 K. Lu, T. Aung, N. Guo, R. Weichselbaum and W. Lin, *Adv. Mater.*, 2018, **30**, 1707634.
- 194 D. Luo, K. A. Carter, D. Miranda and J. F. Lovell, Adv. Sci., 2017, 4, 1600106.
- 195 E. B. Rankin and A. J. Giaccia, Science, 2016, 352, 175-180.
- 196 R. Mo and Z. Gu, Mater. Today, 2016, 19, 274-283.
- 197 X. Zhong, X. Wang, L. Cheng, Y. Tang, G. Zhan, F. Gong, R. Zhang, J. Hu, Z. Liu and X. Yang, *Adv. Funct. Mater.*, 2020, 30, 1907954.
- 198 Q. Chen, J. Zhou, Z. Chen, Q. Luo, J. Xu and G. Song, *ACS Appl. Mater. Interfaces*, 2019, **11**, 30551–30565.
- 199 Z. Wang, B. Liu, Q. Sun, S. Dong, Y. Kuang, Y. Dong, F. He, S. Gai and P. Yang, ACS Appl. Mater. Interfaces, 2020, 12, 17254–17267.
- 200 H. Ranji-Burachaloo, P. A. Gurr, D. E. Dunstan and G. G. Qiao, *ACS Nano*, 2018, **12**, 11819–11837.
- 201 Y. Liu, C. S. Gong, L. Lin, Z. Zhou, Y. Liu, Z. Yang, Z. Shen, G. Yu, Z. Wang, S. Wang, Y. Ma, W. Fan, L. He, G. Niu, Y. Dai and X. Chen, *Theranostics*, 2019, 9, 2791–2799.

Review Article Chem Soc Rev

- 202 D. Wang, H. Wu, W. Q. Lim, S. Z. F. Phua, P. Xu, Q. Chen, Z. Guo and Y. Zhao, Adv. Mater., 2019, 31, 1901893.
- 203 X. Meng, J. Deng, F. Liu, T. Guo, M. Liu, P. Dai, A. Fan, Z. Wang and Y. Zhao, *Nano Lett.*, 2019, 19, 7866–7876.
- 204 A. K. Iyer, G. Khaled, J. Fang and H. Maeda, *Drug Discovery Today*, 2006, **11**, 812–818.
- 205 H. Kobayashi, R. Watanabe and P. L. Choyke, *Theranostics*, 2014, 4, 81–89.
- 206 M. Yu and J. Zheng, ACS Nano, 2015, 9, 6655-6674.
- 207 J. Fang, H. Nakamura and H. Maeda, *Adv. Drug Delivery Rev.*, 2011, **63**, 136–151.
- 208 H. Soo Choi, W. Liu, P. Misra, E. Tanaka, J. P. Zimmer, B. Itty Ipe, M. G. Bawendi and J. V. Frangioni, *Nat. Biotechnol.*, 2007, 25, 1165–1170.
- 209 J. Zhou, G. Yu and F. Huang, Chem. Soc. Rev., 2017, 46, 7021-7053.
- 210 J. Zhang, X. Li, X. Han, R. Liu and J. Fang, *Trends Pharmacol. Sci.*, 2017, 38, 794–808.
- 211 B. Yang, Y. Chen and J. Shi, Adv. Mater., 2019, 31, 1901778.
- 212 W. Fan, N. Lu, P. Huang, Y. Liu, Z. Yang, S. Wang, G. Yu, Y. Liu, J. Hu, Q. He, J. Qu, T. Wang and X. Chen, *Angew. Chem., Int. Ed.*, 2017, 56, 1229–1233.
- 213 L. Chen, S.-F. Zhou, L. Su and J. Song, ACS Nano, 2019, 13, 10887–10917.
- 214 Y. Li, X. Liu, B. Li, Y. Zheng, Y. Han, D.-f. Chen, K. W. K. Yeung, Z. Cui, Y. Liang, Z. Li, S. Zhu, X. Wang and S. Wu, ACS Nano, 2020, 14, 8157–8170.
- 215 J. D. Martin, H. Cabral, T. Stylianopoulos and R. K. Jain, Nat. Rev. Clin. Oncol., 2020, 17, 251–266.
- 216 X. Duan, C. Chan and W. Lin, *Angew. Chem., Int. Ed.*, 2019, **58**, 670–680.
- 217 L. A. Emens, P. A. Ascierto, P. K. Darcy, S. Demaria, A. M. M. Eggermont, W. L. Redmond, B. Seliger and F. M. Marincola, *Eur. J. Cancer*, 2017, **81**, 116–129.
- 218 X. Li, C. Shao, Y. Shi and W. Han, J. Hematol. Oncol., 2018, 11, 31.
- 219 L. Guo, D. D. Yan, D. Yang, Y. Li, X. Wang, O. Zalewski, B. Yan and W. Lu, ACS Nano, 2014, 8, 5670–5681.
- 220 H. Zhang, J. Zhang, Q. Li, A. Song, H. Tian, J. Wang, Z. Li and Y. Luan, *Biomaterials*, 2020, **245**, 119983.
- 221 J. Liu, S. J. Blake, M. C. R. Yong, H. Harjunpää, S. F. Ngiow, K. Takeda, A. Young, J. S. O'Donnell, S. Allen, M. J. Smyth and M. W. L. Teng, *Cancer Discovery*, 2016, 6, 1382–1399.
- 222 S. S. Lucky, K. C. Soo and Y. Zhang, *Chem. Rev.*, 2015, **115**, 1990–2042.
- 223 J. Schmitt, V. Heitz, A. Sour, F. Bolze, H. Ftouni, J.-F. Nicoud, L. Flamigni and B. Ventura, *Angew. Chem., Int. Ed.*, 2015, **54**, 169–173.
- 224 S. Han, R. Deng, X. Xie and X. Liu, *Angew. Chem., Int. Ed.*, 2014, **53**, 11702–11715.
- 225 Z. Gu, L. Yan, G. Tian, S. Li, Z. Chai and Y. Zhao, Adv. Mater., 2013, 25, 3758–3779.
- 226 X. Chen, D. Peng, Q. Ju and F. Wang, *Chem. Soc. Rev.*, 2015, 44, 1318–1330.
- 227 X. Jia, J. Li and E. Wang, Nanoscale, 2012, 4, 5572-5575.
- 228 J. Shen, Y. Zhu, C. Chen, X. Yang and C. Li, *Chem. Commun.*, 2011, 47, 2580–2582.

- 229 M. R. Hamblin and T. Hasan, *Photochem. Photobiol. Sci.*, 2004, 3, 436–450.
- 230 H. Wu, C. Moser, H.-Z. Wang, N. Høiby and Z.-J. Song, *Int. J. Oral Sci.*, 2015, 7, 1–7.
- 231 L. Tan, J. Li, X. Liu, Z. Cui, X. Yang, S. Zhu, Z. Li, X. Yuan, Y. Zheng, K. W. K. Yeung, H. Pan, X. Wang and S. Wu, Adv. Mater., 2018, 30, 1801808.
- 232 J. Wu, C. Zhang, S. Xu, X. Pang, G. Cai and J. Wang, Colloid Interface Sci. Commun., 2018, 24, 98–104.
- 233 B. Le Ouay and F. Stellacci, Nano Today, 2015, 10, 339-354.
- 234 E.-L. Zhang, S. Fu, R.-X. Wang, H.-X. Li, Y. Liu, Z.-Q. Ma, G.-K. Liu, C.-S. Zhu, G.-W. Qin and D.-F. Chen, *Rare Met.*, 2019, 38, 476–494.
- 235 J.-M. Zhang, Y.-H. Sun, Y. Zhao, Y.-L. Liu, X.-H. Yao, B. Tang and R.-Q. Hang, *Rare Met.*, 2019, **38**, 552–560.
- 236 T. Yang, D. Wang and X. Liu, *J. Mater. Chem. B*, 2020, 8, 406–415.
- 237 N. Khan, D. Kumar and P. Kumar, *Colloid Interface Sci. Commun.*, 2020, 35, 100242.
- 238 Y.-S. Huang and H.-H. Huang, *Rare Met.*, 2019, **38**, 512–519.
- 239 B. Kong, C. Selomulya, G. Zheng and D. Zhao, *Chem. Soc. Rev.*, 2015, 44, 7997–8018.
- 240 Z. Qin, Y. Li and N. Gu, Adv. Healthcare Mater., 2018, 7, 1800347.
- 241 X. Cai, W. Gao, M. Ma, M. Wu, L. Zhang, Y. Zheng, H. Chen and J. Shi, *Adv. Mater.*, 2015, 27, 6382–6389.
- 242 L. Hang, H. Li, T. Zhang, D. Men, C. Zhang, P. Gao and Q. Zhang, ACS Appl. Mater. Interfaces, 2019, 11, 39493–39502.
- 243 M. Shokouhimehr, E. S. Soehnlen, A. Khitrin, S. Basu and S. D. Huang, *Inorg. Chem. Commun.*, 2010, 13, 58–61.
- 244 W. Zhu, K. Liu, X. Sun, X. Wang, Y. Li, L. Cheng and Z. Liu, *ACS Appl. Mater. Interfaces*, 2015, 7, 11575–11582.
- 245 P. Shou, Z. Yu, Y. Wu, Q. Feng, B. Zhou, J. Xing, C. Liu, J. Tu, O. U. Akakuru, Z. Ye, X. Zhang, Z. Lu, L. Zhang and A. Wu, *Adv. Healthcare Mater.*, 2020, **9**, 1900948.
- 246 W. Wu, L. Yu, Y. Pu, H. Yao, Y. Chen and J. Shi, *Adv. Mater.*, 2020, 32, 2000542.
- 247 L. Fétiveau, G. Paul, A. Nicolas-Boluda, J. Volatron, R. George, S. Laurent, R. Muller, L. Sancey, P. Mejanelle, A. Gloter, F. Gazeau and L. Catala, *Chem. Commun.*, 2019, 55, 14844–14847.
- 248 Y. Li, C. H. Li and D. R. Talham, *Nanoscale*, 2015, 7, 5209–5216.
- 249 X. Cai, W. Gao, L. Zhang, M. Ma, T. Liu, W. Du, Y. Zheng, H. Chen and J. Shi, ACS Nano, 2016, 10, 11115–11126.
- 250 M. Ishizaki, H. Ando, N. Yamada, K. Tsumoto, K. Ono, H. Sutoh, T. Nakamura, Y. Nakao and M. Kurihara, *J. Mater. Chem. A*, 2019, 7, 4777–4787.
- 251 W. Tian, Y. Su, Y. Tian, S. Wang, X. Su, Y. Liu, Y. Zhang, Y. Tang, Q. Ni, W. Liu, M. Dang, C. Wang, J. Zhang, Z. Teng and G. Lu, *Adv. Sci.*, 2017, 4, 1600356.
- 252 X. Cai, X. Jia, W. Gao, K. Zhang, M. Ma, S. Wang, Y. Zheng, J. Shi and H. Chen, Adv. Funct. Mater., 2015, 25, 2520–2529.

253 X. Yao, P. Yang, Z. Jin, Q. Jiang, R. Guo, R. Xie, Q. He and W. Yang, *Biomaterials*, 2019, **197**, 268–283.

Chem Soc Rev

- 254 J. An, Y.-G. Hu, C. Li, X.-L. Hou, K. Cheng, B. Zhang, R.-Y. Zhang, D.-Y. Li, S.-J. Liu, B. Liu, D. Zhu and Y.-D. Zhao, *Biomaterials*, 2020, 230, 119636.
- 255 Y. Li, J. Dang, Q. Liang and L. Yin, *Biomaterials*, 2019, 209, 138–151.
- 256 T. Feng, J. Wan, P. Li, H. Ran, H. Chen, Z. Wang and L. Zhang, *Biomaterials*, 2019, 214, 119213.
- 257 Y. Liu, G. Shu, X. Li, H. Chen, B. Zhang, H. Pan, T. Li, X. Gong, H. Wang, X. Wu, Y. Dou and J. Chang, *Adv. Funct. Mater.*, 2018, 28, 1802026.
- 258 L. Cheng, H. Gong, W. Zhu, J. Liu, X. Wang, G. Liu and Z. Liu, *Biomaterials*, 2014, 35, 9844–9852.
- 259 M. Gautam, B. Kumar Poudel, Z. Chi Soe, K. Poudel, S. Maharjan, S. Kwang Ku, C. Soon Yong, S. Woo Joo, J. Oh Kim and J. Hoon Byeon, *Chem. Eng. J.*, 2020, **383**, 123177.
- 260 X.-D. Li, X.-L. Liang, F. Ma, L.-J. Jing, L. Lin, Y.-B. Yang, S.-S. Feng, G.-L. Fu, X.-L. Yue and Z.-F. Dai, *Colloids Surf.*, B, 2014, 123, 629–638.
- 261 P. Xue, K. K. Y. Cheong, Y. Wu and Y. Kang, *Colloids Surf.*, *B*, 2015, **125**, 277–283.
- 262 C. Tong, X. Zhong, Y. Yang, X. Liu, G. Zhong, C. Xiao, B. Liu, W. Wang and X. Yang, *Biomaterials*, 2020, 243, 119936.
- 263 Y. Y. Su, Z. Teng, H. Yao, S. J. Wang, Y. Tian, Y. L. Zhang, W. F. Liu, W. Tian, L. J. Zheng, N. Lu, Q. Q. Ni, X. D. Su, Y. X. Tang, J. Sun, Y. Liu, J. Wu, G. F. Yang, G. M. Lu and L. J. Zhang, ACS Appl. Mater. Interfaces, 2016, 8, 17038–17046.
- 264 J.-J. Hu, Y. Chen, Z.-H. Li, S.-Y. Peng, Y. Sun and X.-Z. Zhang, *Nano Lett.*, 2019, **19**, 5568–5576.
- 265 D. Wang, J. Zhou, R. Shi, H. Wu, R. Chen, B. Duan, G. Xia, P. Xu, H. Wang and S. Zhou, *Theranostics*, 2017, 7, 4605.
- 266 D. Wang, J. Zhou, R. Chen, R. Shi, G. Zhao, G. Xia, R. Li, Z. Liu, J. Tian, H. Wang, Z. Guo, H. Wang and Q. Chen, *Biomaterials*, 2016, **100**, 27–40.
- 267 Y. Luo, J. Li, X. Liu, L. Tan, Z. Cui, X. Feng, X. Yang, Y. Liang, Z. Li, S. Zhu, Y. Zheng, K. W. K. Yeung, C. Yang, X. Wang and S. Wu, ACS Cent. Sci., 2019, 5, 1591–1601.
- 268 L. Jing, X. Liang, Z. Deng, S. Feng, X. Li, M. Huang, C. Li and Z. Dai, *Biomaterials*, 2014, 35, 5814–5821.
- 269 W. Zhu, M.-Y. Gao, Q. Zhu, B. Chi, L.-W. Zeng, J.-M. Hu and A.-G. Shen, *Nanoscale*, 2020, **12**, 3292–3301.
- 270 G. Fu, W. Liu, Y. Li, Y. Jin, L. Jiang, X. Liang, S. Feng and Z. Dai, *Bioconjugate Chem.*, 2014, 25, 1655–1663.
- 271 J. Peng, M. Dong, B. Ran, W. Li, Y. Hao, Q. Yang, L. Tan, K. Shi and Z. Qian, ACS Appl. Mater. Interfaces, 2017, 9, 13875–13886.
- 272 J. Peng, Q. Yang, W. Li, L. Tan, Y. Xiao, L. Chen, Y. Hao and Z. Qian, *ACS Appl. Mater. Interfaces*, 2017, **9**, 44410–44422.
- 273 X. Zheng, L. Wang, M. Liu, P. Lei, F. Liu and Z. Xie, *Chem. Mater.*, 2018, **30**, 6867–6876.
- 274 Y. Wu, M. Yuan, J. Song, X. Chen and H. Yang, *ACS Nano*, 2019, **13**, 8505–8511.
- 275 F. Liu, X. He, H. Chen, J. Zhang, H. Zhang and Z. Wang, Nat. Commun., 2015, 6, 8003.

- 276 J. Li, C. Zhang, S. Gong, X. Li, M. Yu, C. Qian, H. Qiao and M. Sun, *Acta Biomater.*, 2019, 94, 435–446.
- 277 G. Zhao, H. Wu, R. Feng, D. Wang, P. Xu, P. Jiang, K. Yang, H. Wang, Z. Guo and Q. Chen, ACS Appl. Mater. Interfaces, 2018, 10, 3295–3304.
- 278 W. Cai, H. Gao, C. Chu, X. Wang, J. Wang, P. Zhang, G. Lin, W. Li, G. Liu and X. Chen, *ACS Appl. Mater. Interfaces*, 2017, 9, 2040–2051.
- 279 W. Zhu, M. Chen, Y. Liu, Y. Tian, Z. Song, G. Song and X. Zhang, *Nanoscale*, 2019, 11, 20630–20637.
- 280 S. Dang, Q.-L. Zhu and Q. Xu, Nat. Rev. Mater., 2017, 3, 17075.
- 281 S.-N. Zhao, X.-Z. Song, S.-Y. Song and H.-j. Zhang, Coord. Chem. Rev., 2017, 337, 80–96.
- 282 K. Xiong, J. Li, L. Tan, Z. Cui, Z. Li, S. Wu, Y. Liang, S. Zhu and X. Liu, *Colloid Interface Sci. Commun.*, 2019, 33, 100201.
- 283 H. Xiang, W. Feng and Y. Chen, *Adv. Mater.*, 2020, 32, 1905994.
- 284 Y. Weng, S. Guan, L. Wang, H. Lu, X. Meng, G. I. N. Waterhouse and S. Zhou, *Small*, 2020, **16**, 1905184.
- 285 A. Han, B. Wang, A. Kumar, Y. Qin, J. Jin, X. Wang, C. Yang,
   B. Dong, Y. Jia, J. Liu and X. Sun, *Small Methods*, 2019,
   3, 1800471.
- 286 L. Jiao and H.-L. Jiang, Chem, 2019, 5, 786-804.
- 287 B. Xu, H. Wang, W. Wang, L. Gao, S. Li, X. Pan, H. Wang, H. Yang, X. Meng, Q. Wu, L. Zheng, S. Chen, X. Shi, K. Fan, X. Yan and H. Liu, *Angew. Chem., Int. Ed.*, 2019, 58, 4911–4916.
- 288 P. Yin, T. Yao, Y. Wu, L. Zheng, Y. Lin, W. Liu, H. Ju, J. Zhu, X. Hong, Z. Deng, G. Zhou, S. Wei and Y. Li, *Angew. Chem., Int. Ed.*, 2016, 55, 10800–10805.
- 289 Q. Yang, C.-C. Yang, C.-H. Lin and H.-L. Jiang, *Angew. Chem., Int. Ed.*, 2019, **58**, 3511–3515.
- 290 M. Huo, L. Wang, Y. Wang, Y. Chen and J. Shi, *ACS Nano*, 2019, **13**, 2643–2653.
- 291 Y. Yang, Y. Deng, J. Huang, X. Fan, C. Cheng, C. Nie, L. Ma, W. Zhao and C. Zhao, *Adv. Funct. Mater.*, 2019, 29, 1900143.
- 292 X. Fan, F. Yang, J. Huang, Y. Yang, C. Nie, W. Zhao, L. Ma, C. Cheng, C. Zhao and R. Haag, *Nano Lett.*, 2019, 19, 5885–5896.
- 293 T. Kitao, Y. Zhang, S. Kitagawa, B. Wang and T. Uemura, Chem. Soc. Rev., 2017, 46, 3108–3133.
- 294 Y.-D. Zhu, S.-P. Chen, H. Zhao, Y. Yang, X.-Q. Chen, J. Sun, H.-S. Fan and X.-D. Zhang, ACS Appl. Mater. Interfaces, 2016, 8, 34209–34217.
- 295 Q. Wu, M. Niu, X. Chen, L. Tan, C. Fu, X. Ren, J. Ren, L. Li, K. Xu, H. Zhong and X. Meng, *Biomaterials*, 2018, 162, 132-143.
- 296 W. Wang, L. Wang, Y. Li, S. Liu, Z. Xie and X. Jing, Adv. Mater., 2016, 28, 9320–9325.
- 297 J. Huang, N. Li, C. Zhang and Z. Meng, ACS Appl. Mater. Interfaces, 2018, 10, 38729–38738.
- 298 Y. Li, J. Jin, D. Wang, J. Lv, K. Hou, Y. Liu, C. Chen and Z. Tang, *Nano Res.*, 2018, 11, 3294–3305.
- 299 L. Zhang, C. Liu, Y. Gao, Z. Li, J. Xing, W. Ren, L. Zhang, A. Li, G. Lu, A. Wu and L. Zeng, *Adv. Healthcare Mater.*, 2018, 7, 1801144.

300 X. Yang, L. Li, D. He, L. Hai, J. Tang, H. Li, X. He and K. Wang, J. Mater. Chem. B, 2017, 5, 4648-4659.

**Review Article** 

- 301 L. An, M. Cao, X. Zhang, J. Lin, Q. Tian and S. Yang, ACS Appl. Mater. Interfaces, 2020, 12, 8050-8061.
- 302 X. Liu, Y. Pan, J. Yang, Y. Gao, T. Huang, X. Luan, Y. Wang and Y. Song, Nano Res., 2020, 13, 653-660.
- 303 J. Yao, Y. Liu, J. Wang, Q. Jiang, D. She, H. Guo, N. Sun, Z. Pang, C. Deng, W. Yang and S. Shen, Biomaterials, 2019, **195**, 51-62.
- 304 W. Shang, C. Zeng, Y. Du, H. Hui, X. Liang, C. Chi, K. Wang, Z. Wang and J. Tian, Adv. Mater., 2017, 29, 1604381.
- 305 B. Li, Q. Wang, R. Zou, X. Liu, K. Xu, W. Li and J. Hu, Nanoscale, 2014, 6, 3274-3282.
- 306 M. Wang, K. Deng, W. Lü, X. Deng, K. Li, Y. Shi, B. Ding, Z. Cheng, B. Xing, G. Han, Z. Hou and J. Lin, Adv. Mater., 2018, 30, 1706747.
- 307 X. Deng, K. Li, X. Cai, B. Liu, Y. Wei, K. Deng, Z. Xie, Z. Wu, P. a. Ma, Z. Hou, Z. Cheng and J. Lin, Adv. Mater., 2017, 29, 1701266.
- 308 H. Chen, Y. Ma, X. Wang and Z. Zha, J. Mater. Chem. B, 2017, 5, 7051-7058.
- 309 J. Li, F. Zhang, Z. Hu, W. Song, G. Li, G. Liang, J. Zhou, K. Li, Y. Cao, Z. Luo and K. Cai, Adv. Healthcare Mater., 2017, 6, 1700005.
- 310 Y. Zhang, Y. Liu, X. Gao, X. Li, X. Niu, Z. Yuan and W. Wang, Acta Biomater., 2019, 90, 314-323.
- 311 Y. Zhang, L. Wang, L. Liu, L. Lin, F. Liu, Z. Xie, H. Tian and X. Chen, ACS Appl. Mater. Interfaces, 2018, 10, 41035-41045.
- 312 Z. Luo, L. Jiang, S. Yang, Z. Li, W. M. W. Soh, L. Zheng, X. J. Loh and Y.-L. Wu, Adv. Healthcare Mater., 2019, 8, 1900406.
- 313 S. Wang, L. Shang, L. Li, Y. Yu, C. Chi, K. Wang, J. Zhang, R. Shi, H. Shen, G. I. N. Waterhouse, S. Liu, J. Tian, T. Zhang and H. Liu, Adv. Mater., 2016, 28, 8379-8387.
- 314 F. Zhang, Y. Liu, J. Lei, S. Wang, X. Ji, H. Liu and Q. Yang, Adv. Sci., 2019, 6, 1901378.
- 315 P. Yang, Y. Tian, Y. Men, R. Guo, H. Peng, Q. Jiang and W. Yang, ACS Appl. Mater. Interfaces, 2018, 10, 42039-42049.

- 316 C. Liu, D. Kong, P.-C. Hsu, H. Yuan, H.-W. Lee, Y. Liu, H. Wang, S. Wang, K. Yan, D. Lin, P. A. Maraccini, K. M. Parker, A. B. Boehm and Y. Cui, Nat. Nanotechnol., 2016, 11, 1098-1104.
- 317 Y. Ren, Y. Han, Z. Li, X. Liu, S. Zhu, Y. Liang, K. W. K. Yeung and S. Wu, Bioact. Mater., 2020, 5, 201-209.
- 318 B. Wu, Y. Li, K. Su, L. Tan, X. Liu, Z. Cui, X. Yang, Y. Liang, Z. Li, S. Zhu, K. W. K. Yeung and S. Wu, J. Hazard. Mater., 2019, 377, 227-236.
- 319 Y. Li, X. Liu, L. Tan, Z. Cui, X. Yang, Y. Zheng, K. W. K. Yeung, P. K. Chu and S. Wu, Adv. Funct. Mater., 2018, 28, 1800299.
- 320 M. Chen, Z. Long, R. Dong, L. Wang, J. Zhang, S. Li, X. Zhao, X. Hou, H. Shao and X. Jiang, Small, 2020, 16, 1906240.
- 321 J. Li, L. Tan, X. Liu, Z. Cui, X. Yang, K. W. K. Yeung, P. K. Chu and S. Wu, ACS Nano, 2017, 11, 11250-11263.
- 322 B. Huang, L. Tan, X. Liu, J. Li and S. Wu, Bioact. Mater., 2019, 4, 17-21.
- 323 S. Tavakoli, S. Nemati, M. Kharaziha and S. Akbari-Alavijeh, Colloid Interface Sci. Commun., 2019, 28, 20-28.
- 324 L. Huang, J. Li, W. Yuan, X. Liu, Z. Li, Y. Zheng, Y. Liang, S. Zhu, Z. Cui, X. Yang, K. W. K. Yeung and S. Wu, Corros. Sci., 2020, 163, 108257.
- 325 Q.-W. Chen, X.-H. Liu, J.-X. Fan, S.-Y. Peng, J.-W. Wang, X.-N. Wang, C. Zhang, C.-J. Liu and X.-Z. Zhang, Adv. Funct. Mater., 2020, 30, 1909806.
- 326 R. Riccò, W. Liang, S. Li, J. J. Gassensmith, F. Caruso, C. Doonan and P. Falcaro, ACS Nano, 2018, 12, 13-23.
- 327 S. Yan, X. Zeng, Y. Wang and B.-F. Liu, Adv. Healthcare Mater., 2020, 9, 2000046.
- 328 S. Qiu, M. Xue and G. Zhu, Chem. Soc. Rev., 2014, 43, 6116-6140.
- 329 J. Zhao, W. T. Nunn, P. C. Lemaire, Y. Lin, M. D. Dickey, C. J. Oldham, H. J. Walls, G. W. Peterson, M. D. Losego and G. N. Parsons, J. Am. Chem. Soc., 2015, 137, 13756-13759.
- 330 J. Zhao, B. Kalanyan, H. F. Barton, B. A. Sperling and G. N. Parsons, Chem. Mater., 2017, 29, 8804-8810.